Governing the Biological Interactions of Monolayer Protected Gold Nanoparticles by Controlling the Composition and Spatial Structure of the Thiolate Shell

By

Adam Ryan Travis

Dissertation

Submitted to the Faculty of the

Graduate School of Vanderbilt University

in partial fulfillment of the requirements

for the degree of

DOCTOR OF PHILOSOPHY

in

Chemistry

August 11, 2017

Nashville, Tennessee

Approved:

David E. Cliffel, Ph.D.

David W. Wright, Ph.D.

John A. McLean, Ph.D.

Craig L. Duvall, Ph.D.

For Peggy Bielefeld and Berle Travis, Sr.

ACKNOWLEDGMENTS

Without financial contributions from sources both internal and external to Vanderbilt University, this work would not have been possible. Funding was provided by the National Institutes of Health, Environmental Protection Agency, Vanderbilt Institute of Chemical Biology, and Frederic LeRoy Conover Graduate Research Fellowship. I would also like to thank the Graduate School of Vanderbilt University for awarding me a University Graduate Fellowship. This fellowship significantly enhanced my experience here in Nashville, and I will be forever grateful for it. Non-financial support from the staff here has also been invaluable. From the NMR facilities to the Storeroom, everyone has always been so helpful, and you would be hard-pressed to find friendlier faces than those of the custodial staff in Stevenson 5 and 7.

Iron sharpeneth iron; so a man sharpeneth the countenance of his friend. During my time in graduate school, I have had the privilege to work alongside some incredibly intelligent and hardworking people. To all of the members of the Cliffel and Wright research groups with whom I have labored, thank you for providing me with guidance and camaraderie. Kim Fong, from rotations to writing, you have been a true friend. If the pipettes in the cell room could talk, they would testify to just how much of a caring, diligent, and genuine person you are. You continue to be a shining example of how a person should conduct him or herself at all times. Jenny Nesbitt, my first mentor, you made teaching Capstone infinitely more tolerable, and I have an immense amount of respect for the amount of time that you dedicated to teaching. Stephen Jackson, you taught me what happens when an immovable object meets an irresistible force. Mandy Agrawal, your third year seminar was why I rotated in the Cliffel Lab. Thank you for helping me as much as you did even though our time only briefly overlapped. Danielle Kimmel, you have kept me sane in some of the more interesting moments. If I ever needed to vent and then have a good

laugh, I knew you were always there to lend an ear. Evan Gizzie, I have felt like I have been in your shadow from the day I joined the Cliffel Lab. Wherever you go next, I have no doubts that you will succeed. That finally brings me to the Nano Lab Crew. Matt Casey and David Crisostomo, you two made 5526 a blast. I also have the two of you to blame for introducing me to two of the biggest distractions in my life: Reddit and PokemonShowdown. Dave, I am going to miss having to explain some of my more bizarre Southernisms to you, but hopefully after 5+ years together you can finally understand me.

I would be remiss if I failed to mention the graduate students who are still working their way to a Ph.D. too. Alexis Wong, you and I are some of the last gold nanoparticle holdouts. From cell room struggles to feeling neglected, we somehow have both made it to the end. Westley Bauer, I am not going to miss the peptide synthesizer, and I doubt that you or Anna Bitting will either. Aaron Daniel, I am so sorry that you will be the last of the Nano Lab Crew, but maybe this will help expedite your defense date. I would say that I will call the lab phone to check in on you every now and again, but we both know that you would not answer it anyway. Ha! Ethan McClain and Sara Melow, I wish you both the best of luck. You two really helped me crank out some data here at the end. Chris, Dilek, and Margaret, hold down the fort. Jo^2, make Mr. Jordan proud.

My success in graduate school is due in no small part to the firm academic foundation built by my former teachers at Woodlawn Elementary School, New Providence Middle School, Northwest High School, and The University of Tennessee at Martin. Thank you all for dedicating your lives to education, and please know that you have left a lasting impression as I fondly look back on my pre-graduate school days. I would also like to thank my committee members and instructors here at Vanderbilt for grilling me during exams for my betterment. Dr. Polavarapu,

Group Theory was likely the most fair and difficult class that I have ever taken. I have always loved geometry, but I left each and every lecture with a new appreciation for its applications. Dr. McLean, you stopped me in the hallway a few days after my qualifying exam and gave me a word of encouragement that I really needed. You may not even recall the comment that you made, but it greatly impacted me. Thank you. Sincerely. Dr. Cliffel, I cannot imagine a more laid back and approachable professor under whom I could have completed my graduate research. I considered myself a fairly self-motivated individual before joining the lab, but I have since learned the true value of being an independent, critical thinker.

The friends that I have made in Nashville outside of the department and off campus are too numerous to mention. There are a few, however, to whom I would like to give special recognition. Jake Hall, you were an amazing roommate and an even better friend – despite the fact that you abandoned me to follow your boss to Cleveland! I only wish that your trips back home could be more frequent. To everyone at Music City Church, thank you for being so encouraging and inclusive. I always look forward to our time together in service and life groups.

The last group of people I would like to thank is my family, both immediate and extended. The unrelenting spirit of determination that you instilled in me helped me make it through the more tedious moments here. You have also provided me with many a mental reprieve from the hustle and bustle of life here in "the big city" of Nashville. The tales that I have brought back from my weekend trips home to Woodlawn, Indian Mound, and Cumberland City have undoubtedly contributed to the honing of my storytelling skills. Just ask any of my labmates. I have known from the very beginning just how proud of me that you all are, and for those of you who jokingly questioned if I would be in school for my entire life, I can finally say, "No, I'm finished!"

TABLE OF CONTENTS

Page

DEDICATION ii

ACKNOWLEDGMENTS iii

LIST OF TABLES viii

LIST OF FIGURES ix

Chapter

I. AN INTRODUCTION TO NANOMATERIALS 1
- Nanomedicine 2
- Biomimetics 6
- Controlling Function through Structure 7

II. DESIGNING THE SURFACE OF GOLD NANOPARTICLES TO ENHANCE TARGETED RADIOSENSITIZATION 9
- Introduction 9
  - Lung Cancer, Angiogenesis, and the Role of Integrins 9
  - Cilengitide 11
  - Radiosensitizers and Gold Nanoparticles 12
- Experimental Methods 15
  - Materials 15
  - Nanoparticle Synthesis 16
  - ^{137}Cs Clonogenic Assays 18
- Results & Discussion 19
  - Nanoparticle Characterization 19
  - *In Vitro* Activity 22

III. ENHANCING THE IMMUNOGENICTY OF GOLD NANOPARTICLES BY SPATIALLY CONSTRAINING BIOMIMETIC LIGANDS 28
- Introduction 29
  - Anthrax and BioThrax 29
  - Biomimetic Vaccines 30
- Experimental Methods 32
  - Materials 32
  - Nanoparticle Synthesis 32
  - Animal Studies 34
- Results & Discussion 36

IV. TUNING THE PATTERNING OF LIGANDS ON THE SURFACE OF GOLD NANOPARTICLES 43
- Introduction 4

Nanoscale Patterning 43
Characterization Methods for Nanoscale Patterning 45
Applications of Anisotropy 49
Synthetic Routes to Janus Particles 50
Experimental Methods 52
Materials 52
Ligand Syntheses 52
Nanoparticle Syntheses 56
Place Exchanges 58
Nanoparticle Characterization 58
Results & Discussion 59

V. CONCLUSIONS AND FUTURE DIRECTIONS 66
Preventive Nanoparticles 66
Diagnostic Nanoparticles 71
Therapeutic Nanoparticles 72

Appendix

A. VALIDATION OF A ROTARY PLANAR VALVE AND ROTARY PLANAR PERISTALTIC MICROPUMP AS A MICROFORMULATOR 75
Introduction 75
Experimental Methods 76
Results & Discussion 79

B. APPLICATIONS OF MULTIANALYTE MICROPHYSIOLOGICAL DEVICES 85
Strategies for Avoiding Electrochemical Interference 85
In Vitro Multianalyte Microphysiometry 87
Multianalyte Microphysiometer 87
Microclinical Analyzer 88
Experimental Methods 89
Results & Discussion 92
In Vivo Multianalyte Microphysiometry 96
Microdialysis Probes 97
Implantable Electrodes 99
Wearable Devices 102
Conclusions 104

REFERENCES 106

CURRICULUM VITAE 119

LIST OF TABLES

Table Page

2.1 Dose enhancement factors in HUVECs, H460s, and MCF-7s treated with Cilengitide mimics on AuNPs....26

B.1 Summary of off-line electrochemical measurements of glucose, lactate, and glutamate in the effluent from NVUs....96

LIST OF FIGURES

Figure Page

1.1 Diagram of hAuNPs 3

2.1 Structure of Cilengitide and the binding pocket of $\alpha_v\beta_3$ integrin 12

2.2 Transmission electron micrographs of Tio and GS AuNPs 21

2.3 Thermogravimetric analysis plot of Tio AuNPs 21

2.4 ^{1}H NMR spectra of RGD peptides, Tio AuNPs, and RGD peptides on Tio AuNPs 22

2.5 Results of clonogenic assays evaluating the density of peptides on AuNPs 23

2.6 Results of clonogenic assays evaluating the spatial constraint of peptides on AuNPs 24

2.7 Results of clonogenic assays evaluating the passivating backfill ligand on AuNPs 25

3.1 Time-dependent gold concentrations in murine blood samples 37

3.2 Time-dependent gold concentrations in murine urine samples 38

3.3 Gold content in the organs of euthanized mice 39

3.4 Results of competitive sandwich ELISAs 40

4.1 STM images of Janus and striped nanoparticles 46

4.2 Diagrams of staple structures known to passivate gold cores 47

4.3 MALDI-IM-MS spectrum of Tio/MUTEG AuNPs 48

4.4 Azide-terminated PEGs and their synthetic intermediates 51

4.5 NOESY spectrum of C6/PEPEPSH AuNPs 60

4.6 NOESY spectrum of Tio/MUTEG AuNPs 61

4.7 MALDI-IM-MS spectra of various place exchanged AuNPs 62

4.8 Deviation from a binomial distribution model using MALDI-IM-MS data 63

5.1 Proposed peptides sequences for anti-gp120 AuNPs 69

5.2 Proposed BLI/QCM experiments using anti-gp120 AuNPs 70

5.3 Fluorescence of etched vs unetched Tio AuNPs 72

5.4 Tumor volume and survival curves of mice treated with AuNPs and radiotherapy 73

5.5 Electronic coupling of AuNPs to behave as AuNRs 74

A.1 Image of a microformulator 77

A.2 ICP-OES results of a valve leakage test 79

A.3 ICP-OES results of equal-time formulations 80

A.4 Flow rate calibrations of a five port rotary planar valve 81

A.5 Stroke volumes of a rotary planar peristaltic micropump operating at varying speeds ... 82

A.6 ICP-OES results of formulations created by time-division multiplexing 83

B.1 SPEA diagram and glucose, lactate, and glutamate calibration curves 92

B.2 Acetylcholine detection strategy and calibration curve 93

B.3 Stability measurements of glucose, lactate, and glutamate oxidase electrodes with and without the addition of a bubble trap 95

Chapter I

AN INTRODUCTION TO NANOMATERIALS

Nanotechnology can be broadly defined as the science behind and resulting from the manipulation of pieces of matter with at least one dimension between 1 and 100 nm. One of the earliest known usages of nanoscale materials was to improve the aesthetics of bulk materials.[1,2] Likely the most well-known example of such artisan work, the Roman-era Lycurgus cup owes its unique optical properties to the incorporation of nanoparticulate gold and silver into glass.[1] Craftsmen in other fields also developed techniques that employed nanomaterials but for more utilitarian purposes.[2,3] Transmission electron micrographs of residue from a seventeenth century sword forged from wootz ingots revealed carbon nanotubes.[3] Such evidence offers an explanation for the renowned flexibility and strength of Damascus blades whose exact fabrication methods have been lost to time.

The origin of the modern concept of nanotechnology is commonly traced back to 1959 when Richard Feynman gave a lecture entitled "There's Plenty of Room at the Bottom" to a meeting of the American Physical Society.[4] Approximately two decades later, observations of individual atoms were made possible by the development of scanning tunneling microscopy (STM).[5] Other nanoscale capabilities, including the physical manipulation of atoms and molecules, were realized soon after by the advent of atomic force microscopy (AFM).[6] Both techniques have had powerful impacts in the field of surface chemistry, and the work presented in this dissertation focuses on potential biological applications of nanomaterials with carefully tuned surface properties.

Nanomedicine

In the past thirty years, nanotechnology has advanced from being a novelty of science to being incorporated in over one thousand commercial products.[7] With the currently observed upward trajectory of life expectancy,[8] the application of nanotechnology to solve problems relating to the quality and length of life comes as no surprise. Goods featuring elements of nanotechnology in human health can be broadly classified into four categories: preventives, diagnostics, therapeutics, and toxicants. Investigations into and applications of these four subsets form the basis of nanomedicine.

Diarrheal diseases are the leading cause of childhood malnutrition and the second leading cause of death in children under five years of age.[9] Largely a result of contaminated water supplies, these deaths are counted as preventable and are concentrated in developing nations where water-treatment infrastructure is poor or lacking altogether. Thus, there is a significant need for scalable, low-cost solutions. Purification devices utilizing adsorbents, photocatalytic nano-metals/metal oxides, and membrane processes are gaining traction and represent a significant step in improving the global water supply and thus global health.[10]

Preventive nanomedicine also has applications in the developed world. In times of severe drought or water service disruption following a natural disaster, atypical water sources could prove valuable if the appropriate purification devices are available. Other preventive nanomedicine applications can be found in the size-dependent interaction of nanomaterials with light. Newer formulations of sunscreens commonly contain titanium dioxide and zinc oxide nanoparticles to expand the spectrum of afforded photoprotection, and these nanoparticles have the additional benefit of being more optically transparent.[11] Improving the perception of such preventive measures by the public has the potential to increase adherence to preventive

protocols. For melanoma, this is of particular concern as rates have continued to rise for the past thirty years.[12]

When preventive measures fail, the accurate and early diagnosis of many cancers has been shown to dramatically improve survival rates. For melanoma patients, those diagnosed at Stage IA have a 97% 10 year survival rate whereas that for Stage IIIC patients is 24%. For breast cancer patients, the difference is equally stark. 5 year survival rates for Stage 0 and I patients are nearly 100%, but this drops to 72% for Stage III and to 22% for Stage IV.[13] To facilitate early and accurate diagnosis, gold nanoparticles (AuNPs) have been developed to quantify intracellular mRNA that codes for biomarkers linked to these cancers (Figure 1).[14,15] These

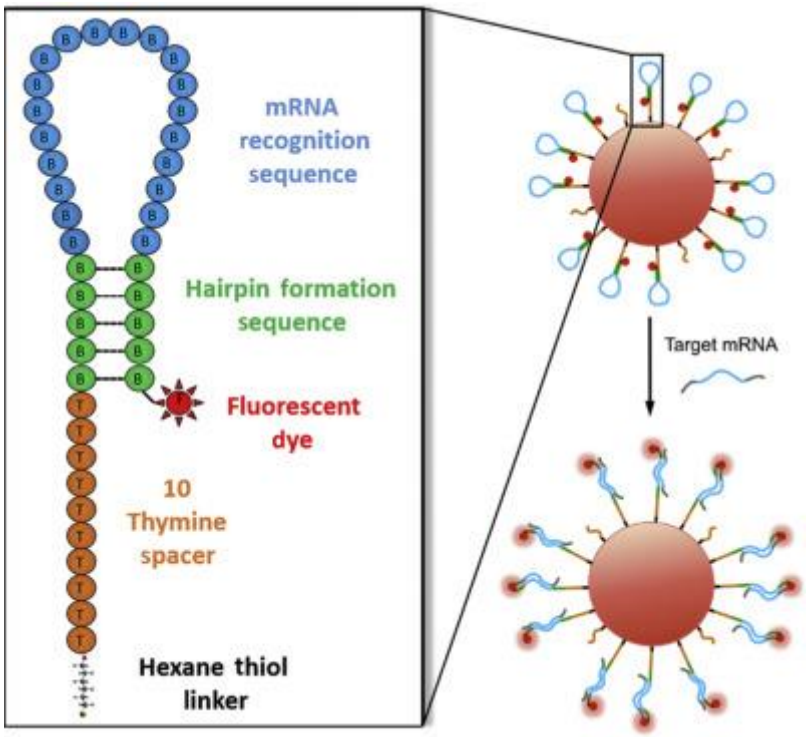

Figure 1.1: Diagram of gold nanoparticles functionalized with hairpin DNA. Upon binding to mRNA that is complementary to the loop region, the hairpin opens. This results in the dye on the 3' end of the DNA extending away from the gold core, allowing it to fluoresce.[15]

AuNPs are functionalized with oligonucleotides capped with hexanethiol on the 5' end and a fluorophore on the 3' end. A polythymine spacer allows the hairpin sequence to extend away from the gold core, and two self-complementary regions terminate the loop of the hairpin. The loop region is complementary to mRNA of interest, and upon hybridization with its target sequence, the hairpin overcomes the energy barrier needed to break the hydrogen bonds of the self-complementary sequence. This straightening of the hairpin loop increases the distance between the fluorophore and the gold core which previously quenched the fluorescence of the dye. The increase in fluorescence can be quantified using methods such as confocal microscopy or flow cytometry. The use of these hairpin-DNA functionalized AuNPs (hAuNPs) offers some unique advantages over other techniques such as RT-PCR and using molecular beacons due to the ability to investigate expression profiles of individual cells and increased resistance to degradation by cytoplasmic nucleases.[14] Additionally, hAuNPs are compatible with live cell imaging, require no transfection reagents, have not been observed to exhibit cytotoxic effects *in vitro*, and can be multiplexed to quantify several transcripts simultaneously.[14,15] This last property is limited only by the user's ability to deconvolute multiple fluorescence signals.

Other interactions of nanostructures with electromagnetic radiation provide the anti-cancer effects seen in photodynamic and photothermal therapies.[16,17] In the case of AuNPs, these mechanisms often rely on the surface plasmon resonance band. This property arises from the collective oscillation of electrons in the conduction band and is dependent on both the shape and size of the nanostructure.[17] At this frequency, absorption of incident light is at a local maximum. Relaxation of the electrons can then occur thermally,[17] or resonance energy transfer can occur to nearby photosensitizers resulting in the production of reactive oxygen species.[16] In both cases, the therapeutic effects are localized to the desired areas by specifically targeting tumors with

lower energy radiation sources which keeps the collateral damage often seen in chemo- and radiotherapeutics to a minimum.

Both organic and inorganic nanostructures can also serve as therapeutic scaffolds for drugs whose solubility is poor. Many molecules that serve as photosensitizers in photodynamic therapy are limited by their hydrophobicity. By encapsulating these drugs in lipids or polymers or by loading them onto the surface of inorganic cores, the ability to deliver them to sites of interest can be significantly enhanced.[16] Conjugating targeting moieties such as peptides or other small molecules allows active targeting of overexpressed surface bound receptors on cancer cells.[16] Chemo- or photoactivation of these scaffolds can then result in the release of the drug intracellularly or into the tumor microenvironment, again mitigating collateral damage.[16]

The benefits and applications of nanomaterials have historically received more attention than potential adverse health effects.[18] With the ever-growing presence of nanomaterials, however, identifying any long-term drawbacks has begun gaining more attention.[4] Studies have shown unexpected acute renal toxicity for some monolayer protected AuNPs which can be avoided by simple surface modifications to the particles.[19] Additionally, long-term changes to human cells after single dose exposures to AuNPs have been found,[20] and the repeated application of nanomaterials to human skin has been called into question.[11] A few studies have examined the fate of nanomaterials in the environment,[21] and as the understanding of the interactions between living tissue and engineered nanomaterials grows, this too will likely become an area of further interest.

Each chapter in this dissertation deals with at least one aspect of nanomedicine. Chapter II examines the use of biomimetic AuNPs as therapeutics, specifically as targeted radiosensitizing agents. Chapter III investigates the possibility of using AuNPs in a preventive

capacity and describes efforts to identify potential toxicological properties. The ability to stimulate a humoral immune response with peptides on AuNPs is explored in a murine model, and post-mortem histological examinations were performed to identify any adverse renal effects. Chapter IV details the synthesis and characterization of multifunctional AuNPs with potential uses in both diagnostic and therapeutic applications. Conclusions and an outlook on the future of nanomedicine are presented in Chapter V with following appendices describing microfluidic devices that are being developed to monitor metabolic responses to a variety of chemical challenges, including those posed by nanomaterials.

Biomimetics

The growing field of biomimetics capitalizes on the exquisite molecular architecture that already exists in nature. The microscopic ordering of biological materials often gives rise to macroscopic observations such as the ability of geckos to crawl along almost any surface, mussels to withstand the forces in the tidal zone, and burs to cling to the fur of passing animals.[22] Biomimetics does not simply seek to replicate the structural elements responsible for these phenomena, but it seeks to understand the driving forces that cause the emergence of such properties and apply this understanding to create new materials.

In the context of nanomedicine, the guiding principles of biomimetics can be used to synthesize novel materials that interface with biological systems. This may involve starting with previously solved crystal structures of a protein with or without co-crystalized species of interest. When targeting overexpressed receptor proteins, this knowledge can be used to design artificial ligands with affinities even greater than those of the naturally occurring agonists.[23] Such synthetic peptides may incorporate unnatural amino acids or other residues to impart functions

not possible through biological means. Conjugating these biomimetic structures to AuNPs allows preventive, diagnostic, and therapeutic benefits to be realized and is the basis for the studies undertaken in Chapters II and III.

Controlling Function through Structure

Compounds with component atoms joined through identical connectivity but with different three-dimensional structures are known as stereoisomers. The biological effects of such isomers can vary dramatically. For example, conversion of a single chiral center in thalidomide from R to S results in teratogenic birth defects.[24] Other drugs, such as omeprazole, exist as racemic mixtures. Only the S enantiomer of omeprazole provides a therapeutic benefit, making it the eutomer, but no adverse effects of the R enantiomer, the distomer, have been noted.[24] Additionally, R is readily converted to S *in vivo* by most populations, making the separation of the two unnecessary.[24]

Spatial rearrangements that do not require the breakage of chemical bonds result in conformational isomers, also known as rotamers or conformers. For proteins, structural changes can have severe deleterious effects on biological activity, and Anfinsen's dogma, also known as the thermodynamic hypothesis of protein folding, says that the three-dimensional structure of a protein is dictated only by the primary sequence of amino acids.[25] However, this structure is highly dependent on conditions such as temperature and solvent effects, and the denaturation of proteins can be accomplished through chemical and thermal means with varying degrees of intramolecular rearrangement and therefore changes in activity.[26,27] By removing the denaturing conditions, refolding into an active, native state is often possible to some extent.[28] Perturbations to the native structure of proteins *in vivo* are removed through biological mechanisms; misfolded

proteins are either refolded into a native state by chaperones or are degraded by proteases.[29] When these mechanisms fail to eliminate the misfolds, intermolecular interactions between proteins can result in the formation of aggregates which have been linked to a variety of disease states including Alzheimer's, Huntington's, and Parkinson's.[30]

Due to this reliance of biological activity on the spatial arrangement of individual amino acids, synthetic peptides meant to interface with biology should be designed with conformational requirements in mind. The excision of short peptide sequences may fail to fold into the same conformation seen in the native protein, seemingly violating Anfinsen's dogma due to the lack of distant intramolecular forces helping to shape the three-dimensional structure of the excised region. The attachment of these short peptides to the surface of AuNPs can reduce the number of available conformations. By providing anchoring sites, AuNPs may allow peptides to adopt conformations more similar to those found in the native proteins in addition to providing benefits such as increased resistance to proteases and improved delivery to sites of interest. The following two chapters investigate the ability of these bio-nanoconjugates to exhibit biological activity as a function of the conformations of the surface peptides.

Chapter II

DESIGNING THE SURFACE OF GOLD NANOPARTICLES TO ENHANCE TARGETED RADIOSENSITIZATION

This chapter explores the use of linear and looped RGDfV sequences attached to the surface of small (<5 nm) gold nanoparticles (AuNPs) to enhance the radiosensitizing effects of Cilengitide, a cyclic RGDf(*N*Me)V pentapeptide that targets $\alpha_v\beta_3$ integrin which is overexpressed in certain cancers. The synthesis of the AuNPs is detailed, followed by their performance in clonogenic assays against HUVECs, H460s, and MCF7s using a ^{137}Cs irradiator. Untargeted AuNPs induced no significant dose enhancement factors (DEFs) in any of the cell types when compared to radiation treatment alone, whereas all evaluated AuNPs functionalized with targeting peptides performed at least as well as controls (irradiation after Cilengitide treatment). The observed DEFs also suggest that spatially constraining the linear peptides into looped structures may facilitate target binding. These greater dose enhancements merit future *in vivo* studies of drug-AuNP conjugates to assess the ability of the nanostructures to provide an improved therapeutic benefit over treatment with drug candidates and radiation alone.

Introduction

Lung Cancer, Angiogenesis, and the Role of Integrins

As the leading cause of cancer deaths in the United States, lung cancer kills more people annually than breast, colorectal, and pancreatic cancers combined.[31,32] It is estimated that approximately 225,000 individuals will be diagnosed with the disease this year,[31,32] and the five-year survival rate is a mere 18%.[32] Representing 85% of total lung cancer cases, non-small cell

lung carcinoma (NSCLC) is a subset with heterogeneous histology, but these cases are similar in terms of treatment and prognosis.[31] For patients with early stage NSCLC, surgical resection is often the treatment of choice.[31] Although the removal of a partial or whole lung is highly invasive, five-year survival rates for early stage NSCLC are significantly higher: 30-50%.[31,32] Unfortunately, symptoms are often not present until the disease has progressed into Stage III or later at which point surgery alone is likely no longer the preferred course of action.[31,32] Instead, chemo- and radiotherapy are employed in attempts to shrink the size of tumors already present and prevent further metastases from forming. Such non-surgical techniques may also be used in earlier stage cancers in what are known as neoadjuvant and adjuvant therapies to make efforts to prevent the cancer from recurring.[31]

As oxygen can only diffuse effectively for a short distance from the nearest blood supply, a tumor experiences increasingly hypoxic conditions as it approaches 1-2 mm^3 in volume.[33,34] Under this stress, the protein hypoxia-inducible factor 1-alpha (HIF-1α) is stabilized, resulting in the upregulation of vascular endothelial growth factor (VEGF) transcription.[33,35] The release of VEGF by the tumor cells results in endothelial cell activation, proliferation, and migration until the sprouting capillary has sufficiently vascularized the tumor secreting the angiogenic factors.[33] Once in close proximity to the new capillaries, the increased nutrient supply leads to rapid tumor expansion as well as increased metastatic potential as the tumor begins to invade the walls of the blood vessels.[35]

One class of receptors on the surface of endothelial cells is the integrins.[36] These receptors allow the cells to interact with the extracellular matrix (ECM) and transduce signals across the cell membrance.[37] Composed of heterodimeric α and β subunits, there are at least 24 human integrins, many of which are specific for one or two proteins.[38] However, $\alpha_v\beta_3$ integrin is

a more promiscuous receptor that binds to a broader variety of proteins containing arginine-glycine-aspartate (RGD) sequences.[39] Disruption of the integrin-ECM interactions results in integrin-mediated apoptosis, and as this particular receptor is found overexpressed on activated endothelial cells and certain tumor types, it has become a prime target for anti-angiogenic therapies.[40]

Cilengitide

Over half of the known integrins recognize RGD sequences in their naturally occurring agonists. Such proteins include fibrinogen, fibronectin, vitronectin, collagens, von Willebrand factor, and several others.[38] Many studies have investigated using this conserved tripeptide to target integrins with anti-cancer or anti-angiogenic drugs,[41–43] with a variety of sequences and scaffolds having been explored, from block copolymers[44] to multi-kDa, branched dendrimers[45]. As the elucidation of the crystal structure for the $\alpha_v\beta_3$ binding pocket was not complete until 2002,[46,47] the original efforts of drug discovery focused on three things: cyclization of linear peptides to reduce the number of possible conformations, insertion of D-amino acids for spatial screening, and N-methylation to induce further conformational restraints.[23] One of the most promising to emerge was Cilengitide (Figure 2.1), a cyclic pentapeptide, c(RGDf(N-methyl)V), developed jointly in 1995 by the Technische Universität München and Merck-Serono.[23] Co-crystal structures of Cilengitide with $\alpha_v\beta_3$ integrin have since revealed the metal ion dependent adhesion site of the protein-binding ligand. This small molecule recently failed a CENTRIC Phase III trial investigating its use in mutliforme glioblastoma patients with a methylated MGMT promoter, meaning the subjects were also sensitive to the current standard of treatment.[48] Phase II data suggested there would be an increased response in patients given Cilengitide in addition

to the current standard of care,[49] and it is unclear why no significant difference materialized in Phase III.[48] Despite this setback, Cilengitide has also shown promise in Phase II clinical evaluations against NSCLC, another devastating disease with the biological hallmark of increased $\alpha_v\beta_3$ integrin expression.[50,51] Due to the Phase III failure of Cilengitide in the CENTRIC trial, however, the decision was made to no longer develop the small molecule into an anti-angiogenic drug to be used in combination with radiotherapy.[48]

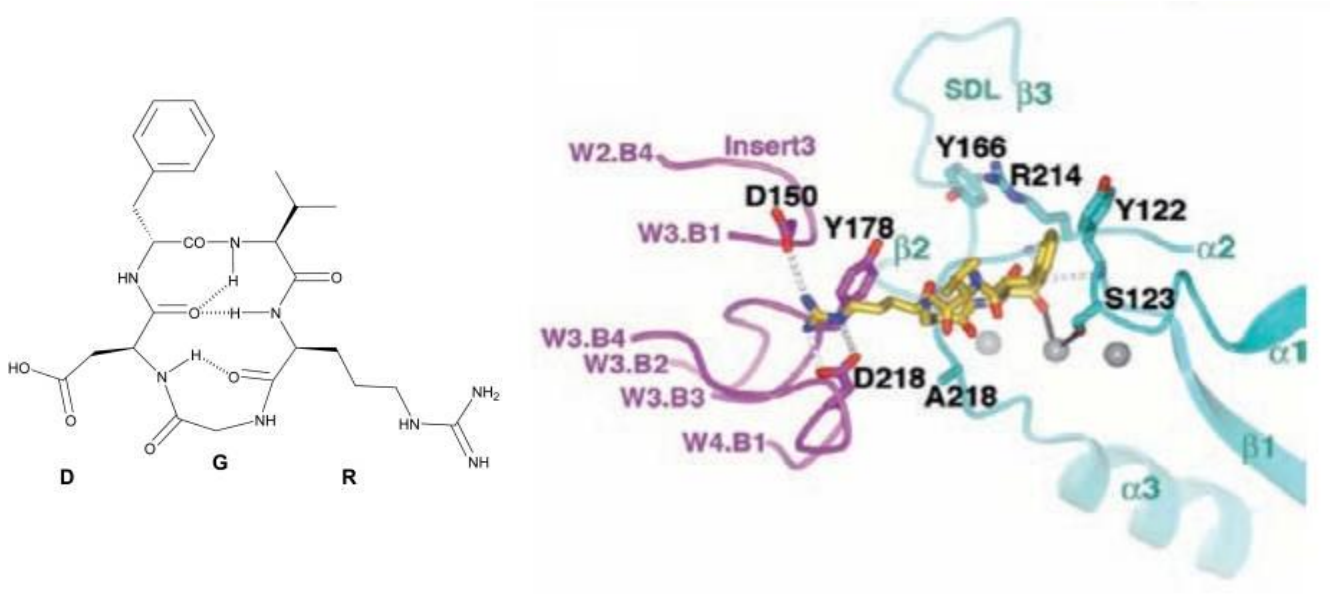

Figure 2.1: Structure of Cilengitide (left) and co-crystal structure of Cilengitide and $\alpha_v\beta_3$ integrin (right), revealing the ionic interactions between the protein and ligand.[23]

Radiosensitizers and Gold Nanoparticles

Although the efforts to develop Cilengitide into an anti-angiogenic drug were unsuccessful, several drugs have been approved by the FDA for their anti-angiogenic activity.[52,53] In 2004, a monoclonal antibody called bevacizumab became the first approved inhibitor of angiogenesis and is now used in a variety of treatment protocols, including those against certain NSCLC subtypes.[52,54] It specifically targets VEGF, resulting in slower growth of

new blood vessels, and is used in combination therapy with platinum-based drugs and paclitaxel, both of which are radiosensitizers.[55–57]

Compounds designated as radiosensitizers are those that enhance the effects of radiotherapy and can be classified into five categories based on their mechanism of action: "suppression of intracellular-SH or other endogenous radioprotective substances, radiation-induced formation of cytotoxic substances from the radiolysis of the sensitizer, inhibitors of post-irradiation cellular repair processes, sensitization by structural incorporation of thymine analogues into intracellular DNA, and oxygen-mimetic sensitizers, for example the electron-affinic drugs."[58] Metal-based drugs can be found in several of these categories and may be difficult to classify due to their multiple roles *in vivo*. Cisplatin, for example, is both electron affinic and can interfere with DNA repair mechanisms.[59]

Because of its biocompatibility, gold has been increasingly investigated as a radiosensitizer to take advantage of its high-Z number.[60] When incident radiation strikes a gold atom, several processes can lead to an enhancement of the effects of radiation *in vitro* and *in vivo*. At the lower energies of near-IR, the plasmons of gold nanostructures can be tuned to absorb light in the so called biological window to take advantage of primarily photothermal effects.[61] X-ray and gamma radiation, however, carry orders of magnitude more of energy and can cause the photoelectric effect, Compton scattering, and electron-positron pair production to occur.[60] These phenomena can not only result in localized hyperthermia as the nanostructures convert photons into phonons but can also lead to highly energetic, free electrons that are able to induce radical oxygen species.[62]

Due to the localized nature of the radioenhancement with gold, a mechanism is required by which the effects are concentrated in the area of interest, i.e. the tumor. Fortunately, a

biological phenomenon known as the enhanced permeability and retention (EPR) effect provides such a means of selectivity.[63] The EPR effect occurs due to the neovasculature of tumors being poorly sealed with tight junctions relative to that of normal tissue. These wide fenestrations allow higher molecular weight molecules such as gold nanostructures to extravasate into tumors whereas they would normally be retained within the circulatory system. Additionally, these regions also tend to be lacking in lymphatic drainage, allowing for the build-up of the nanostructures.[63]

Once anti-cancer compounds have left the bloodstream, their ability to penetrate deeply into the tumor plays a vital role in their efficacy, and multiple approaches have been explored to achieve this goal.[64–67] For example, the peptide known as iRGD can be conjugated to[64] or co-administered with[65] drug-delivering nanoparticles to enhance tumor penetration. A more passive means relies on the inherent diffusibility of small nanostructures. Multiple studies have demonstrated that smaller polymeric[68] and inorganic[66] nanostructures will diffuse more deeply than their larger counterparts. In fact, so important is the ability to penetrate beyond the tumor periphery that complex systems have been designed to release smaller nanoparticles from larger ones once they are exposed to proteolytic enzymes of the tumor microenvironment.[65,67]

Large enough to accumulate primarily in areas surrounding leaky vasculature but small enough to diffuse into the tumor, small AuNPs possess many desirable properties for potential radiosensitizers, notably biocompatibility, low toxicity, facile tunability, and selectivity.[69] In 2004, Hainfeld et. al. demonstrated the ability of 1.9 nm diameter AuNPs to passively target tumors *in vivo*.[70] In this study, mice receiving intravenous treatment with the AuNPs in combination with radiation exhibited dramatically increased survival times compared to all control groups. Furthermore, survival rates improved in a dose-dependent fashion. Since this first

demonstration of the ability of high-Z nanostructures to act as radiosensitizers *in vivo*, Hainfeld and others have published corroborative findings.[71–75]

Although small AuNPs appear to be effective at radiosensitizing cells, this radioenhancement factor can be improved upon by conjugating certain small molecules, such as folate[76] or glucose[77], to the particle surface to allow for more active targeting. The organic layer encapsulating the gold cores also plays a vital role in mediating *in vivo* responses, as studies have noted that the addition of polyethylene glycol to the surface can reduce unfavorable side effects.[19] In the case of peptides being presented from the surface of small AuNPs, it has been shown that, in addition to primary structure, the secondary structure of the peptides impacts the ability of the AuNPs to interact with immobilized antibodies.[78]

In the study presented here, small AuNPs are used as scaffolds to present peptides with the same amino acid sequence found in Cilengitide. The particles are passivated with tiopronin or glutathione to investigate any effects due to changes in the capping ligands, and peptides are attached in either a mono- or bidentate fashion to the AuNPs to determine the importance of the spatial constraint and secondary structure of the peptide. The number of peptides on the particles is also varied to explore any increased radiosensitization due to particle multivalency. Finally, the ability of the AuNPs to specifically target cells expressing $\alpha_v\beta_3$ is evaluated through the use of clonogenic assays against three different cell types.

Experimental Methods

Materials

Tetrachloroauric acid trihydrate was synthesized according to previous literature[79] and stored at -20°C, and a Millipore filtration system was used to prepare 18 MΩ•cm water.

Cilengitide and deuterium oxide were purchased from Selleck Chemicals and Cambridge Isotope Laboratories, Inc., respectively. Glacial acetic acid was purchased from EMD, and peptide synthesis reagents were purchased from AAPPTec. Tissue culture reagents were purchased from sources as indicated, and all other chemicals were purchased from Sigma-Aldrich and used as received unless otherwise noted. Cryovials of HUVECs, H460s, and MCF7s were purchased from ATCC.

Nanoparticle Synthesis

N-(2-mercaptopropionyl)glycine, also known as tiopronin (Tio), is a small molecule drug used for the treatment of cystinuria.[80] It has also found application in the synthesis of water-soluble AuNPs approximately 2 nm in diameter through a modified Brust synthesis.[81] Also of interest are similarly sized glutathione (GS) protected AuNPs as they too are relatively monodisperse structures. Briefly, these syntheses are accomplished by the addition of 3 eq of the thiol compounds to tetrachloroauric acid trihydrate that has been dissolved in 6:1 methanol:glacial acetic acid. Once the solution becomes colorless, reduction of the gold-thiolate structures is accomplished by the addition of 10 eq of $NaBH_4$ dissolved in a minimal amount of water. Three hours later, the solvent is removed, and the gold particles are redissolved in water and purified in SnakeSkin™ tubing (10 kDa MWCO) by dialysis against deionized water until the solution is free of excess ligand according to ^{1}H NMR. The resulting AuNPs are subsequently characterized by transmission electron microscopy (TEM) and thermogravimetric analysis (TGA) to acquire an average molecular formula for each particle type.

The Cilengitide mimic was of the sequence RGDfV$(PEG)_6$C and was synthesized through standard solid phase peptide synthesis (SPPS) techniques. Fmoc-Cys(Trt)-Wang resin

(0.20 g of 0.45 mmol/g substitution) was allowed to swell for 30 mins in DMF before being deprotected with 20% piperidine in DMF for another 30 mins. This was rinsed away through subsequent washings with DMF, methanol, and DMF again. Fmoc-NH-$(PEG)_6$-CH_2CH_2COOH was added in a 3 fold molar excess with respect to the substitution along with 6 fold excesses of HBTU and HOBT and 12 fold excess of DIEA. This was allowed to react for half an hour before being rinsed with DMF, methanol, and more DMF. The cycle of deprotection with piperidine, activation/reaction, and washing was repeated with each subsequent amino acid with the only change being 6 fold excesses of the amino acids. After the last wash step in this cycle, the resin was again deprotected, washed with DMF, and then washed with DCM. Cleavage was accomplished by adding the resin to 4 mL of a 90:5:3:2 v/v solution of TFA, thioanisole, anisole, and ethanedithiol for an hour. The resin was then filtered out with glass wool, and the peptide was precipitated into chilled ether. The precipitate was centrifuged out and washed five times with portions of chilled ether. Purification was achieved using reversed-phase HPLC with a Waters Prep LC 4000 System and LC Controller, and fractions were lyophilized. Peptide masses were confirmed using α-cyano-4-hydroxycinnamic acid and a Voyager DE-STR MALDI-TOF MS.

For the place exchange of the free peptide onto the surface of the particles, the tiopronin and glutathione protected AuNPs were dissolved in water at 3 mg/mL. Using the TEM and TGA data to calculate the average molecular formulae of the different samples, the free peptide was codissolved at the desired ratio of tiopronin to peptide, either 50:1 or 25:1. These solutions were allowed to mix for 3 days. Following purification through dialysis, the average number of peptides per particle was calculated using ^1H NMR and integrating the areas under the peaks attributed to the phenylalanine residue and either tiopronin or glutathione as appropriate.

A portion of each of these AuNPs was then subjected to an EDC/NHS coupling procedure for amide formation to loop the peptide back down onto the surface of the AuNP, resulting in the more spatially constrained Cilengitide mimics. A 1 mg/mL AuNP solution buffered with 0.1 M MES (2-(*N*-morpholino)ethanesulfonic acid) with 0.5 M NaCl at pH 6.0 was first created, and to this, EDC (1-ethyl-3-(3-dimethylaminopropyl)carbodiimide) and NHS (*N*-hydroxysuccinimide) were simultaneously added until they were at 2 mM and 5 mM, respectively. This was allowed to react for 2 hrs prior to quenching with hydroxylamine. Following further purification through dialysis, the AuNPs were filtered through a 0.2 μm filter to remove any particulates and microbial contamination. Gold concentrations of the filtrate were determined through ICP-OES using an Optima 7000 DV (Perkin Elmer), and AuNP concentrations were calculated using the previously determined average molecular formulae.

^{137}Cs Clonogenic Assays

Three cell lines were used for clonogenic assays: human umbilical vein endothelial cells (HUVECs), a large cell lung cancer (H460s), and a poorly invasive breast ductal carcinoma (MCF7s). The expression level of $\alpha_v\beta_3$ integrin varies among these cell types,[82] with HUVECs having high expression, H460s having moderate levels, and MCF7s having very little or none. HUVECs were cultured in F-12K Nutrient Mixture (Gibco) with 0.03 mg/mL endothelial cell growth supplement, 0.1 mg/mL Heparin, 10% FBS (Atlanta Biologicals), and 1% Fungizone (Gibco). H460s were maintained in RPMI-1640 (ATCC) with 10% FBS and 1% penicillin/streptomycin (Gibco). Lastly, MCF7s were cultured in DMEM +4.5 g/L glucose +L-glutamine (Gibco) with 10% FBS and 1% pen/strep. All cultures were incubated at 37˚C with

5% CO_2. Aqueous stocks of 10 mM Cilengitide were kept at 4˚C. Prior to plating in 60 mm tissue culture dishes, cells were trypsinized and counted with a hemocytometer. After being plated in their respective media, they were given 4 hrs to adhere to the dishes before being treated at 1 μM with Cilengitide, one of the six RGD-presenting AuNPs, or bare TioAuNPs or being left untreated as controls. These cultures were placed back in the incubator for an hour prior to being irradiated with either 0, 2, 4, or 6 Gy from a ^{137}Cs source. Post irradiation, the cultures were returned to the incubator for 24 hrs before the media was exchanged. Subsequently the media was exchanged once every three days for two weeks. At the end of the two week period, cells were fixed with a 2% paraformaldehyde solution, stained with 0.5% crystal violet in PBS, and visually counted using a digital colony counting pen with the aid of an inverted microscope. Only colonies containing at least 50 cells were counted. All collected data were fitted to weighted, stratified, linear regressions to determine coefficients for the linear-quadratic model of dose dependent cell survival through the use of SPSS statistical software.[83] Four variables were examined with respect to the DEFs, Equation 2.1: the density of the peptides on the surface of the AuNPs, the secondary structure of the Cilengitide mimics, the $\alpha_v\beta_3$ integrin expression level, and the identity of the capping ligand.

$$\text{DEF} = \frac{\text{Radiation Dose for 10\% Survival with Radiation Alone}}{\text{Radiation Dose for 10\% Survival with Radiation+Drug}} \qquad \textbf{(Equation 2.1)}$$

Results & Discussion

Nanoparticle Characterization

Characterization of the AuNPs through TEM revealed similarly sized particles synthesized through the tiopronin and glutathione syntheses, 1.8±0.5 nm and 1.8±0.7 nm in diameter, respectively (Figure 2.2). This allowed the potential variable of size to be held constant

during the evaluation of the varying particle types. Analysis of the AuNPs with TGA revealed the relative mass percentage of passivating staple structures to the inorganic core (Figure 2.3). This ratio was used to calculate the mass of Cilengitide mimic needed for the feed ratios. To evaluate the success of place exchange and purity of the product, ^{1}H NMR was used (Figure 2.4). This step ensured that no excess free ligand impacted the clonogenic assays as well as revealed the number of peptides per particle by determining the ratio of the signal of the aromatic residues to the signal arising from the passivating tiopronin and glutathione. ^{1}H NMR also provided evidence for the increased spatial constraint after EDC/NHS coupling; an increased ratio of amide protons was observed post-coupling as the linear peptide was tethered back onto the surface of the nanoparticle.

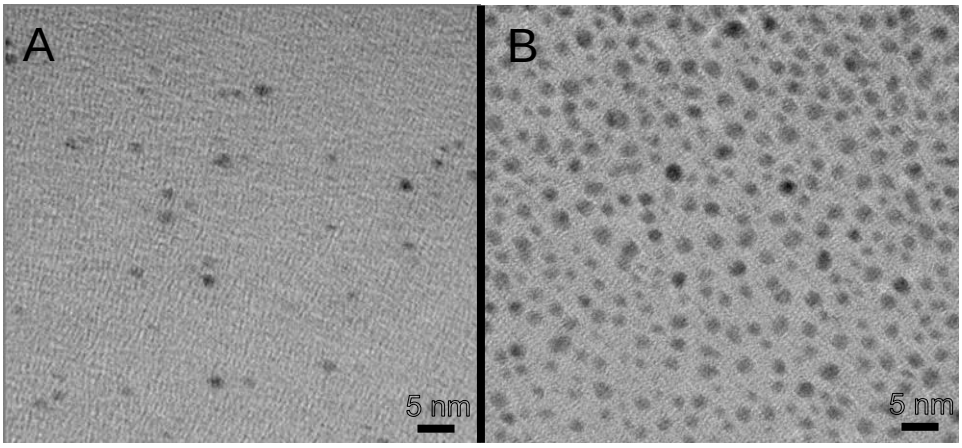

Figure 2.2: Transmission electron micrographs of nanoparticle samples. Images were obtained on a Phillips CM 20 TEM. (A) AuNPs were protected with a monolayer of tiopronin and are 1.8±0.5 nm in diameter. (B) AuNPs were protected with a monolayer of glutathione and are 1.8±0.7 nm in diameter.

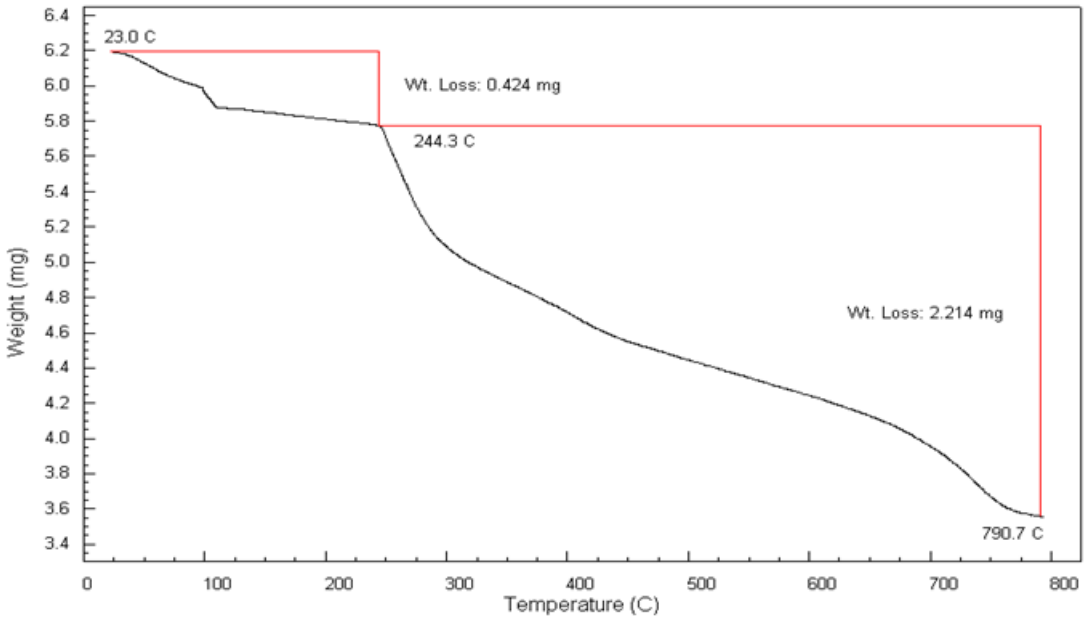

Figure 2.3: TGA curve of tiopronin-protected AuNPs. Plots were acquired on an Instrument Specialist's TGA-1000. The first step is due primarily to loss of water. The second and larger change corresponds to a loss of so-called "staple" structures that are composed of passivating thiolate ligands and gold atoms that have been pulled from the surface of the AuNPs.

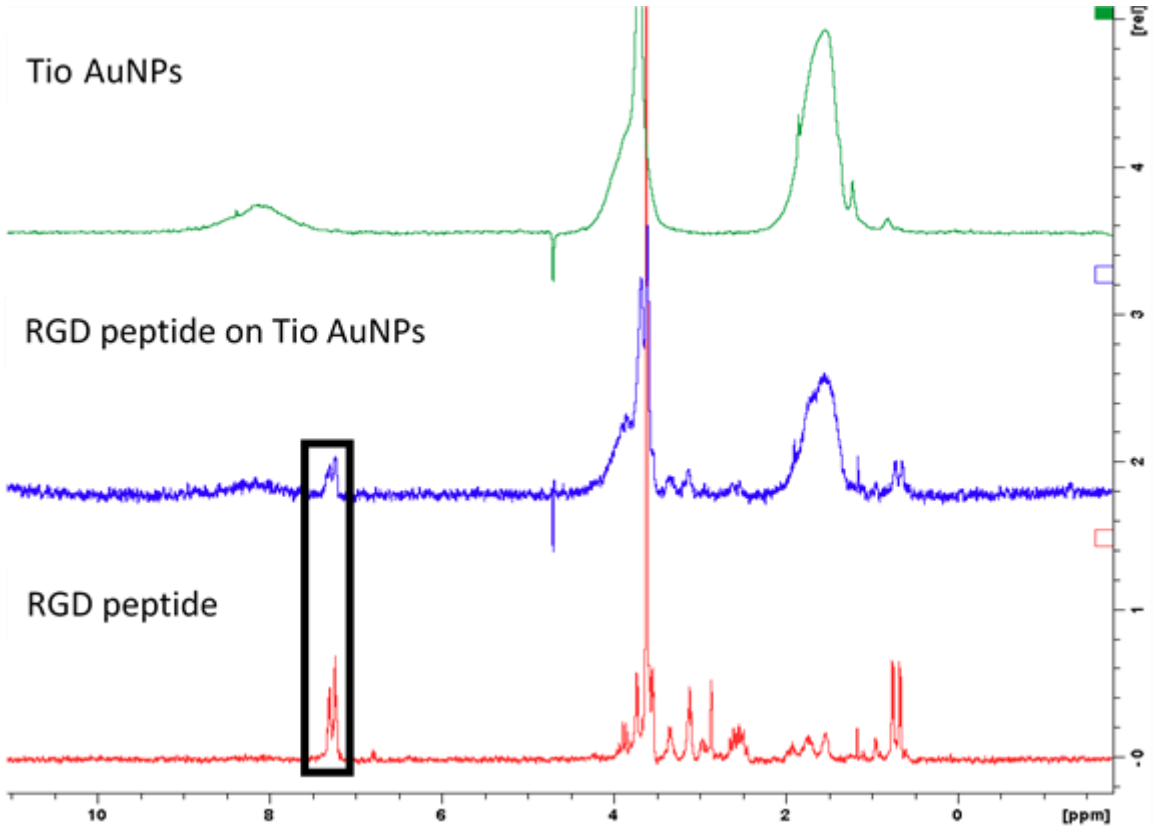

Figure 2.4: ^{1}H NMR spectra for Cilengitide mimics and AuNPs. Top: Tio AuNPs after purification and before place exchange. Middle: Tio AuNPs presenting the Cilengitide mimic. Bottom: Free peptide prior to place exchange. The highlighted box represents the signal from the aromatic phenylalanine sidechain that is used to quantitate the relative amount of peptide to tiopronin that has been place exchanged onto the particle.

In Vitro Activity

At the peptide density levels investigated, there does not appear to be a significant multivalent effect when the other variables (core-passivating ligand, secondary structure of the peptide, and cell type) are held constant (Figure 2.5). At greater numbers of peptides on the surface, an impact may arise, but solubility and unfavorable steric interactions between neighboring peptides become concerns. Increasing particle size would allow for more peptides to be place-exchanged onto the particle surface to further investigate the effect, but this would

decrease the diffusibility of the AuNPs into the interior of the tumor from the periphery. However, it is clear that the RGD peptides are playing a role in the interaction of the AuNPs with the cells, as particles without any targeting ligands, "Bare," exhibit no radioenhancement, essentially giving a trace of the radiation only curve (Figure 2.5). This is expected as the carboxylates of the passivating monolayer on the surface of the AuNPs are unlikely to have favorable interactions with the negatively charged cell membranes.

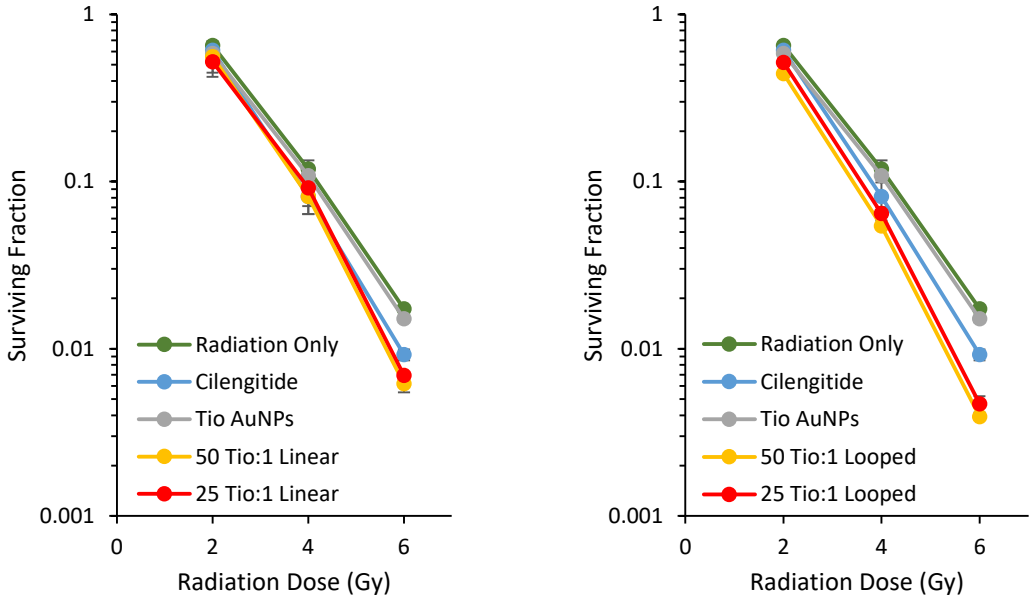

Figure 2.5: Results of clonogenic assays performed in triplicate using HUVECs treated at 1 µM and a ^{137}Cs irradiator. All particles were passivated with tiopronin, and ratios correspond to place exchange feed ratios. Left: Cilengitide peptide mimics were linear. Right: Cilengitide peptide mimics were looped. No multivalent effect was noted in either case, but significant differences exist between samples using targeted and untargeted AuNPs.

As anticipated, the secondary structure of the targeting ligand significantly influenced the ability of the AuNPs to radiosensitize the cells (Figure 2.6). The looped peptide, being spatially constrained and more accurately mimicking the natural agonists of $\alpha_v\beta_3$ integrin, outperforms its

linear counterpart when other factors are held constant. This finding agrees with previous results claiming that cyclic peptides and bidentate ligands bind more effectively to their targets.[78,84]

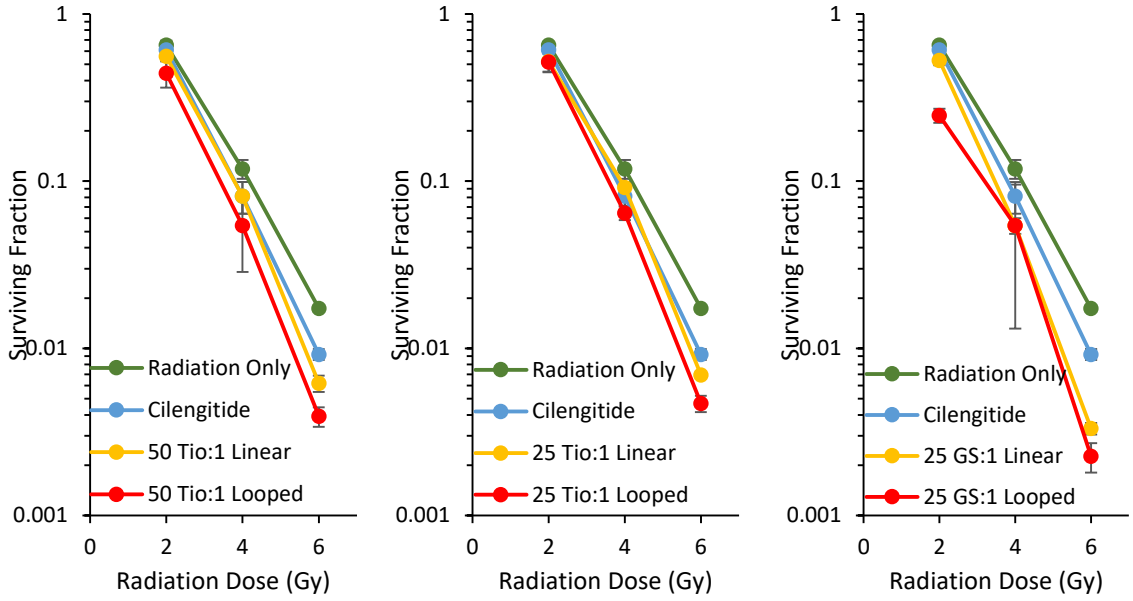

Figure 2.6: Results of clonogenic assays performed in triplicate using HUVECs treated at 1 µM and a ^{137}Cs irradiator. Ratios correspond to place exchange feed ratios. Left and center: Particles were passivated with tiopronin. Right: Particles were passivated with glutathione. In each case, AuNPs with looped peptides radiosensitized the cells to a greater extent than those with linear peptides.

An unexpected effect was observed when the thiolate forming the protective monolayer capping the AuNPs was changed (Figure 2.7). At physiological pH, tiopronin and glutathione have similar charges, so the electrostatic interactions between a nanoparticle and cell membrane should not have been significantly altered. However, previous studies have demonstrated that there are indeed differences in the *in vivo* activity of AuNPs protected with tiopronin and glutathione.[19,85] Although the basis for this is still undetermined, it is clear that even subtle changes to the monolayer can cause affect the interactions of the AuNPs with biological systems. One explanation for the increased radiosensitization seen in the GS AuNP samples is their ability

to interact with other membrane proteins, possibly gamma-glutamyl transpeptidase. This protein is known to be involved in the regulation and biosynthesis of glutathione in endothelial cells,[86] and the previously reported ability of folate-modified AuNPs to radiosensitize cells that overexpress folate receptor supports this hypothesis.[76]

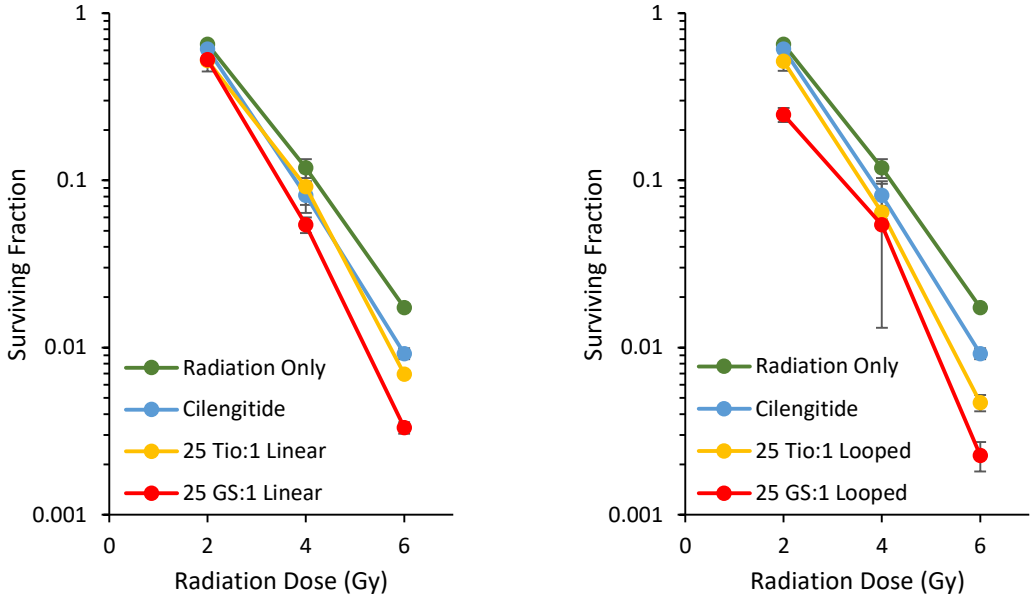

Figure 2.7: Results of clonogenic assays performed in triplicate using HUVECs treated at 1 μM and a ^{137}Cs irradiator. Ratios correspond to place exchange feed ratios. Left: Cilengitide mimics were linear. Right: Cilengitide mimics were looped. Despite having similar overall charges at physiological pH, AuNPs passivated with glutathione were able to more effectively radiosensitize cells than those protected with a tiopronin monolayer, suggesting that the backfill ligand on targeted AuNPs plays a greater role than core passivation alone.

The level of receptor expression plays a vital role in the ability of the targeted AuNPs to radiosensitize cells (Table 2.1). When used against MCF7 cells, no significant difference materialized between the radiation only control and the drug or AuNP treated samples. However, even at lower levels of expression as exhibited by the NSCLC H460 cell line, significant DEFs emerge for Cilengitide and all of the RGD-presenting AuNPs investigated. Finally, at the highest levels of expression, HUVECs demonstrate the greatest radiosensitivity following treatment.

This observed correlation of $\alpha_v\beta_3$ integrin expression to sensitivity to treatment with Cilengitide aligns with previous literature.[87]

	DEF at 10% SF		
$\alpha_v\beta_3$ Expression	HUVEC >	H460 >	MCF7
Cilengitide	1.08	1.06	X
25:1 Tio Linear	1.13	1.13	X
50:1 Tio Linear	1.12	1.09	X
25:1 Tio Looped	1.17	1.11	X
50:1 Tio Looped	1.23	1.14	X
GS Linear	1.20	1.15	X
GS Looped	1.42	1.15	X
Bare Tio	X	X	X

X $p > 0.05$, against irradiation only
$p > 0.05$, against Cilengitide treated
$p < 0.05$, against Cilengitide treated
$p < 0.01$, against Cilengitide treated

Table 2.1: Table of DEFs at 10% survival for all treatments across all cell types used. $\alpha_v\beta_3$ integrin expression levels are as follows: HUVEC > H460 > MCF7. No radioenhancement was observed for any treatments in cells lacking $\alpha_v\beta_3$ integrin. In H460 cells, the expression level is low, but cells are radiosensitized to approximately the same extent as they are with Cilengitide treatment. At higher expression levels, significant differences arise between samples treated with linear and looped peptides on AuNPs; it is also for these cells that differences are noted with respect to the capping ligand.

Presented here was the coinvestigation of four variables involved in the development of a gold nanoparticle that is small enough to diffuse into the interior of a tumor from the periphery while presenting targeting peptides that allow for selective radiosensitization of cells of interest. Although the number of targeting peptides per particle did not have a significant impact at the levels investigated here, their presence was clearly vital for radiosensitization, as seen when comparing the DEFs of targeted AuNPs against those of AuNPs passivated only with tiopronin. Also of importance is the secondary structure of the targeting peptides, as evidenced by the enhanced DEFs for all particle types tested in the HUVEC model after undergoing an EDC/NHS coupling reaction to loop the targeting peptides back down onto the particle surface, spatially constraining them. Unexpected effects arose when the passivating ligand was changed from tiopronin to glutathione when other factors were held constant. Like tiopronin, this endogenous

tripeptide has an overall negative charge at physiological pH, but particles passivated with glutathione were significantly more effective at radiosensitizing cells. The final variable, the number of receptors of interest on the cell membrane, was evaluated by utilizing cell lines with varying expression levels of $\alpha_v\beta_3$ integrin, and those with the greatest number of receptors were the most sensitive to the effects of ionizing radiation when incubated with gold nanoparticles.

The conclusions that can be drawn from this data have important implications for the growing field of biomimetic nanostructures. Because there was no apparent multivalent effect when the number of peptides per particle was increased, efforts should be instead focused on faithfully recreating the secondary structure of biomimetic peptides used for targeting specific cellular receptors rather than relying solely on their amino acid sequence to impart activity. The selection of surface passivating molecules is also non-trivial. Although it is well known that cetyltrimethylammonium bromide (CTAB), a surfactant used in the synthesis of gold nanorods, exhibits cytotoxicity,[88] other small molecules incorporated into protective monolayers may have properties that are difficult to predict *in vitro* and *in vivo*. Tiopronin-protected particles, for example, can cause renal damage despite the use of tiopronin in medical settings being to treat cystinurea and prevent kidney problems.[19] Although it is presently unknown from where the glutathione-protected particles gain their extra potency, future studies may probe this further, investigating a broader variety of short thiolates to cap the gold core. Perhaps the most important suggestion of this data is that these particles can not only be used to directly sensitize certain cancers that express $\alpha_v\beta_3$ integrin but that they could be used to destroy neovasculature to prevent tumors from being able to grow and metastasize. How effective they are at accomplishing this will be the focus of future studies examining both $\alpha_v\beta_3$ integrin positive and negative cell lines *in vivo*.

Chapter III

ENHANCING THE IMMUNOGENICTY OF GOLD NANOPARTICLES BY SPATIALLY CONSTRAINING BIOMIMETIC LIGANDS

This chapter describes an *in vivo* humoral immune response elicited by biomimetic nanostructures against a bacterial toxin. Specifically, antibodies against the protective antigen (PA) of *Bacillus anthracis* were elicited by subcutaneously inoculating mice with gold nanoparticles. These particles were passivated with a mixed monolayer of tiopronin and cysteine-terminated biomimetic peptides. To avoid deleterious side effects, the tiopronin was partially esterified with ethylene glycol (TioEG). Mono- and bidentate peptides representing an antigenic epitope of PA were investigated to determine how spatial constraint affects peptide immunogenicity when presented from the surface of monolayer protected clusters (MPCs). Competitive sandwich ELISAs were used to quantify anti-PA antibodies in the sera of control mice and those inoculated with the novel nanostructures. Although MPCs conjugated to the monodentate PA epitope mimic likely elicited anti-PA antibody production ($p < 0.10$), a humoral response was more strongly correlated with inoculation using the more spatially constrained hapten ($p < 0.01$). This demonstrates that the secondary structure of peptides used to create biomimetic conjugates should be optimized along with the more frequently investigated properties of size, surface charge, and shape of gold nanostructures. No adverse histological effects were observed in the inoculated mice, and ICP-OES measurements of blood, sera, and various organs indicate that MPCs undergo rapid renal filtration. These results suggest that biomimicry maintains the high degree of biological specificity that has allowed vaccination to revolutionize medicine while reducing the risks associated with current anthrax vaccines.

Introduction

Anthrax and BioThrax

Bacillus anthracis, the spore-forming pathogen responsible for anthrax, is a rod-shaped, Gram-positive bacterium found in soils and animal products such as wool and hair.[89,90] Despite only one or two reported anthrax cases per year in the US,[91] the poor prognosis associated with inhalation anthrax (below 15% survival with aggressive treatment)[92] coupled to its demonstrated use as a bioterrorism agent has spurred the search for improved anthrax prevention strategies, notably pre-exposure prophylaxis in the form of vaccination.[93–96] Investigated here is the ability of synthetic peptides representing an epitope of protective antigen (PA), the target of the only FDA-approved anthrax vaccine, BioThrax,[96] to stimulate anti-PA antibody production. This was evaluated as a function of the spatial constraint of the biomimetic peptides on the surface of gold nanoparticles (AuNPs) to determine the extent to which secondary structure should be investigated in emerging biomimetic vaccines.

Live attenuated and subunit vaccines confer immunity to anthrax, but concerns exist for these formulations.[95,97] Those employing live attenuated bacteria commonly use the Sterne strain lacking the poly-glutamate capsule that allows *B. anthracis* to avoid recognition by the immune system. However, the residual pathogenicity of the strain makes it an unsuitable inoculant in some animals and human populations.[89,90,94–96,98] As a result, the attenuated pathogen is not approved for human use in many countries. Subunit vaccines developed in the US and UK decrease this risk but may not be as effective at conferring immunity, requiring an 18 month vaccination schedule in addition to yearly boosters.[96,97] These subunit vaccines take advantage of the toxicity dependence of edema factor (EF), a calcium- and calmodulin-dependent adenylate cyclase, and lethal factor (LF), a zinc protease that cleaves mitogen-activated protein kinase

kinases, on PA to form the tripartite anthrax toxin.[97–100] Without the addition of PA, injections of LF and EF do not exhibit *in vivo* toxicity, as membrane-spanning oligomeric PA is required for translocation of LF and EF into the cytosol.[100,101] Only small amounts of EF and LF relative to PA are present within the subunit vaccines, created using a filtrate collected from a culture of toxin-producing, non-encapsulated *B. anthracis*. Thus, the observed humoral immune response largely results in anti-PA antibodies.[90,95] However, these poorly defined subunit vaccines have been shown to cause adverse reactions at the injection site for 30% of patients.[95] Numerous studies have been conducted to enhance the immunogenicity and improve the safety of the subunit vaccines by altering the inoculant and adjuvant.[102,103] In this study, synthetic peptides conjugated to biocompatible gold nanoparticles as a biomimetic alternative to inoculation with PA-containing filtrates were evaluated.

Biomimetic Vaccine Alternatives

The shift to biomimetics is expected to reduce the adverse effects associated with existing vaccination protocols while still stimulating or enhancing the desired humoral immune response. Using a single amino acid sequence from an epitope of PA as the inoculant allows for chemically defined and reproducible inocula, addressing concerns with current batch-to-batch variability.[95] The selection of the targeted epitope is non-trivial; it must contain an amino acid sequence corresponding to a solvent-exposed residue on the native protein to which elicited anti-PA antibodies can bind. Although antibodies could theoretically be elicited to any portion of the primary sequence of PA, only those that prevent the subsequent binding of PA to host cell receptors or EF/LF are likely to have a protective effect against anthrax. Therefore, the primary structure of the peptide epitope we investigated is found within a loop region of PA whose

binding to monoclonal antibody (mAb) 14B7 has been shown to inhibit the *in vivo* toxicity of anthrax toxin.[103]

The poor immunogenicity of small peptides is commonly remedied by conjugating them as haptens to carrier proteins such as keyhole limpet hemocyanin (KLH). Additives known as adjuvants are also commonly added to vaccine formulations to enhance the protective quality of the stimulated immune response.[104] Gold nanoparticles have previously been shown to be suitable replacements for carrier proteins as well as complete Freund's adjuvant (CFA) by stimulating an equivalent humoral immune response using only 1% of the total antigen required when using CFA.[105] Studies using AuNPs as the carrier have stimulated immune responses against amino acids, neurotransmitters, hormones, drugs, and antigens from bacteria, protozoa, and viruses.[106] In the case of biomimetic AuNPs bearing antigens from pathogens, the faithful reconstruction of the secondary structure of peptides and proteins conjugated to the nanostructures has been largely neglected. However, the effects of the size, surface charge, and shape of AuNPs have been explored with respect to *in vivo* activity.[106–110] The correlation of these properties with immune response allows for the design of nanoconjugates with tunable pharmacokinetics and pharmacodynamics. Previous studies[111] have also shown that bidentate, 'looped' peptides presented from AuNPs exhibit stronger binding affinities for biological targets compared to their monodentate, 'linear' counterparts. It is therefore hypothesized that spatially constraining biomimetic peptides found in a loop sequence of a PA epitope would enhance the desired humoral immune response.

The effects of spatial constraint on the immunogenicity of biomimetic nanoconjugates were investigated in a murine model. Mice were subcutaneously inoculated with AuNPs presenting no, linear, and looped PA-mimetic peptides and with saline as a control. To reduce

non-specific interactions, carboxylate-terminated AuNPs were esterified with ethylene glycol. Anti-PA antibodies in the sera of the inoculated mice were quantified with competitive sandwich ELISAs. The gold content of various organs was assessed post-mortem using ICP-OES to determine the biodistribution of the AuNPs. Additionally, kidney sections were taken to histologically identify any unexpected renal toxicity that has been previously observed[19] with some small AuNPs.

Experimental Methods

Materials

Tetrachloroauric acid trihydrate and DI water were sourced described in Chapter II. Borane-tert-butylamine (TBAB) was purchased from Acros Organics, and trace metal grade nitric acid, trace metal grade hydrochloric acid, and ethylene glycol were purchased from Fisher Scientific. Deuterium oxide and sterile 0.9% sodium chloride were purchased from Cambridge Isotope Laboratories, Inc. and Hospira, Inc., respectively, and were used as received. All other chemicals were purchased from Sigma-Aldrich and used as received unless otherwise noted.

Nanoparticle Synthesis

Synthesis of the TioEG MPCs was accomplished by adding 0.50 g tetrachloroauric acid trihydrate to 0.64 g tiopronin in 40 mL of ethylene glycol. This mixture was heated at 70°C for 7 min prior to reducing the precursor complexes with a solution of 1.10 g TBAB in 10 mL ethylene glycol that had been preheated to 55°C. This solution was held at 70°C and stirred for an hour before being allowed to cool to room temperature. The particles were then etched by adding 0.5 mL concentrated HCl and allowing to stir for 4 days. Clean-up proceeded by

removing the solvent via rotary evaporation and subsequently dialyzing the particles in 3.5 kDa MWCO SnakeSkin™ tubing against DI water for 7 days.

The initial characterization step was to assess purity via ^{1}H NMR using D_2O. Spectra were collected on a Bruker AV-400 of the TioEG MPCs after dialysis as well as the precursor compounds. To determine the extent of esterification, matrix-assisted laser desorption/ionization ion mobility mass spectrometry (MALDI-IM-MS) spectra of MPCs were collected using a Synapt HDMS (Waters Corporation) as previously described, and spectra were analyzed using the the MassLynx 4.1 software package (Waters Corporation).[112] Particles were sized using an FEI Tecnai Osiris transmission electron microscope, and thermogravimetric analysis was performed with an Instrument Specialist's TGA-1000 to determine the shell:core ratio of the particles.

Two biomimetic peptides were synthesized for place exchange. Both contained the sequence KYNDKLPLYISNPC, and the looped analogue contained an additional cysteine on the N-terminus. Both were synthesized, cleaved, purified, and characterized using the techniques described in Chapter II with slight modifications. The substitution of the resin was 0.7 mmol/g, and a 6-fold excess of amino acid was used relative to the resin loading. Additionally, the N-terminal amine was acylated prior to deprotection by incubating the resin for 30 min in 50% Peptides were place exchanged onto the MPCs using a ligand to peptide feed ratio of 25:1 by stirring in deionized water for 3 days at room temperature. After place exchange, MPCs were again purified via dialysis in 3.5 kDa MWCO SnakeSkin™ tubing against DI water, and actual tiopronin to peptide ratios were determined by integrating areas under the peaks in ^{1}H NMR spectra as described in Chapter II.

Animal Studies

Animals used for the *in vivo* studies were female, 16-17 week old BALB/cAnNHsd mice weighing 20-22 g (Harlan Sprague Dawley, Inc). They were housed under the supervision of full-time veterinarians and staff in a Vanderbilt Division of Animal Care (DAC) facility, which is fully certified by the Association for the Assessment and Accreditation of Laboratory Animal Care (AAALAC). Animals were given *ad libitum* access to food and water, and the animal room had a controlled photoperiod of 12 h on, 12 h off. All procedures were carried out in accordance with an Institutional Animal Care and Use Committees (IACUC) approved protocol. Mice were allowed one week to acclimate to their new housing prior to experimentation.

Each mouse was subcutaneously injected with a total volume of 200 μL MPC in saline or saline only solution. The two dosage concentrations used were 20 mg/kg (3 mg dissolved in 1.5 mL phosphate buffered saline (PBS)) and 80 mg/kg (12 mg dissolved in 1.5 mL PBS). Baseline blood and urine samples were collected 1 week prior to injection and at specific time points post-injection. Blood was drawn *via* submandibular bleeding[113] according to NIH bleeding guidelines.[114] NIH bleeding guidelines restricted multiple collections of the necessary blood volumes required for analysis from the same mice within one week, so each data point represents a unique mouse for the first 24 hours in Figure 1. Urine was collected on cellophane sheets while avoiding fecal contamination as described in the literature.[115] Blood and urine were analyzed for gold content *via* inductively coupled plasma optical emission spectroscopy (ICP-OES), and red and white blood cell counts were determined by complete blood cell count to monitor immune response. The mice were euthanized 4 weeks post-injection *via* CO_2 asphyxiation, and their organs were harvested for histological and trace metal analyses.

ICP-OES samples were prepared as previously described[19] with modifications. Trace metal grade nitric and hydrochloric acids were used to make aqua regia (3:1 hydrochloric acid/nitric acid). Blood and urine samples were prepared by diluting 5 μL of the fluid with 10% aqua regia in water for a total sample volume of 10 mL. Organs were weighed and dissolved in concentrated nitric acid for 48 h and heated to dryness. The organ residues were then reconstituted in 10% aqua regia in water for a sample volume of 10 mL. Blood and organ samples were centrifuged and decanted to remove remaining tissue and cellular debris. The values obtained for the organs were adjusted for weight and are presented as mass of gold per gram of organ. Measurements were made on a Perkin-Elmer ICP-OES Optima 7000 DV using a Burgener Peek Mira Mist® nebulizer with an argon plasma flow of 15 L min^{-1}, nebulizer flow of 0.65 L min^{-1}, auxiliary flow of 0.2 L min^{-1}, pump flow of 1.6 mL min^{-1}, RF power at 1450 W, and a delay time of 30 s. Spectra were collected at a wavelength of 267.595 nm in triplicate and averaged.

Blood was submitted to the Vanderbilt Comparative Pathology & Research Histology, Translational Pathology Shared Resource for complete blood count (CBC). 20 μL of whole blood samples were analyzed on a FORCYTE™ Veterinary Hematology Analyzer manufactured by Oxford Science Inc.

Organs were excised shortly after euthanasia, and sections of kidney were immediately fixed in 10% formalin, neutral buffered with 0.03% eosin and sent to Vanderbilt University Medical Center Immunohistochemistry Core Lab for hematoxylin and eosin (H&E) staining. The slides were interpreted by Ken Salleng, D.V.M., Vanderbilt University Division of Animal Care.

Materials from the Anthrax Protective Antigen 83 ELISA Kit Cat. No. 800-100-P83 from Alpha Diagnostic were used for all assays. The PA standard used in these experiments was

obtained from List Biological Labs, Inc. To each capture antibody-coated well, 300 μL wash solution was added and the well plate was left to stand for 5 min. The wash solution was discarded, and 100 μL of 1000 ng/mL PA standard was added to each sample well. 100 μL wash solution was added to the blank wells. After incubation on a plate shaker for 2 h, the solution was discarded, and the wells were washed 5x with 200 μL wash solution. In the wells used in the calibration curve, 100 μL 1:100 diluted anti-PA83 HRP conjugate from the kit was mixed with 0, 25, 50, 75, or 100 μL 1:100 diluted unlabeled anti-PA83 antibody 110 (Cat. No. C86110M, Meridian Life Science). In the serum wells, 100 μL HRP antibody was mixed with 100 μL 1:50 diluted serum from mice injected with saline, TioEG MPCs, looped PA-TioEG MPCs, and linear PA-TioEG MPCs. Blank wells again received 100 μL wash solution. The plate was again incubated for 2 h, and the solution was discarded before plates were washed 5x with wash solution. To quantify antibody production, 100 μL 3,3',5,5'-tetramethylbenzidine (TMB) substrate solution was added to all wells and allowed to develop in a dark drawer for up to 15 min. Once wells had developed a blue color, 100 μL stop solution (1% sulfuric acid) was added to all wells, turning them yellow. The absorbance was measured immediately afterwards at 450 nm on a BioTek Synergy HT plate reader.

Results & Discussion

Characterization of the biomimetic MPCs revealed that they were most likely of the formula $Au_{54}(SR)_{25}$ with approximately one PA peptide per cluster and with 50% of the tiopronin existing as esters of ethylene glycol and that they were free of excess ligand prior to being used as inoculants. The results of ICP-OES analysis on the blood (Figure 3.1), urine

(Figure 3.2), and organs (Figure 3.3) from mice inoculated with the TioEG MPCs and controls are shown below.

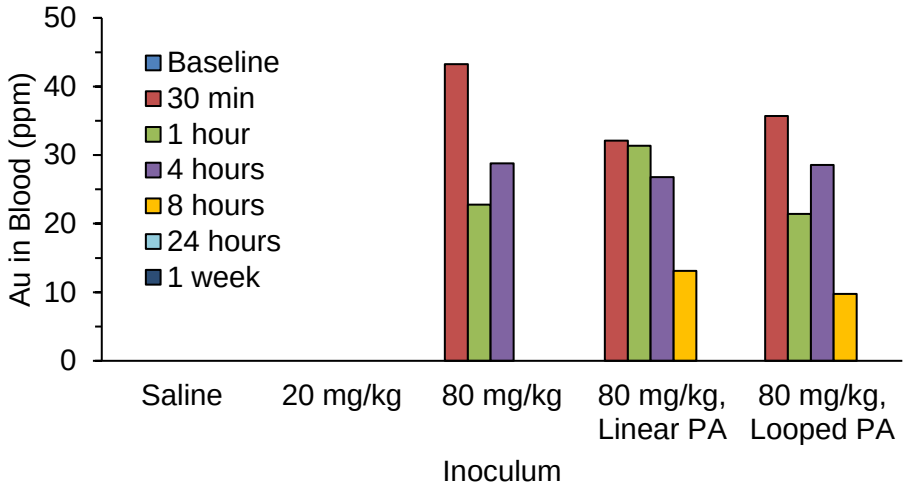

Figure 3.1: Gold concentrations in blood samples from mice inoculated with a saline control, TioEG MPCs, and TioEG MPCs presenting PA-mimetic peptide epitopes. Times given are time post-inoculation.

Due to their nanometer size, MPCs were rapidly cleared from circulation until the gold concentrations in the blood of MPC-treated mice were indistinguishable from those of the saline control. This occurred within 24 hours post-injection. Blood samples continued to be taken weekly for four weeks, but the level of gold in blood never rose back above baseline. Complete blood counts (CBCs) were also obtained for the weekly blood samples. For a normal, healthy mouse, red blood cell (RBC) counts range from 6.36-9.42 x 10^6 cells/μL, and white blood cell (WBC) counts range from 1.8-10.7 x 10^3 cells/μL. The observed fluctuations in WBC counts did not fall outside of these limits, and no statistically significant trend was observed.

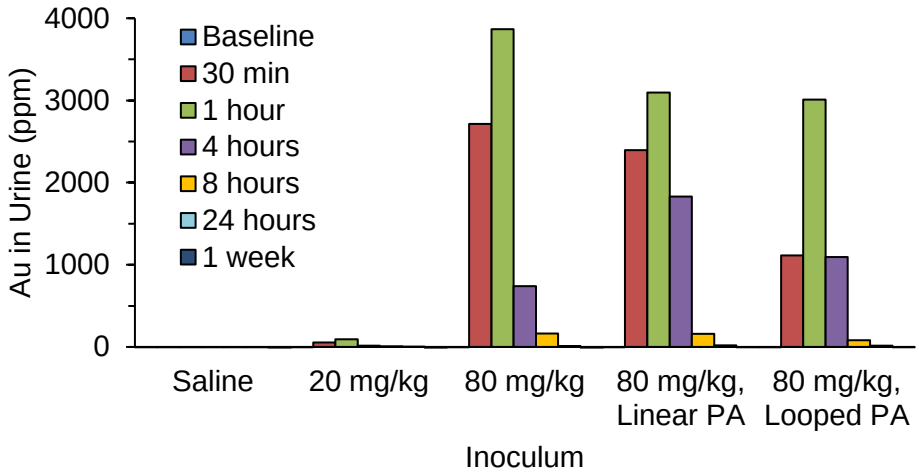

Figure 3.2: Gold concentrations in urine samples from mice inoculated with a saline control, TioEG MPCs, and TioEG MPCs presenting PA-mimetic peptide epitopes. Times given are time post-inoculation.

A considerable amount of the particles was eliminated through the urine as evidenced by the high concentration of gold in the urine, reaching a maximum of 3000-4000 ppm in the higher concentration groups at 1 h post-injection. As with the blood samples, decreases in gold concentration over time are noted in the urine for all three experimental groups given an 80 mg/kg dose. This rapid accumulation and subsequent decline of gold in the blood and urine suggests that the particles are cleared from circulation by renal filtration.

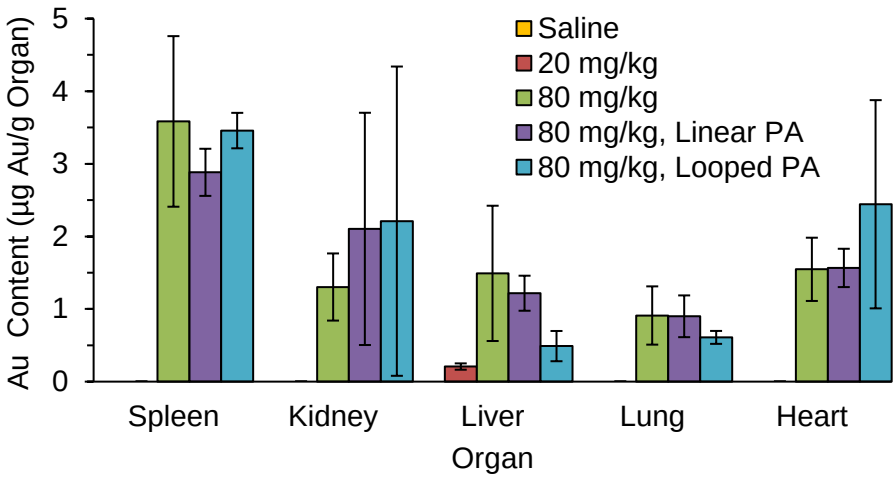

Figure 3.3: Gold content in organs from mice inoculated with a saline control, TioEG MPCs, and TioEG MPCs presenting PA-mimetic peptide epitopes. Error bars represent ± SD (n=5).

Some retention of gold was observed in the spleen, kidneys, liver, lungs, and heart 4 weeks post-injection at the time of euthanization (Figure 3.3). Three of these organs, the spleen, kidneys, and liver, play filtration roles, so the presence of gold in these organs was expected. Histological sections from one kidney of each mouse were also analyzed post-euthanization for adverse effects associated with inoculation with MPCs, but none were observed.

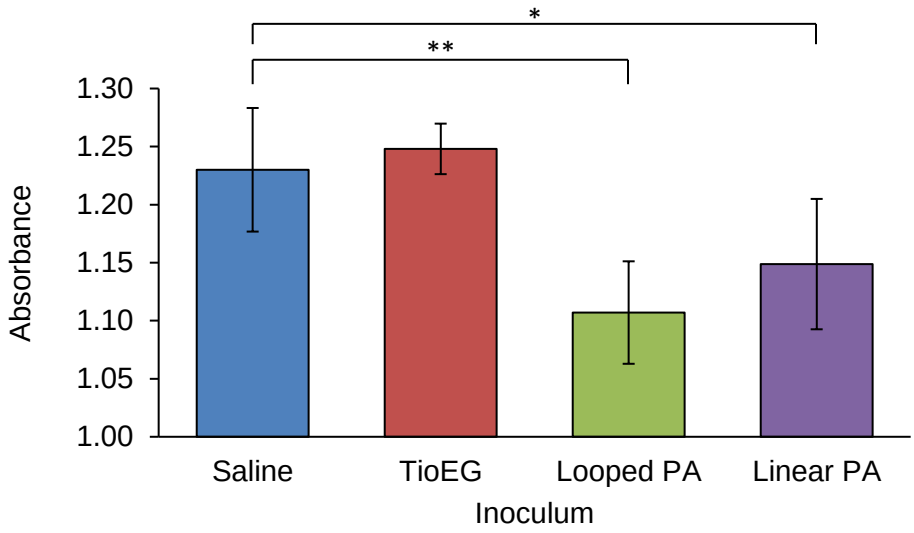

Figure 3.4: Absorbances with standard deviations measured in a competitive sandwich ELISA using the sera of mice inoculated with saline, 80 mg/kg TioEG MPCs, linear PA-TioEG MPCs, and looped PA-TioEG MPCs (n=4). Significant differences exist between saline controls and experimental groups (*$p < 0.10$; **$p < 0.01$).

Using a competitive sandwich ELISA, anti-PA antibodies were detected in the sera of mice inoculated with linear and looped PA-TioEG MPCs (Figure 3.4). Inoculation with AuNPs presenting the spatially constrained PA-mimetic peptides is more strongly correlated with a humoral immune response ($p = 0.0093$) relative to the monodentate linear peptides ($p = 0.074$). However, these values suggest that antibody production is elicited in both groups of mice, confirming the ability of the biomimetic AuNPs to stimulate antibody production.

The humoral immune response elicited by nanoconjugates has also been found to be dependent on the size and shape of the gold nanostructures to which the antigenic peptides or proteins are attached.[106,109,110] Spherical gold nanoparticles approximately 2 nm in diameter stimulate immune responses not unlike KLH.[110] AuNPs focus the immune response against the desired antigen, so that antibodies toward the nanoparticles themselves are not stimulated unlike what is observed when using large protein carriers. Further, the conjugation of peptides to

AuNPs increases their resistance to peptidases which may explain the role of AuNPs as adjuvants.[116–118] When larger AuNPs with poor tissue diffusibility are injected subcutaneously, a slow-releasing depot of antigen may form which is resistant to enzymatic degradation prior to first being internalized by antigen-presenting cells. Alternatively, very small particles diffuse through tissue more easily[66] and could localize in the lymphatic system where an immune response is more likely to be generated.

Chen and coworkers[119] identify a positive correlation between the concentration of immunogenic nanoparticles in the spleen and the specific Ab response detected. Consistent with this report, AuNPs with looped peptides on the surface accumulated to a greater extent in the spleen than did those with linear peptides ($p = 0.012$). The lack of severe adverse effects at the injection site and absence of renal damage suggest that the remaining residual gold within the body four weeks after inoculation is unlikely to present issues with biocompatibility despite not being completely cleared. This is particularly important as some small, negatively charged nanoconjugates have been shown to have severe deleterious effects in animal models.[19] By esterifying the passivating tiopronin layer with ethylene glycol, we aimed to avoid these effects while simultaneously shifting the biodistribution from the liver to the spleen. Additionally, the PEGylation step likely increased the circulatory half-life of the nanoconjugates, allowing more time for a specific antibody response to occur.

The secondary structure of peptides on the surface of nanoparticles has been shown to affect the affinity of particles for biomolecules such as antibodies.[111] Synthetic routes to achieve the different conformations have relied on capping one or both ends of biomimetic peptides with cysteine residues[111] and altering the buffer concentration and pH,[118] and unnatural amino acids can be used to induce turns in peptide chains.[120] With regard to vaccine formulation, spatial

constraint has been identified as an integral step toward successful immunogen development as peptides with more flexible structures tend to afford poor protection after a challenge.[118] This method of biomimetic peptide design is somewhat limited by the need to first identify the immunogenic target that gives rise to protective immunity.

BioThrax[96] takes advantage of PA, a known target for vaccination.[102,103] Also known as anthrax vaccine adsorbed, or AVA, this formulation uses aluminum hydroxide as the adjuvant to assist in stimulating the immune system.[96,102,103] Studies have shown that antigens may actually become less stable when they are adsorbed to aluminum salts, making them more susceptible to degradation by antigen presenting cells.[121,122] In the case of gold nanoparticle adjuvants bearing biomimetic peptides, the inverse plays a role in their adjuvant properties; small peptides conjugated to nanostructures are more resistant to proteolysis.[116–118] The bidentate nature of the looped peptides likely further increases the resistance to proteolysis, allowing more complete sequences of interest to emerge from antigen processing and stimulate the desired humoral immune response.

With these *in vivo* studies, TioEG MPCs have been shown to be promising candidates as carriers for conformational peptide mimics of an epitope of the protective antigen of *B. anthracis*. TioEG MPCs were only in circulation for 24 h, but this, combined with their organ residence, particularly the spleen, was sufficient for the mice inoculated with looped, and to a lesser extent linear, PA peptide functionalized MPCs to produce specific anti-PA antibodies, as determined by competitive sandwich ELISA. Overall, place exchanging short peptides of interest onto stable, water soluble gold nanoclusters to stimulate a naïve immune response may represent a tunable, relatively simple, and safe vaccine platform as no adverse effects were seen in the histological samples.

Chapter IV

TUNING THE PATTERNING OF LIGANDS ON THE SURFACE OF GOLD NANOPARTICLES

The two previous chapters detailed the place exchange of biomimetic peptides onto gold nanoparticles passivated by thiolates, resulting in a mixed monolayer. The manner in which mixed monolayers such as these self-assemble is another lesser examined surface property of nanomaterials. This chapter focuses on the phenomena leading to the emergence of nanoscale patterning, synthetic methods to obtain specific patterns of interest, characterization methods to probe the patterning of surface ligands, and applications of nanoscale patterning.

Introduction

Nanoscale Patterning

The ability of ligand mixtures to form non-random patterns on metal surfaces has been known for many years.[123] However, accurately predicting the patterns that arbitrary ligand combinations will form on a surface remains an active area of research. Mixtures of two alkanethiolates varying only in their solution-exposed termini were once believed to disperse in approximately random distributions across a surface, but STM experiments provided evidence against this.[124] Even seemingly small differences between ligand types, such as the alteration of a tail group from a methyl to a methyl ester, resulted in the emergence of distinct domains. Time-dependent STM studies also revealed that these domains were not static features; the domains had a tendency to coalesce and grow in size over time.[124] In the past decade, this property of phase segregation between two ligand types has been extended to the surface of spheres, and

several distinct patterns have been reported: patchy domains, stripes, and Janus separation.[125,126] Which of these nanoscale patterns will emerge depends on the entropic and enthalpic interactions among the surface ligands and has been the study of various studies.[125–129]

Entropy is the main factor leading to a truly random mixed monolayer of ligands.[125,127] This lack of order occurs in mixed monolayers of miscible ligands, typically similar in polarity, length, and bulkiness. With minimal steric or electrostatic forces at work, ambient temperatures provide enough energy to allow the ligands to comingle in a random fashion. As differences in the ligands arise in the form of conflicting hydrophobicity, bulkiness, and/or length, the degree to which the ligands mix notably decreases as a result of several factors. First, the juxtaposition of bulky groups is unfavorable when there are other, less-sterically hindered sites available. Mismatched ligands in terms of length exhibit similar behavior as the longer ligand prefers to maximize its rotational cone angle. It does this by being adjacent to shorter ligands whose termini do not extend as far away from the AuNP surface, providing more volume for the mismatched portion to rotate freely and thus increasing interfacial entropy. Such interactions would be responsible for the stripe formations reported by STM[125,129,130] and *in silico*[127,128] methods.

In systems where the difference between the two ligands is less pronounced, the monolayer may instead choose to undergo partial phase segregation into homogenous domains with more favorable enthalpic interactions between ligands of the same type.[129] The final known pattern on the surface of nanospheres requires the complete segregation of the different capping molecules to form Janus nanoparticles (JNPs).[125,126] Named for the two-faced Roman god, JNPs exhibit a complete separation of the ligands by keeping the interface between the two to a minimum. On a sphere with equal amounts of two ligand types, this equates to hemispheres each

exclusively presenting one ligand. When the separation of the ligands is at this maximum, enthalpy almost entirely is the driving force. By using two immiscible thiols with roughly equal length and bulkiness, no substantial entropic gain is observed by increasing interfacial interactions. In fact, by increasing the number of interfacial sites, favorable enthalpic interactions decrease, negatively impacting the overall free energy of the system.[125] This is not, however, the only path to creating Janus gold nanoparticles (jAuNPs). When the curvature of the particle becomes sufficiently large as is seen in AuNPs smaller than 1.5 nm in diameter, entropic considerations from interfacial sites become less important as the packing density for the ligands on the gold surface decreases.[125] The increased reliance upon enthalpy for patterning results in ligands of the same type aggregating on the surface to maximize their favorable interactions with their neighbors.

Characterization Methods for Nanoscale Patterning

To ascertain the degree of separation of the ligands at the <5 nm regime, there are four known techniques: Nuclear Overhauser effect spectroscopy (NOESY),[131] contact angle measurements,[132] STM,[125] and matrix-assisted laser desorption/ionization ion-mobility mass spectrometry (MALDI-IM-MS).[126] NOESY is a form of NMR that allows for evaluation of through-space interactions. For JNPs, one can determine if the hydrogen nuclei of the different ligands are close enough spatially to exhibit cross relaxation. The presence of cross peaks in the spectrum is then indicative of the ligands mixing on the surface rather than phase segregating.[131] The main drawback of this method is the broadening of NMR peaks seen when ligands are attached to nanoparticles. This broadening can result in difficult-to-interpret spectra if the crosspeaks for hydrogen nuclei on different ligands significantly overlap with those originating

from same-ligand interactions. Less ambiguously, contact angle measurements are useful for amphiphilic JNPs formed through Langmuir-Blodgett methods. Values are compared for mixed monolayer particles and uniform SAMs, with no difference indicating fully exchanged surface-exposed faces of the various AuNPs. This method is limited in that it requires extreme differences in the hydrophobicity of the different hemispheres which may not be feasible for some applications. With 1 Å resolution in the XY plane and 0.1 Å resolution in the Z direction, STM provides topographical measurements of the surface of the nanoparticles and does not rely on chemical functionalities. Such atomic resolution is achieved by the tunneling of electrons from the ligand termini to the STM tip which creates a measurable current. This allows the boundary between the two ligand types on a JNP to be distinguished due to the disparity of the ligand lengths (Figure 4.1A). Controversy exists within the claims that STM can also be used to observe stripes on the surface of nanoparticles when Janus separation does not occur.[133] Due to the data being collected at the very limit of the method's achievable resolution, images obtained to substantiate the stripes are difficult to interpret and separate from the noise (Figure 4.1B).

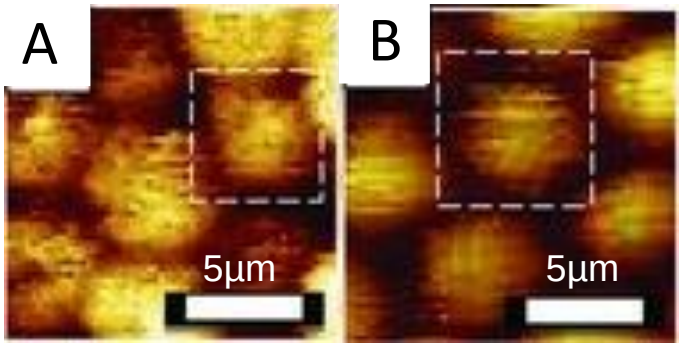

Figure 4.1: STM images of nanoparticles exhibiting (A) Janus separation and (B) striped patterning of surface ligands.[125]

To reduce the uncertainty associated with STM, MALDI-IM-MS can be used to quantitatively characterize the degree of phase separation.[126] Crystal structures of AuNPs have demonstrated that, rather than being loosely adsorbed to faces of the core, the passivating thiolates exist in distinct staple-like structures that pull gold atoms away from the core.[134–136] As

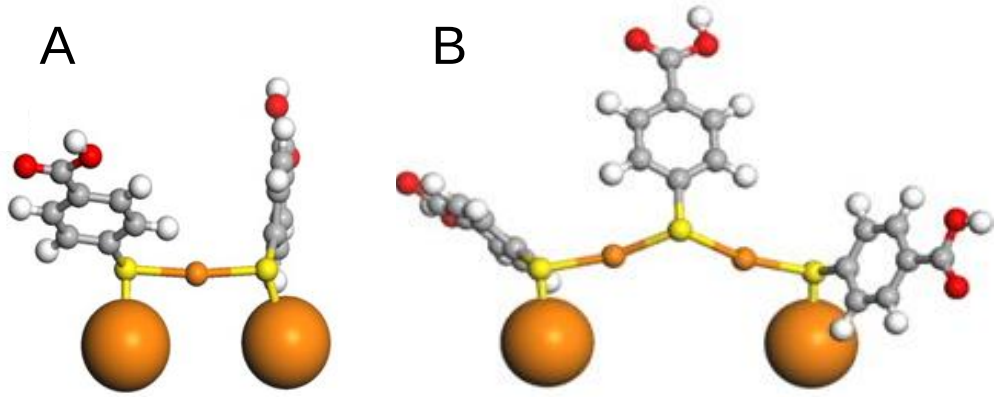

Figure 4.2: Staple structures on the surface of AuNPs passivated by p-mercaptobenzoic acid as determined by X-ray crystallography. The structures can pull either (A) one or (B) two gold atoms away from the gold core using either two or three thiolates, respectively. Large orange spheres represent gold atoms of the core. Small orange spheres represent gold atoms pulled away from the core. Yellow spheres represent the sulfur atoms of the p-mercaptobenzoic acid thiolates.[136]

the AuNPs are ablated by the laser, $Au_4Ligand_4$ clusters appear that are believed to arise from adjacent staple structures. These complexes first pass through the ion mobility flow cell within which is an inert gas. Based on the collisional cross section of the different species in the flow cell, there exists temporal resolution as the smaller ions are the first to exit the flow cell. These ions are then introduced into the TOF-MS portion of the instrument. The resulting spectra from such experiments are three-dimensional and can be used to establish precisely where tetrameric gold rings are beneath a plume of organic noise unresolvable in TOF-MS alone (Figure 4.3). Assuming a random assembly on the particle surface, a binomial distribution model can be created for the prevalence of $Au_4Ligand_xLigand'_{4-x}$ species, Equation 4.1.

$$P(X=k)=\binom{n}{k}p^k(1-p)^{n-k} \qquad \textbf{(Equation 4.1)}$$

The mole fraction of one ligand, say L, is given as *p*. The number of ligands in the gold-sulfur cluster, 4, is *n*, and the number of L of the four ligands in the cluster is given as *k*. The deviation from this binomial model, measured as the residual sum of squares (RSS) in Equation 4.2, can then be used as a quantitative method for determining the extent of phase segregation within the monolayer.

$$RSS=\sum_{k=0}^{4}(P_{observed}-P_{predicted})^2 \qquad \textbf{(Equation 4.2)}$$

P is the probability dictated in the binomial mass distribution equation, and *k* remains the number of L of the four ligands in the gold-sulfur cluster, ranging from zero to four. This method is the most quantitative and may become the preferred method of characterization.

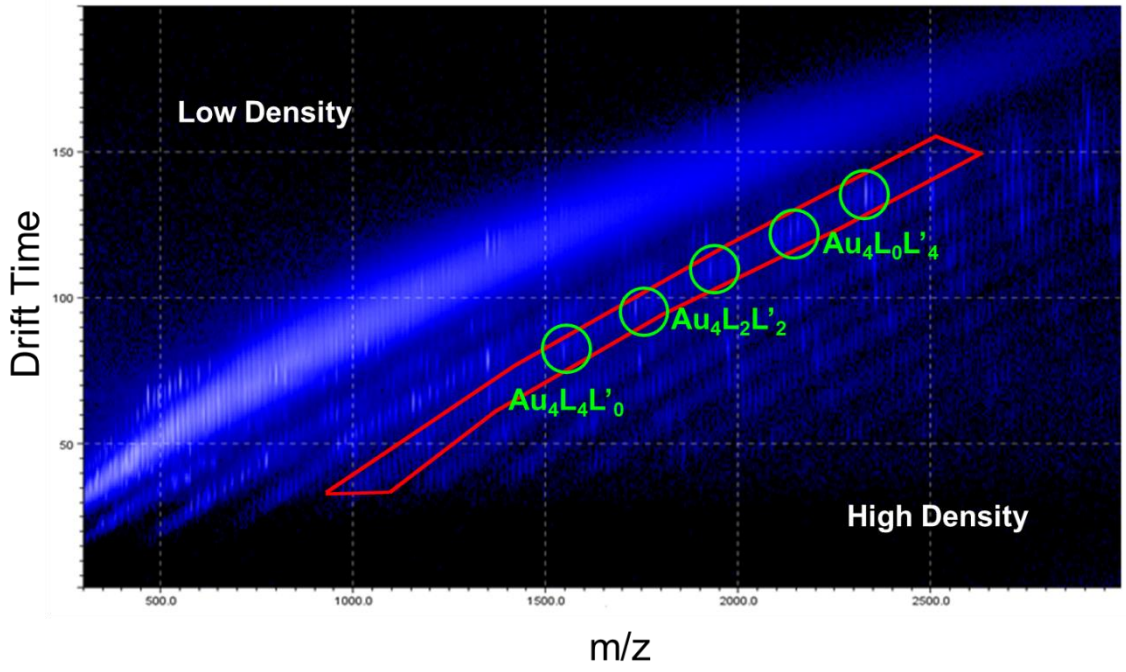

Figure 4.3: Three dimensional MALDI-IM-MS spectrum of Tio/MUTEG AuNPs. The red band represents Au_4 species, and the green regions contain signals from $Au_4Tio_xMUTEG_{4-x}$ species. Comparing this data to a binomial distribution model yields information on nanoscale patterning.

Applications of Anisotropy

Many biological processes require the breaking of symmetry.[137] These include some of the most vital cellular events, including cellular division. Intercellular interactions also rely on structural polarity. This allows epithelial cells to differentiate the interior of an organism from the exterior and subsequently perform their specialized functions. At the molecular scale, anisotropy plays a significant role in the adaptive immune system.[138] The structure of antibodies is such that they are composed of two distinct regions: F_{ab} and F_c. The antigen binding fragment, F_{ab}, is highly variable and affords the specificity that antibodies exhibit for antigens. The F_c portion is far less variable and thus crystallizable. Variations in F_c regions are specific to different classes of antibodies and mediate binding between complement proteins and the F_c receptors on cells of the immune system. This binding results in the activation of cytotoxic and phagocytic pathways. The spatial separation of the different antibody functions allows the process of opsonization to efficiently eliminate threats presented by circulating pathogens.

Many directionally dependent nanostructures have been utilized for their unique optical, theranostic, catalytic, and interface-stabilizing properties,[139] and JNPs also show promise for biological applications. One might reasonably expect JNPs to interact with cells in a manner distinct from randomly patterned particles as properties such as the size, shape, coating, and rigidity also affect their interactions.[140,141] Several studies have indeed shown that JNPs interact with the cell membrane in a directionally-dependent fashion. Notably, they can be used to create single particle layers on the surface of a cell, and the dynamics of particle uptake change when the ligands extending from the particle surface are reserved to one face of the sphere.[142] The ability to interact in a face-specific fashion with one cell could potentially be extended to a second cell. Thus, JNPs could someday serve as a means to bridge intercellular structures such as

the immunological synapse between antigen-presenting cells and T lymphocytes. This chapter investigates methods to fabricate such bridging JNPs. Previous ligand combinations giving rise to nanoscale Janus patterns are modified to facilitate orthogonal functionalization with different as a first step toward this goal.

Synthetic Routes to Janus Particles

With the expanding repertoire of these structures comes an abundance of synthetic techniques that fit into three categories: masking, emulsions, and ligand self-assembly.[143] Of these, only self-assembly has been reported to form JNPs with diameters of <5nm.[126,143] In this method, the entropic and enthalpic contributions from the interactions of the ligands give rise to the distinct hemispheres. Through computational studies,[127] it has been suggested that ligands of identical length but differing tail groups, i.e. carboxyl vs methyl terminated short alkane thiols, will separate as if the ligands were unbound and immiscible. As the difference in bulkiness or length between the two ligands increases, however, the ligands begin to mix with one another to maximize the interfacial entropy due to the increased volume of the cone angle for the longer or bulkier ligand. As the curvature of the particle increases with decreasing core diameter, it is predicted that this effect disappears as the system loses the close packing between ligands, allowing for a greater distance between the organic molecules extending outward from the gold core.[125]

Several JNP-inducing ligand combinations have been explored and reported in the literature.[125,126,131] Of these, AuNPs passivated by a mixed monolayer of tiopronin and mercaptoundecyltetra(ethylene glycol) (MUTEG) are the most promising for biological applications due to their solubility in water. The carboxylates of tiopronin are readily conjugated

to peptides through EDC/NHS coupling reactions as described in Chapter II, and the PEGylation afforded by the MUTEG may reduce the adverse biological effects seen in particles passivated only by tiopronin.

Initial on-particle attempts to convert the alcohol of MUTEG into a more reactive group through a tosylate intermediate were unsuccessful. The AuNPs irreversibly precipitated, possibly as a result of polymerization of neighboring particles. To avoid this, a synthetic strategy was devised to convert the terminal alcohol to an azide prior to particle formation (Figure 4.4). Such azide-terminated ligands can then be used for facile click chemistry reactions to couple AuNPs with alkyl-functionalized peptides.

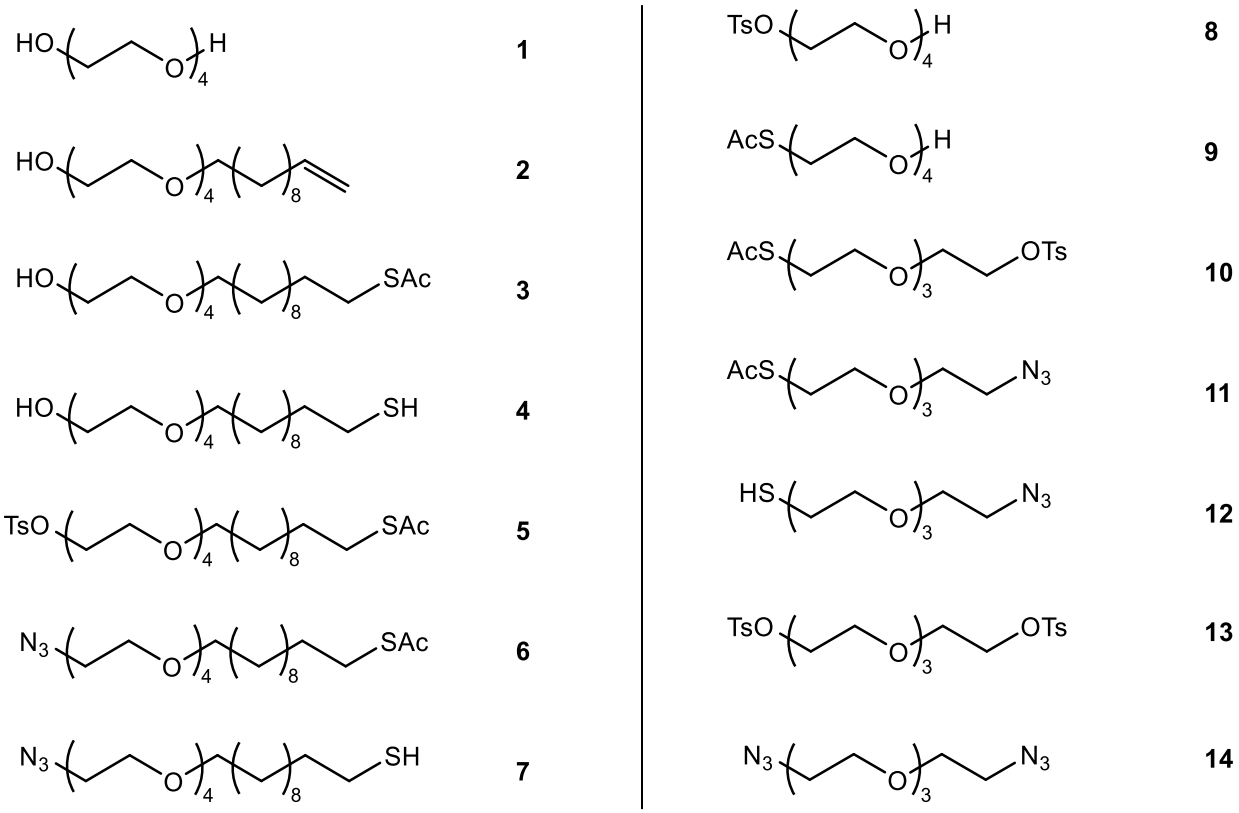

Figure 4.4: Azide- and intermediates to azide-terminated PEGs devised to exhibit Janus patterning in combination with Tio AuNPs (**1-12**). Also shown are symmetric derivatives of tetraethylene glycol designed for orthogonal functionalization of water soluble JNPs, specifically the dimerization of JNPs to form ultrasmall AuNR mimics (**13-14**).

Experimental Methods

Materials

Deuterated solvents were purchased from Cambridge Isotope Laboratories, Inc. Other solvents and reagents were sourced as described in previous chapters or purchased from Sigma Aldrich. All chemicals were used as received.

Ligand Syntheses

Compound **2**, TEG-C_{11}-ene: 4.0 to 20.0 mmol of 50% NaOH in water was added to 10 eq of Compound **1**, TEG. Under an atmosphere of N_2, this mixture was heated to and held at 100˚C with stirring. After 30 mins, 1 eq of 11-bromo-1-undecene was added, and the reaction continued for another 24 hrs. After the solution cooled to room temperature, the crude product was extracted six times with hexanes. Compound **2** was then purified further from this crude product on a silica column using an ethyl acetate mobile phase. Rotary evaporation of the fractions gave a pale yellow oil at 63% yield. ^{1}H NMR (400 MHz, $CDCl_3$) δ 5.82 (m, 1H), 4.96 (m, 2H), 3.57-3.75 (m, 16H), 3.45 (t, 2H), 2.04 (q, 2H), 1.58 (qui, 2H), and 1.25-1.42 (m, 12H).

Compound **3**, TEG-C_{11}-SAc: A solution of 400 mM Compound **2** was prepared in methanol. To this, 4 eq of thioacetic acid and 4 mg of azobisisobutyronitrile were added. This mixture was then irradiated under a mercury UV lamp for six hours. The methanol was removed under rotary evaporation, and the crude product was purified on a silica column using a mixture of ethyl acetate and hexanes as the mobile phase. Compound **3**, a yellow oil, was obtained in 83% yield. ^{1}H NMR (400 MHz, $(CD_3)_2CO$) δ 3.50-3.63 (m, 16H), 3.42 (t, 2H), 2.85 (t, 2H), 2.29 (s 3H), 1.54 (m, 4H), and 1.26-1.41 (m, 14H).

Compound **4**, TEG-C_{11}-SH: Deprotection of the thioacetate to afford the free thiol was

accomplished by refluxing up to 250 mg of Compound **3** in 1.0 M HCl in methanol for 4 hours under an atmosphere of N_2. The mixture was neutralized using aqueous 0.1 M NaOH prior to extraction of the product with diethyl ether. The ether was removed using rotary evaporation, and the product was loaded onto a silica column and eluted with a mixture of hexanes and ethyl acetate. The resulting yellow oil was used within 24 hrs. ^{1}H NMR (400 MHz, $CDCl_3$) δ 3.56-3.75 (m, 16H), 3.45 (t, 2H), 2.60 (m, 2H), 1.58 (m, 4H), and 1.21-1.43 (m, 14H).

Compound **5**, Ts-TEG-C_{11}-SAc: Up to 5.0 g of Compound **3** was dissolved in 30 mL of dry acetone. To this was added 2 eq of triethylamine (TEA) and 1.1 eq of p-toluenesulfonyl chloride (TsCl). The reaction proceeded with stirring under a N_2 atmosphere for 4 hours. The solid byproduct was removed using gravity filtration, and the filtrate was washed thrice with brine. Removal of the solvent resulted in a heterogeneous mixture which was loaded onto a silica column for purification. Mixtures of hexanes and ethyl acetate were used as the mobile phase, and the final product was a peach-colored oil at 85% yield. ^{1}H NMR (400 MHz, $(CD_3)_2CO$) δ 7.81 (d, 2H), 7.49 (d, 2H), 4.16 (t, 2H), 3.67 (t, 2H), 3.49-3.59 (m, 14H), 3.41 (t, 2H), 2.85 (t, 2H), 2.47 (s, 3H), 2.29 (s, 3H), 1.53 (m, 4H), and 1.27-1.41 (m, 14H).

Compound **6**, N_3-TEG-C_{11}-SAc: Up to 500 mg of Compound **5** was dissolved in a minimal amount of DMSO. This was added to a solution of 1.1 eq sodium azide in dry DMSO that had been heated to 80˚C. This reaction was allowed to stir overnight under an atmosphere of N_2. The crude reaction mixture was diluted 5x with cold DI water, and the product was extracted 3x with hexanes and 3x with diethyl ether. These fractions were then combined and washed 3x with brine. Purification of this crude mixture was accomplished using a silica column and a mixture of hexanes and ethyl acetate as the mobile phase. The product was obtained in 59% yield. ^{1}H NMR (400 MHz, $CDCl_3$) δ 3.55-3.69 (m, 12H), 3.44 (t, 2H), 3.38 (t, 2H), 2.85 (t, 2H),

2.31 (s, 3H), 1.55 (m, 4H), and 1.22-1.38 (m, 14H).

Compound **7**, N_3-TEG-C_{11}-SH: 100 mg of Compound **6** in methanolic 0.1 M HCl was stirred under an inert atmosphere for 3 days. This was neutralized using cold 0.1 M NaOH, and the solvent was reduced to a minimal volume with rotary evaporation. The crude product was used immediately afterwards for place exchange.

Compound **8**, Ts-TEG: Up to 10 g of Compound **1** was dissolved in 30 mL of dry acetone. To this was added 1.1 eq of TsCl and 2 eq of TEA. The reaction proceeded with stirring for 6 hours under an atmosphere of N_2. The solid, white byproduct was removed with gravity filtration, and rotary evaporation was used to remove the solvent from the filtrate. A 67% yield of the oily product was obtained using a silica column and a mixture of hexanes and ethyl acetate as the mobile phase. ^{1}H NMR (400 MHz, $CDCl_3$) δ 7.80 (d, 2H), 7.34 (d, 2H), 4.17 (t, 2H), 3.70 (m, 4H), 3.65 (m, 4H), 3.60 (m, 6H), and 2.45 (s, 3H).

Compound **9**, AcS-TEG: Up to 3 g of Compound **8** was dissolved in dry acetonitrile. 1.2 eq of potassium thioacetate was also dissolved in dry acetonitrile and placed under an atmosphere of N_2. The solution of Compound **8** was added dropwise, and this reaction was allowed to stir overnight. After removal of the acetonitrile with rotary evaporation, the crude product was purified on a silica column. Two solvent systems were used with similar yields: methanol in dichloromethane and a mixture of ethyl acetate and hexanes. In each case, a pale yellow oil was obtained in approximately 84% yield. ^{1}H NMR (400 MHz, $CDCl_3$) δ 3.74 (t, 1H), 3.55-5.66 (m, 12H), 3.10 (t, 2H), and 2.34 (s, 3H).

Compound **10**, AcS-TEG-Ts: Up to 3 g of Compound **9** was dissolved in dry acetone. 1.1 eq of TsCl and 2 eq of TEA was added to this mixture, and the mixture was stirred for four hours under an atmosphere of N_2. The solid, white precipitate was removed with gravity

filtration, and the solvent was removed from the filtrate via rotary evaporation. The heterogeneous mixture was loaded onto a silica column and eluted with a mixture of ethyl acetate and hexanes. A pale yellow oil was obtained in an 81% yield. ^{1}H NMR (400 MHz, $CDCl_3$) δ 7.80 (d, 2H), 7.34 (d, 2H), 4.17 (t, 2H), 3.70 (t, 2H), 3.59 (t, 10H), 3.08 (t, 2H), 2.45, s, 3H), and 2.34 (s, 3H).

Compound **11**, AcS-TEG-N_3: Up to 500 mg of Compound **10** was dissolved in a minimal amount of DMSO. This was added to a solution of 1.1 eq of NaN_3 in dry DMSO warmed to 80˚C. This reaction was allowed to stir overnight under an atmosphere of N_2. The crude reaction mixture was diluted 5x with cold DI water, and the product was extracted 3x with hexanes and 3x with diethyl ether. These fractions were then combined and washed 3x with brine. Purification of this crude mixture was accomplished using a silica column and a mixture of hexanes and ethyl acetate as the mobile phase. A pale yellow oil was obtained in a 66% yield. ^{1}H NMR (400 MHz, $CDCl_3$) δ 3.65 (m 12H), 3.40 (t, 2H), 3.10 (t, 2H), and 2.34 (s, 3H).

Compound **12**, HS-TEG-N_3: 100 mg of Compound **11** in methanolic 0.1 M HCl was stirred at 40˚C under an inert atmosphere overnight. This was neutralized using cold 0.1 M NaOH, and the solvent was reduced to a minimal volume with rotary evaporation. The crude product was used immediately afterwards for place exchange.

Compound **13**, Ts-TEG-Ts: Two methods were used obtained this product. It exists in small amounts as a minor product in the synthesis of Compound **8**. The ditosylate was also synthesized in larger quantities by adding a large excess of TsCl. Up to 5 g of Compound **1** was added to 3 eq of TEA and 2.4 eq of TsCl in 50 mL of dry acetone. This was allowed to stir under an atmosphere of N_2 for six hours. The solid, white byproduct was removed through gravity filtration, and the solvent was removed from the filtrate using rotary evaporation. The resulting

heterogeneous mixture was loaded onto a silica column and eluted with a mixture of hexanes and ethyl acetate. A pale yellow oil was obtained in an 87% yield. ^{1}H NMR (400 MHz, $CDCl_3$) δ 7.75 (d, 4h), 7.30 (d, 4H), 4.10 (t, 4H), 3.63 (t, 4H), 3.51 (m, 8H), and 2.40 (s, 6H).

Compound **14**, N_3-TEG-N_3: Up to 250 mg of Compound 13 was added to a solution of 2.1 eq of NaN_3 in DMSO. This mixture was stirred at 80˚C overnight under an atmosphere of N_2. The crude reaction mixture was diluted 5x with cold DI water, and the product was extracted 3x with hexanes and 3x with diethyl ether. These fractions were combined and washed 3x with brine before being reduced to a minimal volume with rotary evaporation. Purification of this crude mixture was accomplished using a silica column and a mixture of hexanes and ethyl acetate as the mobile phase. ^{1}H NMR (400 MHz, $(CD_3)_2CO$) δ 3.69 (t, 4H), 3.63 (m, 8H), and 3.39 (t, 4H).

Nanoparticle Syntheses

Tiopronin protected gold nanoparticles were synthesized as described in Chapter II. Nanoparticles passivated by monolayers of MUTEG, MH, MBA, and MUA were prepared with modifications to these syntheses.

MUTEG-protected AuNPs were synthesized by dissolving 100 mg $HAuCl_4 \cdot 3H_2O$ in 50 mL of a 6:1 v/v mixture of methanol:glacial acetic acid. 3 eq of MUTEG was then added, and the first reduction step was allowed to proceed for three days with stirring. The second reduction step was completed by rapidly adding 10 eq of $NaBH_4$ in a minimal amount of cold DI water. Three hours later, the solvent was removed with rotary evaporation, and the AuNPs were resuspended in DI water. Dialysis was performed against DI water using 10 kDa MWCO SnakeSkin™ dialysis tubing. Dialysis water was changed twice daily until no free ligand was

observed in ^{1}H NMR spectra.

MBA-protected AuNPs were synthesized under basic conditions. 400 mg of MBA was first dissolved in 100 mL a 30:70 mixture of methanol:water whose pH was adjusted to 13 by the addition of concentrated NaOH. 300 mg of $HAuCl_4 \cdot 3H_2O$ was then dissolved in 10 mL of DI water and added to the solution of MBA. After the solution became colorless, 10 eq of $NaBH_4$ was rapidly added in a minimal amount of DI water. This was stirred overnight prior to the solvent being removed with rotary evaporation. The AuNPs were resuspended in and dialyzed against DI water using 10 kDa MWCO SnakeSkin™ dialysis tubing. Dialysis water was changed twice daily until no free ligand was observed in ^{1}H NMR spectra.

MUA-protected AuNPs were synthesized by first dissolving 300 mg of $HAuCl_4 \cdot 3H_2O$ in 25 mL of methanol. 3 eq of MUA was dissolved in a separate 25 mL portion of methanol, and the two solutions were mixed. After the solution became colorless, a solution of 10 eq $NaBH_4$ in a minimal amount of cold DI water was rapidly added. This solution was stirred overnight before the solvent was removed with rotary evaporation. AuNPs were resuspended in and dialyzed against DI water using 10 kDa MWCO SnakeSkin™ dialysis tubing. Dialysis water was changed twice daily until no free ligand was observed in ^{1}H NMR spectra.

MH-protected AuNPs and C_6-protected AuNPs were synthesized using the Brust phase transfer method. 100 mg of $HAuCl_4 \cdot 3H_2O$ was dissolved in 10 mL of DI water. 30 mL of a 1.0 M solution of tetraoctylammonium bromide in toluene was added, and the mixture was stirred until the gold was completely transferred into the organic layer. The organic layer was then separated, and to this was added 3 eq of the desired thiol, either C_6 or MH. This reduction step was allowed to proceed until the solution became pale yellow prior to the addition of 10 eq of $NaBH_4$ freshly dissolved in a minimal amount of cold DI water. After three hours, the solvent

was removed via rotary evaporation, and particles were cleaned through successive rounds of centrifugation and resuspension in ethanol, acetone, and hexanes.

Place Exchanges

A series of place exchanges reactions were attempted to expand the number of experimentally derived ligand combinations that lead to JNP formation. AuNPs protected by a single ligand type were first dissolved in water with the exception of C_6 particles in hexanes. To this was added an aqueous solution of the secondary ligand type, again with the exception of the ligand to be exchanged onto the AuNPs passivated by C_6. Enough of the secondary ligand was added to afford at least a 1:1 mixture on the surface of the particle assuming complete exchange onto the particle. This value was calculated based on data obtained from TGA. When the ligand was not completely soluble in water, methanol, acetone, and ethyl acetate were titrated in until the solution became colorless.

Nanoparticle Characterization

All nanoparticles were characterized with ^{1}H NMR after synthesis to ensure the removal of excess free ligand. For those which underwent place exchange with ligands of a second type, they were characterized following the secondary purification step. C_6/PEPEPSH-protected AuNPs and Tio/MUTEG-protected AuNPs were also analyzed with NOESY to evaluate through space interactions of their hydrogen atoms near the surface of the particle.

All monolayer protected AuNPs were analyzed with TGA as described in Chapter II. This allowed the percentage of organic ligands to be determined which was used to formulate place exchange protocols.

MALDI-IM-MS was used to evaluate the nanoscale patterning of the ligands on the surface of mixed monolayer AuNPs. AuNP samples were spotted onto a stainless steel plate via the sandwich method using concentrated α-cyano-4-hydroxycinnamic acid in acetonitrile and 0.1% trifluoroacetic acid. Analysis was performed on a Waters G2 Synapt as previously described, and data processing occurred on MassLynx software.[126]

Results & Discussion

NOESY spectra for AuNPs passivated by mixed monolayers of C_6/PEPEPSH and Tio/MUTEG are shown in Figure 4.5 and Figure 4.6, respectively. As shown in Chapter II, the attachment of the ligands to the surface of the AuNPs results in their ^{1}H NMR signal being significantly broadened relative to that of the free ligand. The main contributing factor to this is likely a lack of symmetry leading to a large number of chemical environments for ligands bound to the inorganic core.[144] Fortunately for mixed monolayers of C_6/PEPEPSH, a large difference exists between the chemical shifts arising from alkyl and aromatic protons. This difference allows the signal arising from each type of ligand to be differentiated, even once attached to AuNPs. Therefore, the crosspeaks in NOESY spectra can also be attributed to through-space interactions between specific ligand types. Figure 4.5 exhibits crosspeaks between the C_6 and PEPEPSH ligands, suggesting that the two ligand types do not self-assemble into distinct hemispheres but undergo significant mixing, increasing the number of interfacial sites and thus through-space interactions between their protons. The same cannot be said for the mixed monolayers of Tio/MUTEG. The similarity of the chemical shifts arising from protons of each of these ligand types convolutes the NOESY spectrum seen in Figure 4.6. The observed relaxational crosspeaks could result from interactions between ligands of the same type or from

Tio/MUTEG interactions.

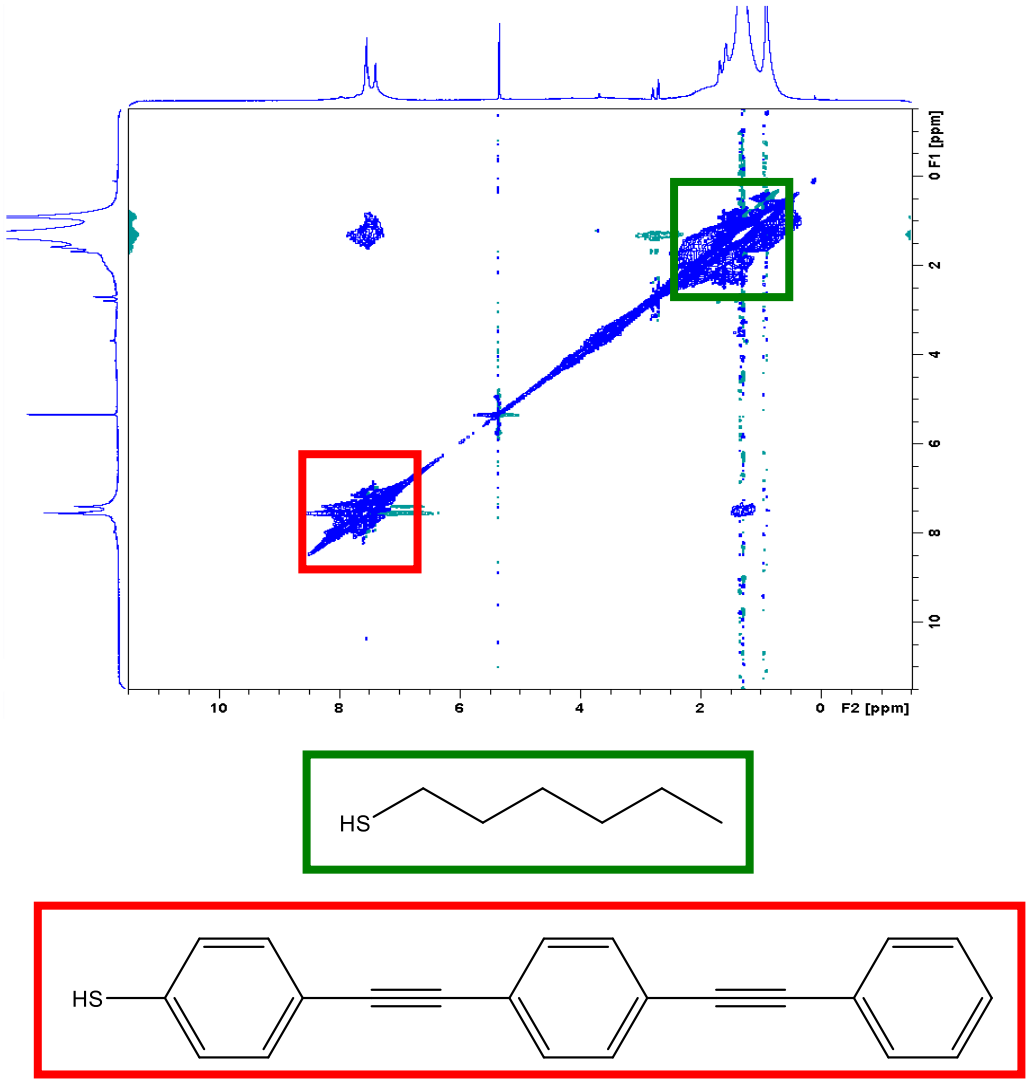

Figure 4.5: NOESY spectrum of AuNPs passivated by a mixed monolayer of C_6 (green) and PEPEPSH (red). Separation of the chemical shifts for the two ligands allows crosspeaks to be attributed to through-space interactions between the different ligand types.

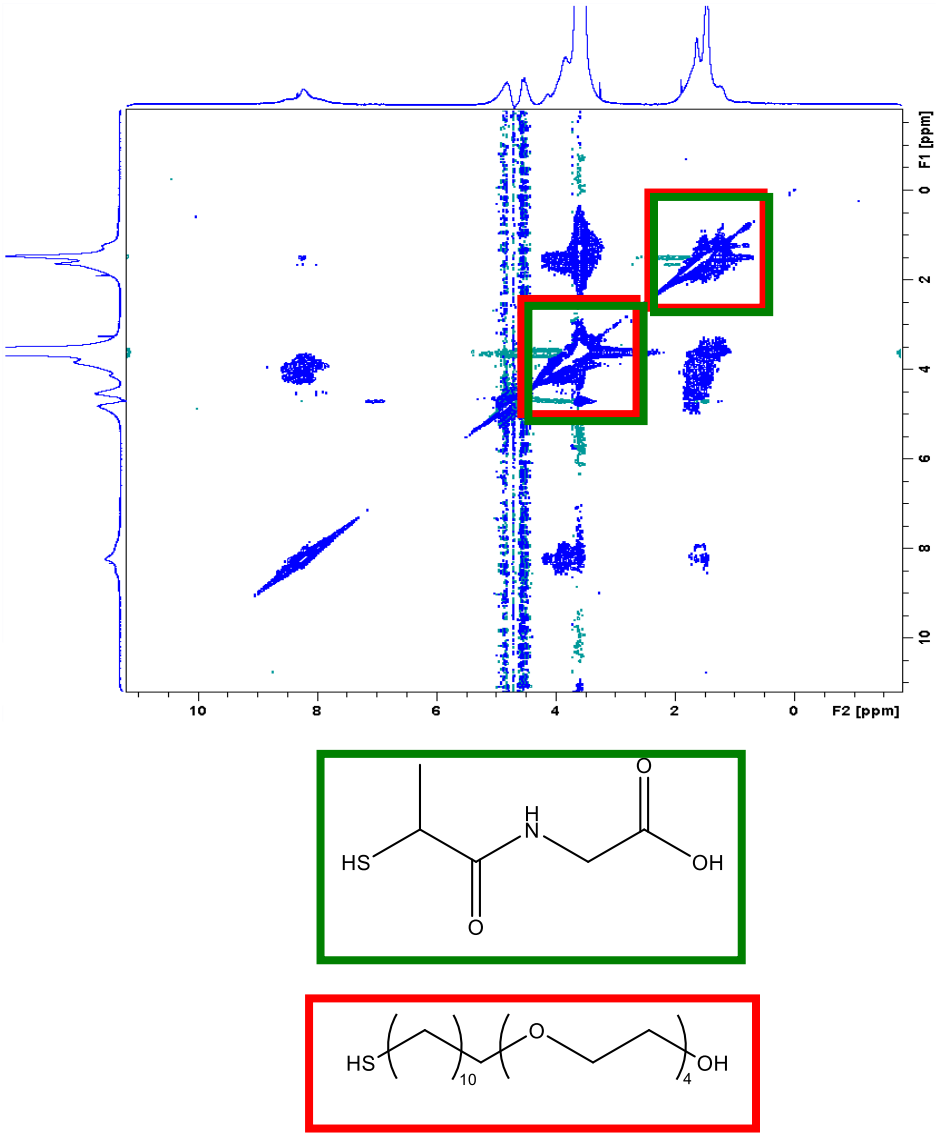

Figure 4.6: NOESY spectrum of AuNPs passivated by mixed monolayers of Tio (green) and MUTEG (red). Overlap of the chemical shifts for protons of the two ligand types convolutes the 2D spectrum, making it impossible to determine if crosspeaks arise due to through-space homo- or hetero-ligand interactions.

The convolution of NMR peaks for many water soluble ligands led to the use of MALDI-IM-MS as an alternative to determine the patterning of ligands on the surface of the AuNPs.

Shown in Figure 4.7 are the 3D ion mobility mass spectra of AuNPs passivated by mixed

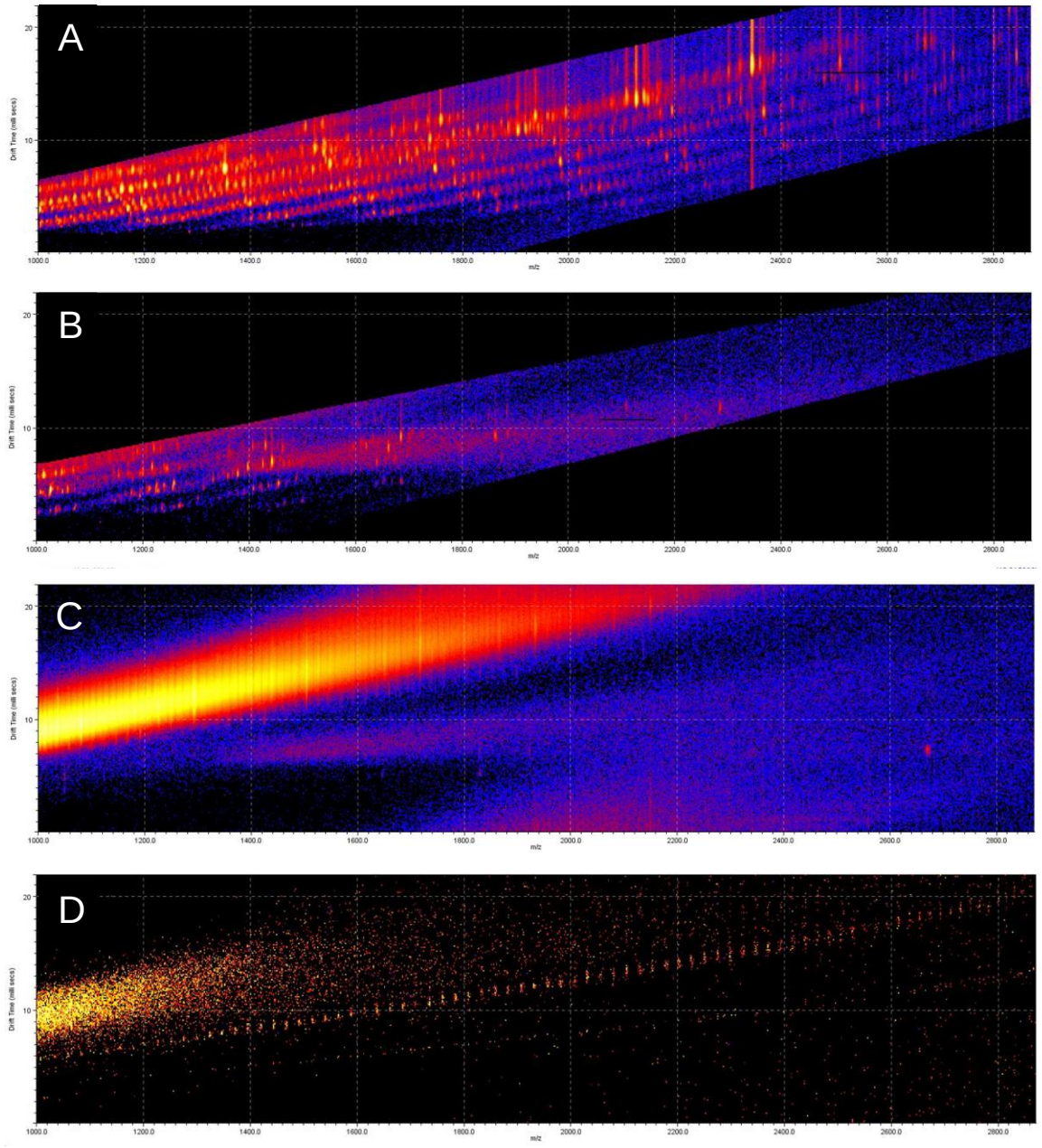

Figure 4.7: MALDI-IM-MS spectra of AuNPs passivated by mixed monolayers of (A) Tio/MUTEG, (B) MUA/MBA, (C) Tio/MBA, and (D) Tio/MUA.

monolayers of Tio/MUTEG, MUA/MBA, Tio/MBA, and Tio/MUA. Spectra of Tio/MUTEG AuNPs were similar to those seen in previous experiments with distinct bands corresponding to

specific numbers of gold atoms per cluster.[126] Plotting the intensities of the $Au_4L_xL'_{4-x}$ species against a binomial distribution model, as seen in Figure 4.8 confirmed the Janus separation of the ligands on the surface of the AuNPs. The other mixed monolayers, however, did not produce such interpretable spectra. While MUA/MBA AuNPs did yield spectra with distinct bands of $Au_4L_xL'_{4-x}$ species, signals were consistently of very low intensity. Tio/MBA AuNPs suffered from even greater problems as the signals were obscured by the matrix, and Tio/MUA AuNPs failed to ionize, instead appearing to react with the matrix during spotting of the MALDI plate.

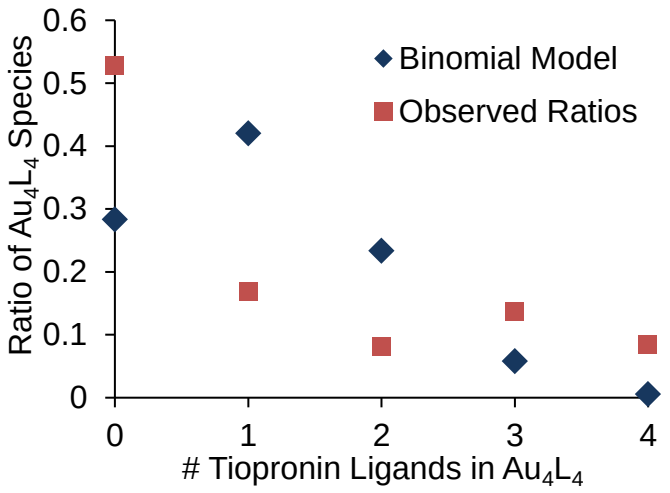

Figure 4.8: Comparison of experimental MALDI-IM-MS data of Tio/MUTEG to a binomial distribution model. The calculated RSS value can then be used to determine the extent of phase separation of the ligands on the surface of the AuNPs.

These ligand combinations were chosen in part due to the water solubility of AuNPs protected by monolayers of the individual ligands. Failure of these combinations to produce new data concerning the phase separation of ligands on the surface of AuNPs was unfortunate, but they likely did not represent a step toward orthogonal functionalization of faces of a JNP as they each were terminated by carboxylates. To this end, four other combinations of mixed monolayers predicted to yield water soluble AuNPs were also investigated: Tio/**7**, Tio/**12**, MH/**7**, MH/**12**.

Place exchange onto Tio and MH AuNPs of the azide-terminated thiols (**7** and **12**) resulted in AuNPs with interesting interfacial properties. To remove excess **7** and **12** after place exchange onto Tio AuNPs, extractions using organic solvents were performed. When organic solvents immiscible with water, such as ethyl acetate, were used, the mixed monolayer AuNPs did not suspend well in solution but instead remained at the liquid-liquid interface. Agitation of the interface in the form of shaking the mixture in a separatory funnel resulted in the production of large numbers of semi-stable droplets. The AuNPs appeared to aggregate and function as a membrane, with droplets slowly aggregating and giving rise to larger, more stable droplets. Attempts to further purify the carboxylate/azide-functionalized AuNPs failed, but the interface-stabilizing properties of the AuNPs suggests that Janus separation is occurring. Place exchanged MH particles revealed similar properties, but the AuNPs had less of a tendency to stabilize the interface, instead aggregating and precipitating out of aqueous solutions. This behavior may be due to the intercalation of the PEG region of the **7** and **12** into the alkyl region of MH.

Although new combinations of self-assembling ligands for nanoscale Janus patterning were unable to be confirmed through NOESY or MALDI-IM-MS, Tio/**7** and Tio/**12** mixed monolayers show promise. Further work will be required to purify the AuNPs after place exchange, or applications may be identified where their interfacial stabilization behavior is sufficient to warrant further investigations without purification. However, purification and further characterization cannot be overlooked if the AuNPs are to be used in biological applications. Amphiphilic molecules such as the Tio/**7** and Tio/**12** mixed AuNPs have the potential to interact with cell membranes in a manner similar to that of surfactants. By tailoring the surface of the AuNPs, it may become possible to passively deliver cargo into the cell using Janus particles with amphiphilic character.

Previous studies have demonstrated unexpected effects of altering the solution-exposed termini of one ligand type in a mixed monolayer,[124] and the results of the experiments described above confirm the need to carefully optimize ligand combinations. As the computational power of *in silico* methods grows, more JNP-inducing combinations are likely to be identified. Experimental methods relying on self-assembly to create these particles and subsequent characterization steps, however, may continue to be plagued by purification obstacles if the two ligands exhibit significantly different solubilities. As a result, future experiments should take care to choose ligands with similar solubility but with functional groups capable of undergoing orthogonal modification.

Chapter V

CONCLUSIONS AND FUTURE PERSPECTIVES

Preventive Nanoparticles

Biomimetic gold nanoparticles were demonstrated in Chapter III to elicit a humoral immune response *in vivo*. However, the presence of antibodies against a pathogenic protein does not necessarily confer protective immunity. To determine whether or not protection is afforded, additional studies are required that would require challenging inoculated and control mice with live spores of *B. anthracis*. Such investigations would allow for optimal inoculation schedules and dosages to be determined to maximize antibody titers. Perhaps most significantly, the prognosis of mice challenged after inoculation with biomimetic AuNPs vs BioThrax, the FDA-approved vaccine against anthrax, will reveal the true benefits, if any, of the shift to synthetic inoculants over less-defined bacterial filtrates.

Prior to additional animal studies, *in vitro* studies should first be undertaken to better understand the mechanism by which the AuNPs are acting as vaccines. Such *in vitro* studies would be designed to evaluate the activation of MHC I vs MHC II pathways as well as probe the extent of antigen processing. By identifying the sequence(s) presented from the MHCs, differences may be observed between the linear and looped peptide samples. One hypothesis suggests that the looped structure protects the peptides from degradation for a longer period of time, allowing for more complete sequences to be presented from MHCs. This would explain the stronger correlation between antibody production and the looped peptide vs the linear analogue.

A limitation of preventive medicine in the form of vaccination is the time required for

antibody production after inoculation. After a known or suspected exposure to a pathogen, vaccination may be less effective depending on the amount of time that has passed between exposure and inoculation. Post-exposure prophylaxis treatments for infectious agents for which no vaccine currently exists rely on other strategies that eliminate the need for internalization, processing, and presentation of antigens. For example, a cocktail of small molecule inhibitors is recommended within 72 hrs of a known exposure to HIV. These antiretrovirals are highly effective when used properly but still fail to prevent infection in some cases.[145]

Five classes of drugs are used to slow the progression of HIV infection into AIDS (entry inhibitors, fusion inhibitors, reverse transcriptase inhibitors [nucleoside and non-nucleoside], integrase inhibitors, and protease inhibitors), and most post-exposure prophylaxis regimens are combinations of at least two of these classes.[145,146] The goal of entry and fusion inhibitors is to prevent HIV infection by thwarting the entrance of viral RNA. The first step in an HIV virion infecting a host cell is mediated by interactions between gp120 (an envelope protein decorating the surface of the HIV virion) and CD4 (a host surface receptor). In 1998, the co-crystal structure of gp120 and CD4 was solved, revealing which residues make close contact,[147] and broadly neutralizing antibodies against HIV-1 have been shown to bind to or obscure the CD4 binding site of gp120.[148]

CD4 is an integral component of the immune system. Any drugs that interfere with its native functioning could result in CD4+ cell toxicity, and conflicting reports exist as to the safety of these compounds.[149] An alternative to binding CD4 is to develop a molecule to block gp120. Upon binding to CD4, gp120 undergoes conformational changes allowing it to bind to a surface bound chemokine coreceptor.[148,150] This then allows a second protein, gp41, to penetrate the host cell membrane and cause fusion of the host and viral membranes, resulting in delivery of the

viral capsid. After the co-crystal structure of revealed which residues make close contact, studies began that determined which of those residues were essential for protein interactions.[147] This information was utilized to create short, peptide mimics of CD4 to determine their relative ability to bind to gp120. Cyclic and linear peptide sequences were explored, with cyclic peptides exhibiting the highest levels of activity.[84] In another study, Feldheim demonstrated that for small molecule antagonists of CCR5, a co-receptor bound by gp120 to anchor the virus to the cell surface, the multivalent property that arises by conjugating them to the surface of small AuNPs blocked virion-host cell fusion whereas the unbound ligand had no effect.[151] This was the first reported instance of AuNPs being used as entry/fusion inhibitors and suggests that even low affinity small molecules or peptides could have therapeutic potential if used on a scaffold that allows for multivalent presentation.

As Tio AuNPs with modified monolayers have been demonstrated to be biocompatible[19] and interact with components of the immune system,[152] rationally designed nanostructures may allow us to prevent the first interaction of HIV with surface receptors necessary for infection. By attaching CD4-mimetic peptides having previously been shown to bind with high affinity to gp120[84] to the surface of biocompatible TioAuNPs,[153] infection of host cells may be prevented by blocking the CD4 binding site of HIV. Such studies would be accomplished through the synthesis and characterization of a library of CD4-mimetic AuNPs and subsequent affinity determination toward gp120 through the use of biolayer interferometry (BLI) as well as a quartz crystal microbalance (QCM). Undesirable effects, notably the activation of the envelope spike, must also be selected against through QCM experiments utilizing anti-gp41 antibodies (Abs) after pretreatment with CD4-mimetic AuNPs.

CD4-mimicking sequences have previously been shown to have a high affinity for gp120

with the more complete, structurally similar, and conformationally constrained sequences exhibiting the greatest binding.[84] With increased structural similarity, however, comes the potential for the CD4-mimetic AuNPs to inadvertently elicit conformational changes in the envelope spike needed for membrane fusion. By screening nanoconjugates presenting the seven sequences identified in Figure 5.1, AuNPs may be identified that not only exhibit high binding affinities to viral proteins but that also fail to induce undesirable conformational changes in the target.

C-PEG-IQFHWKNSNQIKILGNQGSFLTKGPSKLNDRADSRRSLW
C-PEG-IQFHWKNSNQIKILGNQGSFLTKGPSKLNDRADSRRSLW-PEG-C
C-PEG-IQFHWKNSNQIKILGNQGSALTKGPSKLNDRADSRASLW-PEG-C
C-PEG-IKILGNQGSFLTKGP
C-PEG-IKILGNQGSFLTKGP-PEG-C
C-PEG-IKILGNQGSALTKGP-PEG-C
C-PEG-IKILGNQGSfLTKGP-PEG-C

Figure 5.1: Sequences 1-3 represent the CD4 binding site. Sequences 4-7 are those that correspond to a CDR2-like loop. In yellow are residues to tether and present the sequence away from the surface of the AuNP. Red represents hotspot positions.

The synthesis and characterization of the bioconjugates would proceed as described in previous chapters prior to *in vitro* screening using BLI and QCM. Using BLI, recombinant gp120 will be biotinylated and bound to the streptavidin-coated tips. Solutions of the various peptide-conjugated AuNPs will then be evaluated for binding. Biotinylated hemagglutinin and bare TioAuNPs will be used as controls against non-specific adsorption of particles to the tips of the optical fiber. In a QCM, the biotinylated gp120 will be anchored to a streptavidin-functionalized gold electrode atop an oscillating quartz crystal. This technique has been used previously in the analysis of biomolecule binding to gold nanoparticles[111,154] and may avoid interference and artifacts that could arise in BLI due to the scattering and absorption of light by AuNPs.

For CD4-mimetic AuNPs to act as standalone entry inhibitors, it will be imperative that their binding not elicit the conformational changes in the envelope spike that allow it to fuse the host and viral membranes. AuNPs that are exceptional CD4 mimics may display high binding affinities but also induce these undesirable conformational changes. BLI and QCM experiments (Figure 5.2) using whole HIV virions rather than recombinant gp120 alone may allow us to decouple AuNP binding affinity and the induction of counterproductive conformational changes within the target protein. Previous studies[155,156] have demonstrated the specificity of the monoclonal Abs 2F5 and 4E10 for gp41 epitopes that are obscured from binding in the unactivated conformation of the envelope spike, so the affinity of these antibodies for the viral particles after pretreatment with our AuNPs will provide key information about the ability of our CD4-mimetic AuNPs to initiate the conformational cascade that results in the exposure of buried gp41 residues. If correlations can be made between protein binding and viral entry data, the first step in future HIV entry inhibitor studies could use recombinant envelope proteins rather than whole or live viruses, decreasing some of the risks and difficulties currently associated with the development of HIV treatments.

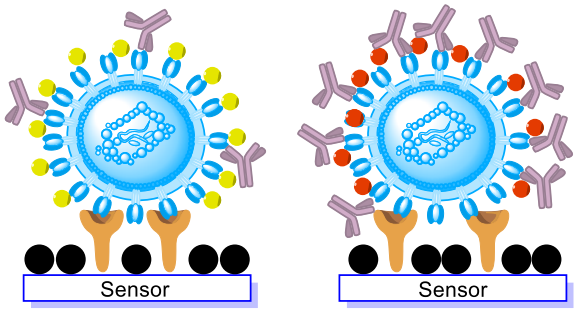

Figure 5.2: Schematic of QCM experiments utilizing AuNPs that fail to (left) and do (right) elicit sufficient conformational changes to gp120 such that gp41 is exposed. Black=surface blocking agent; tan=immobilization protein; blue=HIV virion; gold=gp120-mimetic AuNPs that fail to induce conformational changes; red=gp120-mimetic AuNPs that allow gp41 to become exposed; purple=anti-gp41 Abs.

Data on the binding of AuNPs presenting antagonists to HIV proteins such as gp120 should be easily attained, and the results will likely align well with those in the original study with the gp120-binding peptides.[84] Peptides with more complete sequences are expected to bind more tightly to the immobilized gp120, and sequences with mutated hotspot residues should lose most of their binding capabilities. Also, the reduction of conformational states by the bidentate binding of the dithiols will likely promote binding to the gp120 as suggested by the results in Chapter II. Retaining their stability for longer periods of time and under harsher conditions compared to Abs, AuNPs demonstrating high affinity for gp120 could subsequently be employed in low resource diagnostics.

Diagnostic Nanoparticles

X-ray based computed tomography (CT) is one of the most common medical imaging techniques. These non-invasive scans are used to determine the size, shape, and location of tumors which in turn aid physicians in the staging and treatment of cancer. Without the use of contrast agents, however, CT can be plagued by poor resolution.[157] The AuNPs described in Chapter II could give rise to targeted contrast agents. Modern contrast agents are no longer characterized by high toxicity and poor solubility,[157] and AuNPs would not sacrifice these properties for enhanced local contrast.

Lower energy radiation could also be used to visualize cells of interest. Small AuNPs have been shown to have fluorescence in the NIR, and this fluorescence can be enhanced through a process known as etching (Figure 5.3). Tio AuNPs are dissolved in an aqueous solution of free tiopronin to give a ratio of 100:1 free to bound ligand. This solution is held at 40˚C and stirred continuously for 3 days prior to dialysis against DI water. Conjugating targeting peptides to these

particles would allow *in vitro* and *in vivo* imaging of regions of interest by taking advantage of the fluorescence of the AuNPs being in the NIR window.

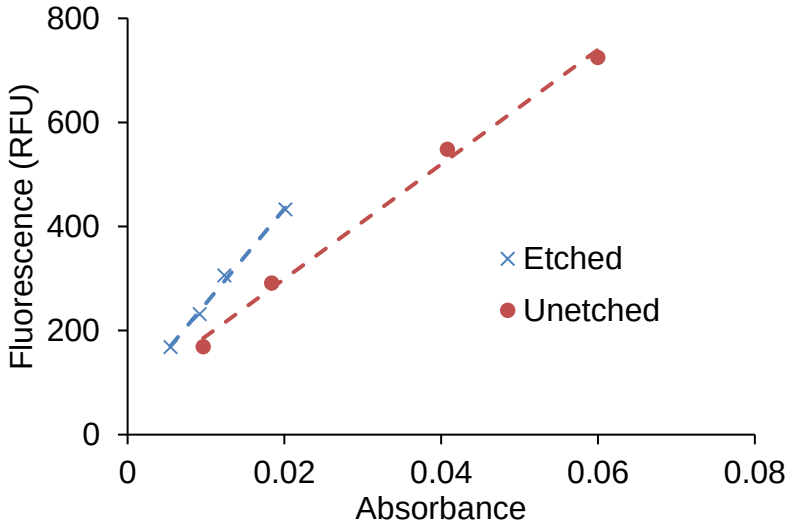

Figure 5.3: Comparison of the quantum yield of etched vs unetched Tio AuNPs.

Therapeutic Nanoparticles

The AuNPs described in Chapter II were demonstrated to enhance the effects of radiotherapy. Radioenhancement was limited to cells of interest, specifically those overexpressing $\alpha_v\beta_3$ integrin, by conjugating targeting peptides to the inorganic core. Each of the targeted AuNPs evaluated *in vitro* performed at least as well as the control Cilengitide which made it to Phase III clinical trials, suggesting that future work should be continued with these bio/nanoconjugates. The next step will be to identify any radioenhancement observed in murine models bearing tumorigenic xenographs. Previous studies injected untargeted AuNPs into mice and noted decreased tumor volume and increased survival (Figure 5.4).[70] By adding a molecular

recognition element to bind overexpressed membrane-bound proteins, the outcomes are expected to improve even further.

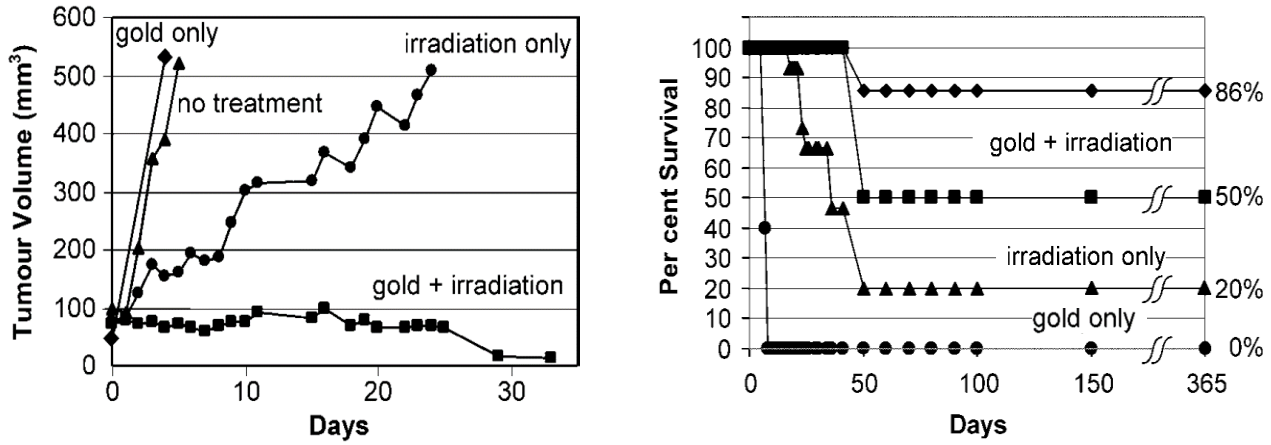

Figure 5.4: Tumor volume (left) and survival curve (right) of mice bearing xenographic tumors. Mice were held as controls or treated with radiation, AuNPs, or a combination of radiation and AuNPs. Mice treated with combinations of radiation and AuNPs exhibit decreased tumor volumes and increased survival rates relative to controls and treatments of radiation or AuNPs alone.[70]

Another avenue of future research is to investigate the mechanism by which the AuNPs are enhancing the effects of radiation. If the interaction of incident radiation with the AuNPs results in electrons being ejected to create reactive oxygen or nitrogen species, the addition of radical inhibitors would reduce the observed radioenhancement. Alternatively, if photothermal effects are the dominant factor, radical inhibitors would have no effect on the DEFs. Biochemical assays could also be undertaken to determine whether integrin mediated death is occurring as a result of the targeted AuNPs acting as integrin antagonists.

As the ionizing radiation used to treat many cancers often leads to undesirable collateral damage, nanostructures with the ability to absorb light from non-ionizing portions of the EM spectrum present alternatives with less collateral damage. Because AuNRs exhibit a plasmon

resonance band in the NIR region, they could potentially be employed for deep photothermal therapy.[158] To breach the lower limit of known AuNR synthesis, AuNPs can be used instead and dimerized to form structures with tunable electronic properties mimicking those of similarly sized AuNRs. As the distance between two gold nanostructures becomes small, their plasmons begin to interact until the longitudinal plasmon that emerges is indistinguishable from that of AuNRs (Figure 5.5).[159] The extent to which the plasmons of separate AuNPs interact is dictated by the distance between them, and the symmetric azide-terminated PEGs synthesized in Chapter IV could be used to easily bridge JNPs presenting alkynes from one face. By varying the length of the PEG linker, the distance between the two particles can be tuned to yield a longitudinal plasmon band in the NIR region.

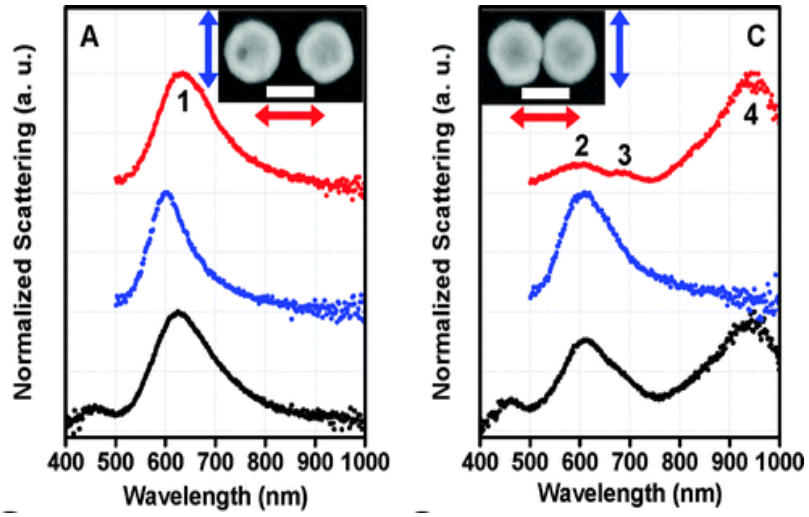

Figure 5.5: Spectra of spatially and electronically separate gold nanoshells (left) and gold nanoshells brought close to one another (right). As the distance between them becomes small, their plasmons interact to form a longitudinal plasmon characteristic of AuNRs.[159]

Appendix A

VALIDATION OF A ROTARY PLANAR VALVE AND ROTARY PLANAR PERISTALTIC MICROPUMP AS A MICROFORMULATOR

Introduction

The continued development of organs-on-chips (OoCs) is expected to revolutionize the fields of toxicology, drug discovery, and personalized medicine.[160] These emerging microanalytical platforms bridge the divide between traditional *in vitro* techniques that fail to reproduce human physiological microenvironments and *in vivo* methods such as clinical trials that are orders of magnitude more expensive.[161] By improving upon the predictive power of existing model systems, one goal of using OoCs is to reduce the number of false hits in the drug discovery pipeline. This will allow researchers to reduce the number of experimental animals required for preclinical trials, mitigating both financial and ethical concerns. Additionally, the shift to human-derived preclinical models will allow species-specific predictions to be made which have been shown to be important, especially in toxicology.[162] Despite these advantages, however, OoCs face unique challenges related to the handling and manipulation of the requisite small volumes of media.[160,161,163]

Accurately reproducing *in vivo* conditions necessitates continuous perfusion within OoCs.[160] While the small volumes and low flow rates are beneficial in keeping material and spatial costs down, there remains a need for instrumentation capable of efficiently formulating and dispensing the media.[163] Widely used syringe pumps are relatively low cost, commercially available, and have applications in clinical settings, but they are limited in their ability to alter the formulation of the perfusion media over the course of an experiment. Due to the natural

oscillations that exist within the human body, static media conditions fail to reproduce the range of concentrations of biomolecules that are experienced over the course of a typical 24 hour period.[164] This inability to alter the perfusion media also restricts the ability of researchers to observe cellular responses to chemical perturbations.

To address this need, several strategies have been employed to create user-defined gradients and mixtures at the microliter scale.[165,166] Computer-controlled arrays of syringe pumps can be used to alter formulations of media over time by incorporating downstream mixers.[167] Other groups have proposed using a single device to control the exquisite balance of hormones inside of milli- or microhumans.[163] Such a device also allows for programmable perturbations of OoCs that require no disassembly of device components, facilitating their ease of use and reducing the risk of contamination or introduction of air bubbles. This approach has been used previously to identify cellular responses to dynamic stimuli with varying frequency.[168] Despite these advances, device cost and the number of components that can be incorporated into media formulations remain concerns.[165,166] This appendix describes the validation of a new microformulator that addresses these shortcomings. It is composed of a rotary planar peristaltic micropump (RPPM) and a normally closed rotary planar valve (RPV)[169] and has the ability to dispense user-defined mixtures of arbitrary complexity using 5 stock solutions.

Materials & Methods

The microformulators are composed of a rotary planar peristaltic micropump and a rotary planar valve. The fluidics for both of these devices are PDMS-based, and they are connected by Tygon tubing. The valve positions are normally closed[169] but can be opened by user-defined in custom AMPERE software. A valve position is opened by the rotation of a drivehead with a

groove. When the groove is over the valve to be opened, the tension that is keeping the valve channel closed is relieved by the upward motion of the ball bearing into the groove. A common output is shared among the five valve ports which feeds into the downstream pump (Figure A.1) whose negative pressure draws out the valve effluent. Both components of the device are controlled by a custom controller seen in the right of Figure A.1C. To ensure sterility of solutions when media formulations are present, septa-sealed vials are used along with needles featuring syringe filters as vents.

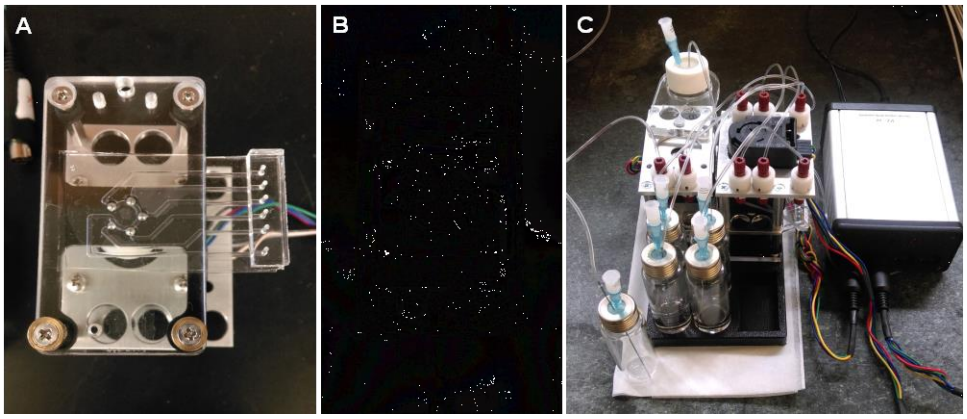

Figure A.1: Components of the microformulator: A) rotary planar valve (from below), B) rotary planar peristaltic micropump (from below), and C) fully assembled microformulator with controller.

To assess the performance of the valves, concentrated standards (High-Purity Standards) of silver, barium, yttrium, and cadmium were diluted for use. These concentrated metal solutions were combined with appropriate amounts of Optima grade nitric acid (Fisher) and 18.2 MΩ deionized water to make individual solutions of 20 ppm metal in 4% w/v nitric acid and an additional 100 ppm Ba in 4% w/v nitric acid solution. A metal-free solution of 4% w/v aqueous nitric acid was also created.

After first priming the fluidics with deionized water, the metal-free solution of nitric acid was used to prime the fluidics for 12 hours. To determine the extent of any leakage from the channels when in the closed position, channels 1-4 were filled with the 100 ppm Ba sample, and the pump and valve fluidics were then flushed for 30 min with the metal-free nitric acid solution coming from channel 5 at a pump speed of -20rpm. Immediately following the 30 minute flush and without stopping the pump or switching the open channel, three consecutive samples of 3 mL of output were collected from each device. These samples were analyzed for Ba content through ICP-OES on an Optima 7000 DV (Perkin Elmer). The spectral line used for quantitation was 455.403 nm.

To determine if the output could be standardized for each channel by performing a mass/time calibration, an experiment was performed in which each channel was opened for 45 s, followed by 300 s of the metal-free solution to collect the sample. Channels 1-4 were each filled with one of the 20 ppm metal standards, and channel 5 continued to dispense the metal-free solution. Pump speed was maintained at -20 rpm with the exception of 2 s stop-flow periods during which the position of the valve was changed. Five samples were taken from each device. 1 mL of each of the samples was added to 9 mL of 4% w/v aqueous nitric acid for analysis through ICP-OES. Spectral lines used for quantitation were 371.029 nm, 233.527 nm, 214.440 nm, and 328.068 nm for Y, Ba, Cd, and Ag, respectively. Immediately following the collection of the five samples of output, channel-specific mass/time calibrations were performed. This was accomplished by measuring the mass of the output at several time points when each of the channels was in the open position. An additional calibration was conducted for a single channel to identify the relationship between pump speed and stroke volume by holding the same channel open but changing the pump speed and measuring the mass at different time points.

A successful microformulator would not only allow for the output of the channels to be mixed in equal ratios, but it would allow for customized output along a spectrum of ratios. To verify that our devices possess this capability, mixtures were created by varying the amount of time that each channel was left open using the same protocol as that used for the equal-time experiment above.

Results & Discussion

As a percentage of total output, a low but statistically significant amount of leakage occurs from the closed channels (Figure A.2). Approximately 0.005% of the output was from those channels as determined by total Ba content. Such a small amount could conceivably arise not only from channels leaking but also from the slow desorption of residual barium from the walls of the fluidics and tubing over time.

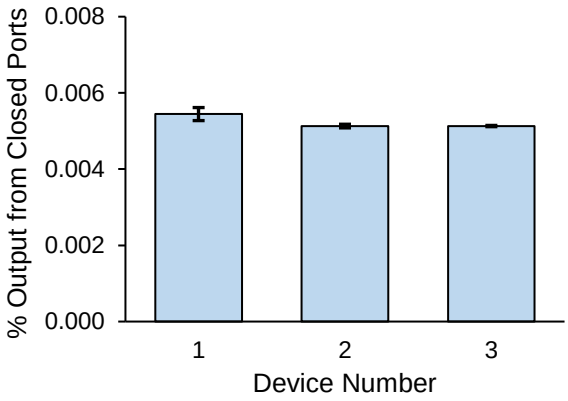

Figure A.2: Results from valve leakage test. A channel with 4% $HNO_{3(aq)}$ was held open while the other four channels held a concentrated Ba standard in 4% $HNO_{3(aq)}$. ICP-OES was performed on an Optima 7000 DV to determine Ba concentration in the output. Three separate microformulators were tested, and three sequential samples were taken from each. Error bars represent ± SD from the mean.

Data from the equal time experiment is presented as w/w ratios of the elements present in the output, and no significant difference exists between the ratios of the metals in the output and the ideal ratio of 1 (Figure A.3).

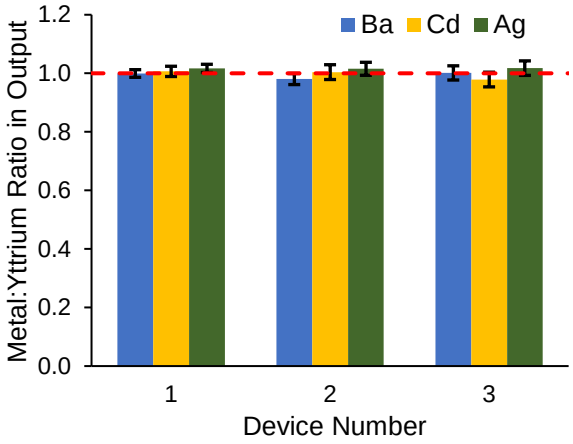

Figure A.3: ICP-OES results on equal-time formulations. One channel dispensed 4% $HNO_{3(aq)}$ while the other four channels dispensed a dilute metal standard in 4% $HNO_{3(aq)}$. ICP-OES was performed on an Optima 7000 DV. Three separate microformulators were tested, and error bars represent ± SD from the mean (n=5).

This lack of difference ($p > 0.05$) was observed after a correction was used to compensate for the unequal flow rates from the different channels. This required the flow rate from each channel to be determined (Figure A.4), and corrections were performed by multiplying by the reciprocal of the ratio of the slopes for the channels being compared (Equation A.1) to obtain the data in Figure A.3.

$$y = \frac{\text{Concentration Metal (ppm)}}{\text{Concentration Y (ppm)}} * \frac{\text{Flow Rate Y Channel}}{\text{Flow Rate Metal Channel}} \qquad \textbf{(Equation A.1)}$$

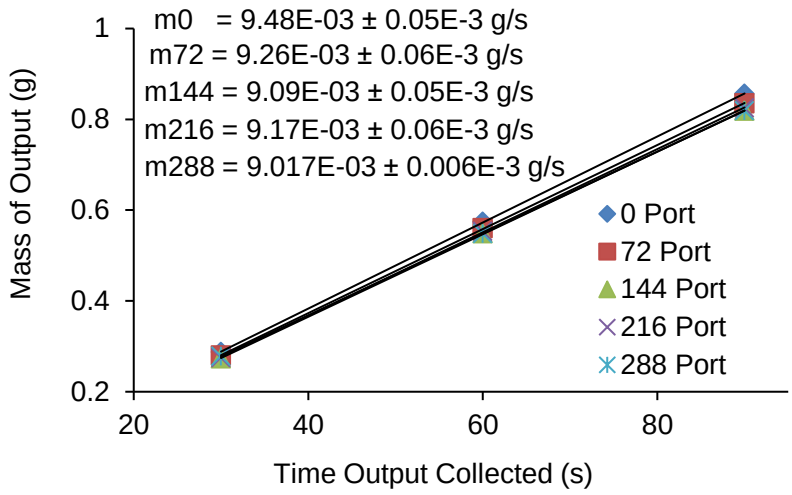

Figure A.4: Flow rates for each of the channels in the five port valves. This correction was necessary to standardize the outputs when each valve was opened for the same amount of time.

Two avenues were explored for the predictable mixing of metals from different ports: altering the pump speed and channel-open time. The data suggests that pump speed is an undesirable variable to change due to the many calibrations that would be required in order to accurately predict and dispense a desired amount of metal from each port. This is likely due to the PDMS fluidics requiring a non-zero relaxation time after being compressed by the pump, giving rise to non-uniform stroke volumes at different pump speeds (Figure A.5). The impact of this physical limitation can be eliminated, however, by instead introducing a variable upstream at the valve. By altering the time that each channel is left opened in the valve, predictable and user-defined ratios are possible.

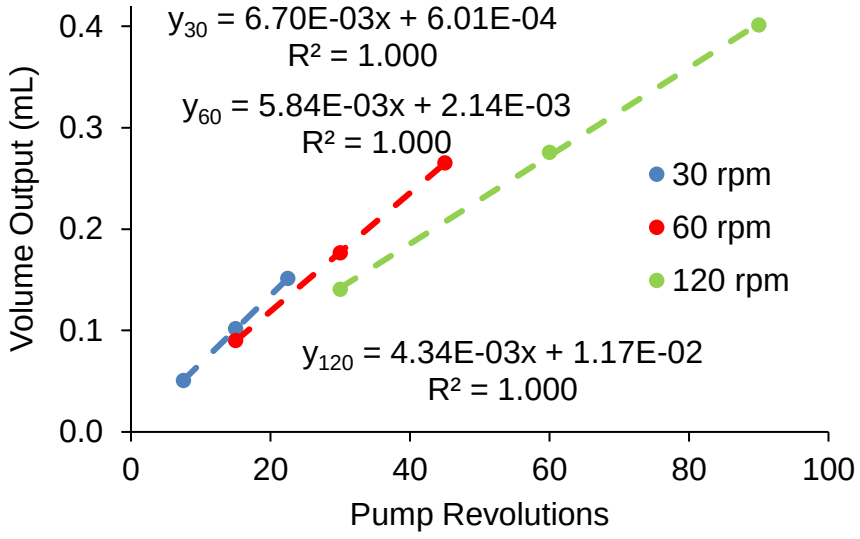

Figure A.5: Stroke volumes at varying pump speeds. Non-uniform stroke volumes emerge as the pump speed is varied, demonstrated by the change in slope.

The results of the time-division multiplexing experiments are shown in Figure A.6. As above, the data was corrected for the unequal flow rates from the different channels. The outputs were standardized for time by dividing by the ratio of the time the channel was open to the longest time that a channel was open, in this case the Ag dispensing channel (Equation A.2).

$$y = \frac{\frac{\text{Concentration Metal (ppm)}}{\text{Concentration Ag (ppm)}} * \frac{\text{Flow Rate Ag Channel}}{\text{Flow Rate Metal Channel}}}{\frac{\text{Time Metal Channel Open}}{\text{Time Ag Channel Open}}} \qquad \textbf{(Equation A.2)}$$

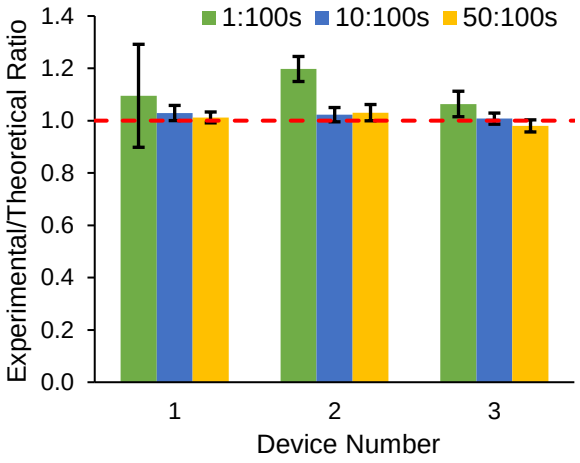

Figure A.6: ICP-OES results on formulations created by time-division multiplexing. One channel dispensed 4% $HNO_{3(aq)}$ while the other four channels dispensed a dilute metal standard in 4% $HNO_{3(aq)}$. ICP-OES was performed on an Optima 7000 DV. Three separate microformulators were tested, and error bars represent ± SD from the mean (n=5).

Significant differences ($p < 0.05$) exist between the idealized ratios and the ratios actually dispensed for two of the 1s samples. Unlike what was observed in the equal-time experiments, data obtained after time-division multiplexing exhibits heteroscedasticity. As the time that the ports are open decreases, seemingly negligible effects become amplified. It should be noted that for all times greater than that required for a half revolution of the pump (1.5 s) no significant differences were observed between predicted and observed values. We believe this is due to the combination of the twofold rotational symmetry of the rotor and using our current pump fluidic design. Future fluidics will aim to reduce the uncertainties in the formulated mixtures by eliminating the backflow observed with the current design.

The design of this new microformulator is highly adaptable. The addition of more ports in the valve will allow for an even larger number of analytes to be incorporated into user-defined mixtures. This would be particularly useful for long-term OoC experiments exploring the effects

of a wide array of chemicals. Additionally, the fludic and rotor width of the pump can be altered to allow for smaller or larger flow rates as needed. In OoCs with small chamber volumes such as those mimicing the blood-brain barrier, low flow rates are crucial to ensure cell survival. Previous microformulators utilized multiple solenoid valves or pneumatic actuators. By eliminating these expensive device components fabrication costs were decreased by over an order of magnitude. Overall, the relatively low cost devices described here have the potential to significantly impact the growing field of OoCs by dispensing user-defined mixtures using time-division multiplexing which allows for an array of chemical perturbations without the need for device disassembly.

Appendix B

APPLICATIONS OF MULTIANALYTE MICROPHYSIOLOGICAL DEVICES

Advances in scientific instrumentation have allowed experimentalists to evaluate well-known systems in new ways and to gain insight into previously unexplored or poorly understood phenomena. This appendix focuses on such instrumentation being developed within the growing field of multianalyte physiometry, specifically that capable of electrochemically measuring changes in the concentration of various metabolites in real time. By simultaneously quantifying multiple analytes, multianalyte microphysiological devices (MAMPDs) have begun to unravel the complex pathways that govern biological responses to ischemia and oxidative stress while contributing to basic scientific discoveries in bioenergetics and neurology. Patients and clinicians have also benefited from the highly translational nature of multianalyte physiometry, and the continued expansion of the repertoire of analytes that can be measured with MAMPDs will undoubtedly play a role in the automation and personalization of medicine. This is perhaps most evident with the recent advent of fully integrated noninvasive sensor arrays that can continuously monitor changes in analytes linked to specific disease states and deliver a therapeutic agent as required without the need for patient action.

Strategies for Avoiding Electrochemical Interference

Measurements made in poorly defined media or environmental conditions within an organism may encounter electrochemical interference. This interference can come from both direct sources, such as redox active species, and indirect sources, such as biofouling, and

commonly manifests as artificial changes in current or potential, plaguing electrochemical investigations. The need to measure signal coming only from analytes of interest has led investigators to develop several methods capable reducing the impacts of electrochemical interference, including 1) using electrostatic polymer barriers,[170–176] 2) shifting the overpotential through electrode modifications,[177–183] and 3) limiting electrode exposure time to the interfering species.[184]

Polymer barriers such as polypyrrole and Nafion films can reduce the interference of redox active species, such as dopamine (DA) and ascorbic acid (AA), commonly encountered when making electrochemical measurements *in vivo*. These polymers are charged, and as such they form an electrostatic barrier around the electrode that can prevent the approach of charged species. For example, 3,4-dihydroxyphenyl-L-alanine (L-DOPA) is used to treat Parkinson's disease but polymerizes on the surface of carbon microelectrodes forming melanin and acting as an interferent.[173] This biofouling is largely mitigated at high concentrations of L-DOPA by electrochemically preconditioning a carbon microfiber electrode and electrodepositing a thin film of Nafion onto the surface of the electrode, maintaining the sub-second response times associated with fast-scan cyclic voltammetry (FSCV).[173] Without the Nafion layer, L-DOPA treatment appeared to inhibit the release of DA, but with the Nafion layer, L-DOPA treatment was observed to enhance DA release in neural pathways associated with Parkinson's disease, which highlights the role of electrode design in understanding biochemical pathways *in vivo*.[173]

Direct interference can also be avoided by shifting the potential at which amperometric measurements are made.[177–183] Shifting of the needed overpotential can be accomplished by either coating or impregnating the working electrode with dyes such as Meldola's blue (MB) and Prussian blue (PB). For example, carbon electrodes modified with MB can be used to monitor

enzymatic reactions involving the production of NADH, but AA interferes with these measurements.[179] NADH is frequently detected at ~0.6 V, the same potential as AA. Incorporation of MB into the electrode shifts the needed potential down to +0.1 V 24 where AA does not become oxidized and thus does not contribute to the measured current. Measuring NADH has been used to diagnose and monitor the intrahepatic cholestasis of pregnancy.[179] When diagnosing and monitoring this it is imperative that biosensors utilizing 3-HSD respond only to analytes of interest where artificially large currents resulting in a false positive could lead to unnecessarily inducing labor.

In Vitro Multianalyte Microphysiometry

Reductionist approaches have allowed researchers to perform investigations that would otherwise be significantly more difficult, expensive, or unethical to conduct *in vivo*. In the field of drug discovery, for example, high throughput *in vitro* assays are essential for screening libraries of drug candidates. The development and application of MAMPDs for *in vitro* studies is described here with a focus on the multianalyte microphysiometer (MAMP) and its successor, the microclinical analyzer (μCA).

Multianalyte Microphysiometer

To build a MAMP, a sensor head from a commercially produced device known as the Cytosensor Microphysiometer was modified by the addition of platinum electrodes.[185] The original device was capable of only measuring changes in extracellular acidification within a 3 μL chamber using a light addressable potentiometric sensor.[186] By inserting the platinum electrodes, amperometric measurements were also made possible. The modification of the

electrodes' surfaces with immobilized films of oxidases provided information about changes in the extracellular concentration of glucose and lactate while a platinum electrode coated with Nafion revealed changes in oxygen consumption.[187] This allowed researchers to probe metabolic changes within specific populations of cells in response to various conditions, including oxidative burst, aglycemia, and treatment with chemical and biological toxicants.[185,187–199]

Microclinical Analyzer

The MAMP was limited by the fact that the sensor head was placed directly above the cell bed. While it was possible to probe excised pancreatic islets and co-cultures of neurons and glia,[191,196] this technology could not be expanded to incorporate multiple organ systems. With the emergence of OoCs that seek to recreate milli- and microhumans, a new strategy had to be devised. This role has been filled by the μCA.[200] By separating the sensing element from the cell bed, the μCA can be adapted to interface with OoCs such as the neurovascular unit-on-a-chip (NVU) which recreates the blood-brain barrier (BBB).

Metabolic changes after transient ischemic attacks in neuronal monocultures and co-cultures with glia were previously studied with the MAMP.[191] These investigations demonstrated that lactate levels are less predictive of neuronal fate than extracellular acidification. Additionally, the results confirmed the protective effects of glial co-cultures and preconditioning with sublethal stresses. While this provided useful information about the viability of neurons, the system failed to reproduce the more structurally complex BBB.

As a vital component of the central nervous system, the BBB must be taken into account when developing new drugs to treat neurological disorders as well as when determining the toxicological effects of novel nanomaterials.[201] By coupling the NVU to an electrochemical

sensing device such as the μCA, time-resolved metabolic perturbations can be identified following various treatment protocols to yield information about the health of cells as well as the permeability of the BBB. This capability was assessed in a series of automated experiments using modified screen printed electrodes to amperometrically measure levels of glucose, lactate, glutamate, and acetylcholine.

Experimental Methods

The fabrication of the NVU has been described in depth elsewhere.[201] Its design is such that three layers of PDMS are bound together to create brain and vascular chambers separated by a polycarbonate membrane having 0.2 μm pores. The construction of the μCA has also been previously published.[200] Briefly, the sensor housing consists of two pieces of acrylic sealed together with magnets and screws. Within this housing is a 26 μL flow chamber in which is seated a screen-printed electrode array (SPEA). The SPEAs used in these experiments were manufactured by Pine Research Instrumentation and have five spatially separate electrodes (Figure B.1). SPEAs were cleaned and electrochemically modified using a CHI 1440 multipotentiostat and associated CHI software, and electrochemical calibrations and measurements of NVU effluent were made using a custom multipotentiostat and LabVIEW software.[202] Perfusion of the NVU occurred using programmable Just Infusion™ syringe pumps from New Era Pump Systems, Inc. operating at a flow rate of 2 μL/min. Bubble traps and their membranes were sourced from Cytosensor Microphysiometers manufactured by Molecular Devices.

All electrode cleaning and plating procedures were performed using a Ag/AgCl (3 M KCl) reference electrode and a freshly flame polished platinum mesh counter electrode. Prior to use, SPEAs were electrochemically cleaned. To remove silver from previous experiments, all

five electrodes of the SPEA were held at 3 V for in a solution of 1.0 M $HNO_{3(aq)}$ until visibly free of residual silver. The SPEA was then washed with DI water and placed into a solution of 0.5 M $H_2SO_{4(aq)}$ and held at 6 V until free of silver and other contaminants as evidenced by subsequent cyclic voltammograms (-0.2 to 0.7 V, 21 scans). Modification of the working disc electrodes was necessary to perform the amperometric detection of specific analytes, but first onto the large bar electrode was deposited a Ag/AgCl film. The SPEA was rinsed with DI water and placed into an aqueous solution of 0.3 M $AgNO_3$ and 1 M NH_3. A sweep-step procedure was then conducted with constant stirring to precondition the electrode surface and plate the silver film: 0.3 to 0.95 V at 0.5 V/s, 0.95 V for 30 s, 0.95 V to -0.15 V at 0.5 V/s, and -0.15 V for 450 s. After being rinsed with DI water, the SPEA was then placed into an aqueous solution of 0.05 M $FeCl_3$ and agitated for one minute. The modified SPEA was then rinsed with DI water, and the four working electrodes were again cleaned in 0.5 M H_2SO_4 at 6 V until free of silver.

Working electrodes were converted into biosensors by depositing films of cross-linked oxidases. First, a solution of bovine serum albumin (BSA, 50 mg) in 50 mM PBS (800 µL) was made. Oxidases of glucose, lactate, and glutamate were then separately dissolved at concentrations of 0.25 mg/mL, 10 mg/mL, and 5 mg/mL, respectively. To detect acetylcholine, a combined solution was made in the BSA/PBS mixture that was 5 mg/mL in both acetylcholinesterase and choline oxidase. Individual solutions of 5 mg/mL acetylcholinesterase and choline oxidase were also made. 10 µL aliquots of these solutions were made and frozen at -20˚C until needed. Prior to use, aliquots were thawed and had 0.1 µL of a 25% glutaraldehyde solution added. The cross-linking solution was then vortexed for 5 s and used immediately by hand-casting 1 µL onto the surface of the desired working disc electrodes. The films were allowed to dry at room temperature prior to being stored at 4˚C in 120 mM KCl and 2mM PBS.

Stock solutions of glucose, lactate, glutamate, and acetylcholine were made in 120 mM KCl in 2mM PBS as well as in the complete EBM-2 media formulations for both the brain and blood sides of the NVU, which use 1% and 5% FBS, respectively. An additional stock solution was made in the complete EBM-2 media that lacked an initial concentration of glucose. All calibrant solutions were diluted from these stocks.

Solutions were pushed through the μCA using the μF described in Appendix A. The five vented calibrant solutions were connected to the five port valve which fed into the RPPM. In some experiments, a bubble trap was placed between the RPPM and the μCA housing. In initial experiments, however, a thin punch-out polycarbonate membrane was used instead and was wet-loaded onto the O-ring of the μCA housing. AMPERE was used to control the movement of the valve and pump, and optimal sampling conditions were found by systematically varying the time that each valve position was opened as well as the pump speed. These variables were tuned to identify the minimal amount of sample that would be required to give a steady state measurement, the reason for this being the low flow rate of the media solution through the NVU. To identify artifacts resulting from the calibrations being performed in increasing, decreasing, or random concentration, an experiment was performed over the course of ten hours that ran all three protocols in an automated fashion, with and without the use of an external bubble trap. Off-line measurements of NVU effluent were accomplished by performing one calibration every ten media samples and eliminated the use of the RPV in favor of manually changing the inlet tube to the various solutions to be tested. However, on-line automated measurements of NVU effluent were also made. This allowed for the determination of the amount of diffusion through the polycarbonate membrane separating the brain and vascular chamber prior to the addition of cells to form the BBB.

Results & Discussion

An electrode modified as depicted in Figure B.1 was used to determine the optimal RPPM parameters. They were determined to be 2 rpm for 90 s. This allowed for sub-120 µL volumes to be used, corresponding to time resolution better than 1 hr for the NVU effluent. Calibration curves obtained using these parameters are shown in Figure B.1.

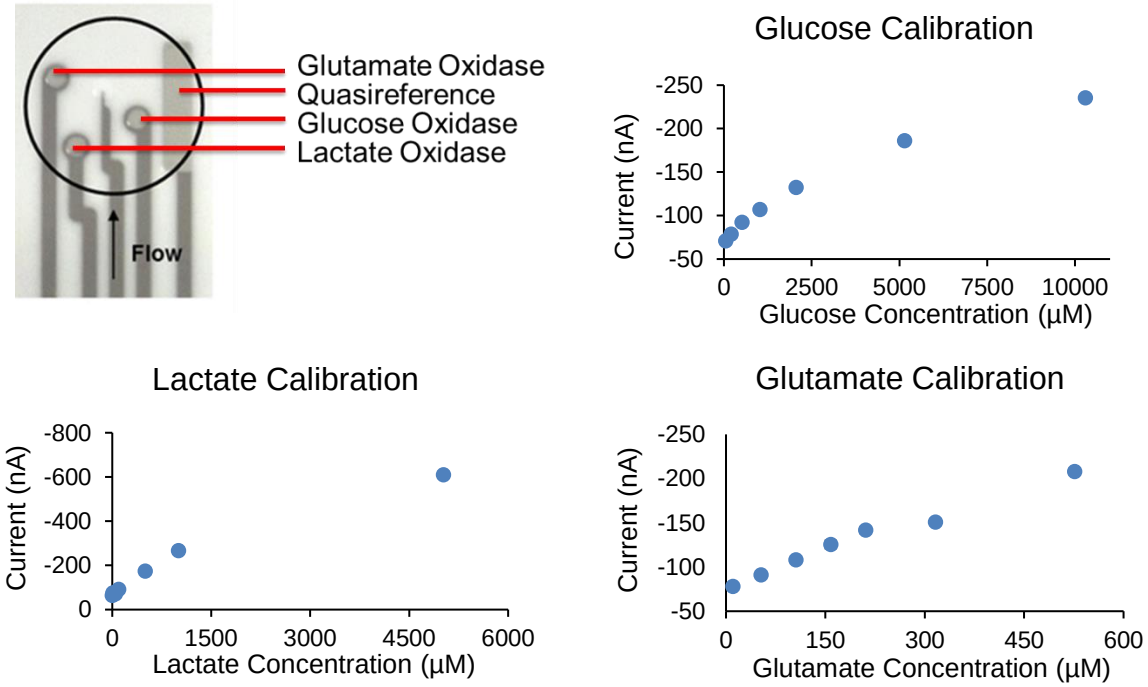

Figure B.1: Diagram of SPEA and example calibrations of glucose, lactate and glutamate electrodes.

Glucose, lactate, and glutamate were quantified using enzymatic biosensors incorporating their respective oxidase. However, for some metabolites of interest, such oxidases are not available. One example of this is acetylcholine (ACh), a common neurotransmitter. To quantify ACh, a similar two-part strategy was employed (Figure B.2). One enzyme, acetylcholinesterase (AChE), deacetylated ACh to give choline which was subsequently oxidized by choline oxidase (ChOx), producing hydrogen peroxide. SPEAs modified with three enzymatic films (AChE only,

ChOx only, and AChE/ChOx) were used in combination with the µCA, and only the film with the co-immobilized enzymes showed current response when exposed to solutions of ACh. The calibration curve for this reactive electrode is shown below in Figure B.2.

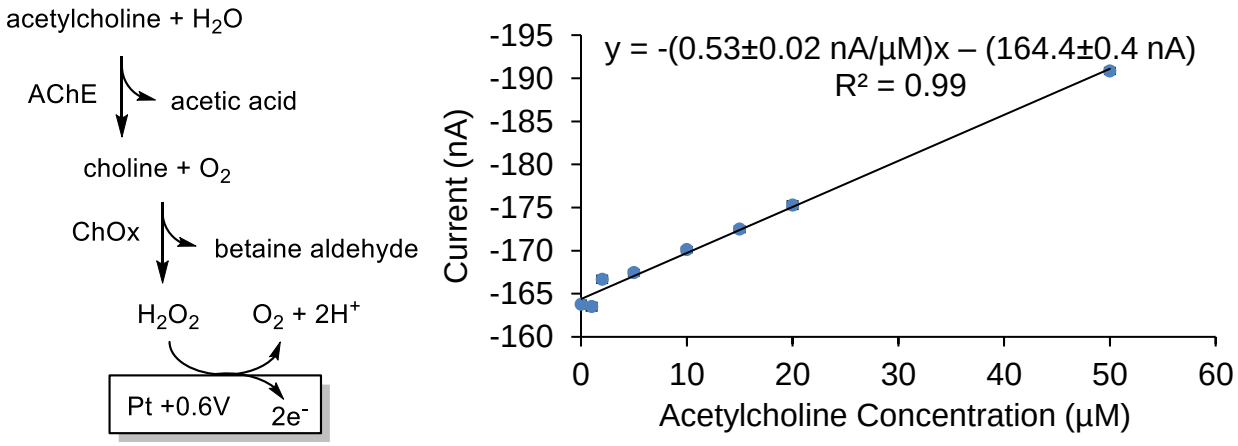

Figure B.2: Detection strategy for acetylcholine and example calibration of an electrode with a co-immobilized film of acetylcholinesterase and choline oxidase.

Initial experiments performed to determine the impact of calibrant order on the observed sensitivities yielded data plagued by seemingly random noise (Figure B.3). The significant losses and sudden rebounds in sensitivity suggested that calibrations would need to be performed immediately prior to running each sample. However, closer inspection of the device assembly revealed the slow accumulation of bubbles within the microfluidics, likely a result of the permeability of PDMS to air. When dislodged from the fluidics, the bubbles would occasionally become stuck on the surface of the SPEA within the µCA housing as a result of surface tension. Not only did the introduction of air bubbles disrupt the flow within the chamber, but when directly atop electrode surfaces it would drastically impact the sensitivity of individual electrodes until dislodged, as seen in the glutamate calibrations of Figure B.3. Because air bubbles have long been known to affect the performance of microfluidic devices, various strategies have been developed to counteract them. The MAMP used a serpentine flow chamber with a debubbler

membrane, and the use of this technology with the μCA dramatically improved the stability of the glucose and glutamate sensors (Figure B.3). For the lactate sensor, however, it revealed a time-dependent sensitivity loss, reinforcing the need to perform frequent calibrations.

Off-line measurements of NVU effluent during cell loading are summarized in Table B.1. During the first 8 days of loading, the levels of lactate and glutamate on the brain side appear to decrease. Both of these then increase on the brain side approximately a week later. Measurements on effluent from the vascular side vary more dramatically with no discernable trend. However, it is interesting to note that Device 52 was contaminated by microbial growth during the endothelial loading on the vascular side, and this correlated to the highest observed lactate levels in any of the samples. The observed lactate concentration on the brain side remained seemingly unaffected.

Automated crossover experiments were performed to determine the extent to which mixing occurs between the brain and vascular sides of the NVU without the presence of an endothelial barrier. By allowing 120 μL samples from each of the two chambers to accumulate over an hour while PBS and calibrant solutions were running through the μCA, lactate levels were measured using an electrode modified with three drop-cast films of cross-linked lactate oxidase and BSA. Crossover was evaluated by comparing differences in peak currents generated by the two 120 μL samples and the difference in peak currents generated by samples of the same two solutions prior to their being perfused into the NVU. The results demonstrated that only 10±7% crossover occurs without the cellular barrier, providing an explanation for the previously observed large increase in vascular lactate following contamination while the brain lactate was similar to that in other devices. Future crossover experiments incorporating endothelial cells are expected to bring this value even closer to zero as the BBB is recreated *in vitro*.

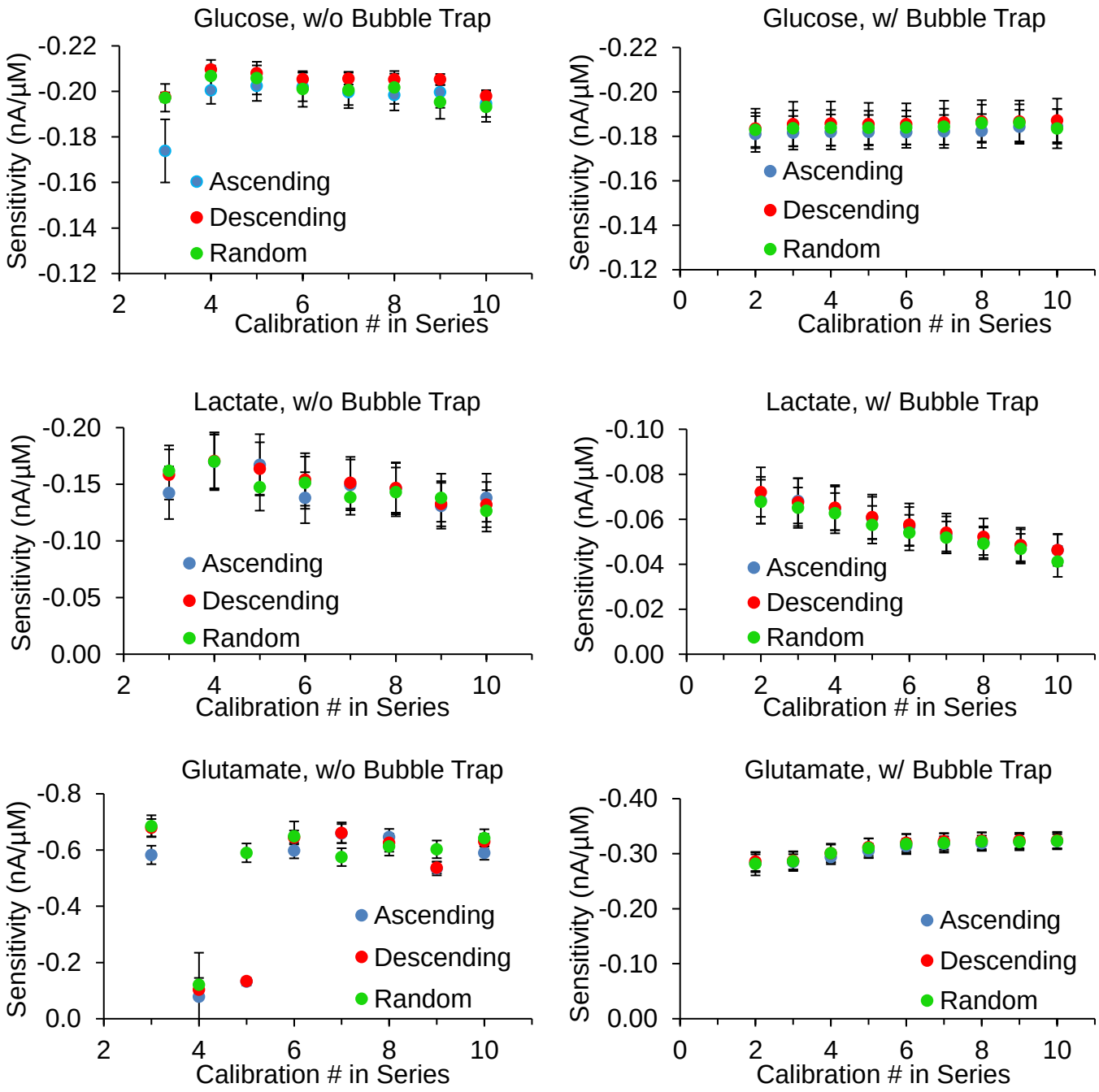

Figure B.3: Calibrations of glucose, lactate, and glutamate sensors before and after the incorporation of a bubble trap. The elimination of bubbles results in more reproducible sensitivities over the course of ten hours of continuous calibrations and allows for the identification of time-dependent sensitivity losses to be identified, as in the case of lactate oxidase.

		Brain						Blood					
		Glucose (mM)		Lactate (μM)		Glutamate (μM)		Glucose (mM)		Lactate (μM)		Glutamate (μM)	
		Avg	Std Dev	Avg	Std Dev	Avg	Std Dev	Avg	Std Dev	Avg	Std Dev	Avg	Std Dev
NVU Batch A	NVU54 0-3d	4.7	0.3	450	40	50	7	5.5	0.3	510	70	100	10
	NVU54 3-5d	4.9	0.3	220	30	23	5	4.7	0.2	340	60	69	8
	NVU54 5-8d	4.7	0.3	140	20	12	5	4.4	0.2	120	70	19	8
	NVU53 0-3d	3.8	0.3	430	40	62	7	4.4	0.2	410	60	79	8
	NVU53 3-5d	3.9	0.3	240	30	33	6	4.5	0.2	-60	50	8	7
	NVU53 5-8d	4.0	0.3	0	20	-1	5	4.3	0.2	330	60	46	8
	NVU52 0-3d	3.8	0.3	420	30	30	6	4.3	0.2	1100	100	120	10
	NVU51 0-3d	4.1	0.3	390	30	37	7	5.0	0.2	590	70	50	10
	NVU51 3-5d	4.1	0.3	210	30	20	7	5.0	0.3	-570	70	-72	7
	NVU51 5-8d	4.3	0.3	120	20	3	5	5.4	0.3	-780	60	-78	7
NVU Batch B	NVU35 3-6d	4.2	0.3	440	40	42	7	5.4	0.3	110	50	-5	8
	NVU35 15-18d	4.1	0.3	590	50	55	8	5.8	0.3	-70	50	-19	8
	NVU36 3-6d	3.9	0.3	460	40	41	6	5.6	0.3	40	50	-5	9
	NVU36 15-18d	3.5	0.3	890	60	70	7	5.7	0.3	20	50	-8	9
	NVU37 3-6d	4.4	0.3	420	40	30	6	5.4	0.3	-100	50	21	8
	NVU37 15-18d	3.7	0.3	730	50	91	8	5.2	0.3	280	70	26	9
	NVU38 3-6d	3.8	0.3	480	40	59	7	5.5	0.3	-100	50	-2	8
	NVU38 15-18d	3.8	0.3	730	50	107	8	5.4	0.3	400	60	20	10

Table B.1: Measurements of glucose, lactate, and glutamate in the effluent of NVUs. Two batches of NVUs were investigated, and multiple time points were taken. Trends in lactate and glutamate are apparent for the brain side, but the vascular chamber exhibits more erratic variations.

In Vivo Multianalyte Microphysiometry

Due to the failure of *in vitro* models to accurately predict the efficacy of certain drugs *in vivo*, the need for animal and human trials remains. Several factors may contribute to the discrepancy between predicted vs observed therapeutic effects, including poor bioavailability of the compound and off-target toxicity of the drug or its metabolites. Although reductionist approaches have provided insight into the complex biochemical pathways that exist within the human body, it can be particularly difficult to predict off-target effects prior to *in vivo* testing. Additionally, the shift of the medical field toward personalized medicine makes it advantageous to develop methodologies that allow for continuous patient monitoring for an extended period of time.

Microdialysis Probes

Monitoring metabolic changes within the brain can help elucidate the biochemical basis of a variety of neural pathologies. Because AA is a known interferent in experiments such as these, shifting the potential used can help signal overlap with analytes of interest. Secondary enzymes such as horseradish peroxidase (HRP) can be included to shift the potential needed for amperometric detection of glucose and lactate down to -0.1 V by adding ferrocene to the buffer used to carry the dialysate sample through FIA systems.[174,177,178,182,203,204] The use of rapid sampling microdialysis (rsMD) allows for on-line measurements of patient samples in FIA systems.[174,177,178,182,203,204] When coupled with other methods of monitoring brain activity such as electrocorticography, correlations can be made between extracellular concentrations of glucose and lactate and spreading depolarizations (SDs) in perilesional tissue following traumatic brain injury.[174,178] After the SD wave passes through the perilesional tissue, significant decreases in glucose and increases in lactate concentrations are noted, likely the result of cellular recovery.[178] The observation that the changes in extracellular glucose and lactate concentrations occur after the SD wave has passed successfully demonstrates that the SD wave is likely the cause and not the effect of changes in cellular metabolism. For patients experiencing frequent SDs, the extracellular glucose concentration fails to reach pre-SD levels before the next wave again depolarizes the cells, suggesting that a prolonged hypoglycemic milieu may contribute to the poorer outcome for these patients.[178]

As with traumatic brain injuries, localized physiological monitoring after surgical procedures can provide insight into recovery mechanisms as well as provide a personalized approach to medicine to predict patient outcome and alter the course of treatment as necessary. One such procedure is surgical anastomosis, the tethering of tubes or channels such as blood

vessels or intestines. Following an anastomosis, the lactate to glucose (L:G) ratio determined through FIA using rsMD may continue to increase near the surgical site indicating local hypoxia.[177,182] Ischemic conditions, which often require surgical intervention if prolonged, have been evaluated in porcine bowels.[177] Using an intramurally inserted microdialysis probe into porcine bowels, glucose and lactate were measured both before and after repeated simulated ischemic conditions.[177] As ischemia set in, the concentration of glucose decreased with a simultaneous rise in lactate concentration. Upon reperfusion, the levels returned to baseline, but the effects of a secondary ischemic event were more severe than those seen in the first, suggesting that the tissue did not fully recover from the first ischemic event or was more susceptible to future events.[177] In experiments such as these, the ratio of the analytes provides a better picture of the metabolic processes as slight changes in the position of the microdialysis probe can alter the measurements dramatically. This is in part due to the flushing effect of the microdialysis perfusion fluid over time causing artificially decreased absolute concentrations of analytes being measured under conditions where nutrients are not being replaced as seen in ischemia.

Monitoring of free flap surgical procedures through FIA with rsMD predicts patient outcome using the L:G ratio.[182] After anastomosis of the arteries and veins of the free flap, the L:G ratio is expected to return to near pre-operative baselines as the nutrient supply is restored and wastes are carried away. Cases in which the ratio did not return to baseline but instead continued to steadily increase were those where the anastomosis had failed or a thrombosis developed.[182] Interestingly, the effect of the topical vasodilator papaverine was also observed in real time as absolute concentrations of glucose and lactate both increased due to the increase in blood flow to the area.[182]

The microdialysis platforms used in these studies have limited temporal resolution in part due to the downstream injection system. However, the use of microdialysis probes is not limited to FIA platforms. Continuous measurements of the microdialysate using traditional enzymatic biosensors can improve temporal resolution.[174] In the case of SD wave passages, where the L:G ratio increases as discussed above,[178] on-line sensors are capable of continuously measuring glucose and potassium ion concentrations. Using a potassium ion selective electrode and the glucose biosensor to monitor induced SD in mice, temporal resolution was improved by a factor of 60, down to 1 second.[174] Using this method, the decrease in extracellular glucose was temporally resolved from the increase in potassium ion concentration, demonstrating that the drop is glucose is in response to the increased metabolic demands of the neurons undergoing repolarization.[174]

Implantable Electrodes

Electrodes may also be directly implanted *in vivo* to probe complex biochemical pathways that are difficult or impossible to reproduce *in vitro*, such as those seen in the brain. These *in vivo* electrodes can therefore preserve information about sub-second cellular responses, a daunting task for microdialysis and flow injection methods. However, implanted electrodes present their own set of challenges: the sensitivity of the electrodes must remain constant and they must be very small or risk a trade-off of spatial resolution for temporal resolution.

Two broad categories of electrodes have proven efficient in maintaining spatial resolution for *in vivo* physiological measurements: metallic microelectrode arrays[170,175,176] and carbon fiber microelectrodes.[173,205–210] Metal microelectrode arrays are slightly larger than carbon fiber electrodes because they spatially separate the surface at which each analyte is detected by

electrode-specific functionalization such as enzymatic or ion-selective films. However, this separation allows for more specific detection of each analyte of interest by decreasing the degree of interference between different analytes while maintaining high sensitivity for individual analytes.[170,171,175,176,180,183,211] Some metal electrodes are not suitable for implantation despite their ubiquity in *in vitro* devices. For example, Ag/AgCl film electrodes have been shown to elicit inflammatory responses *in vivo*.[175] Alternatively, IrO_2 is a biocompatible reference electrode that exhibits long-term stability and low noise *in vivo*. This electrode is, however, sensitive to pH changes and may only be suitable in regions of the body where pH changes are minimal, such as the brain.[175] Metal electrodes have been used to measure physiological changes in the brain in response to mechanical and chemical stimuli. For example, the release of neurotransmitters in the striatum of rats in response to electrical stimuli and physical stresses can be monitored with sub-second temporal resolution using platinum electrodes.[176] The second category of implantable electrodes, carbon fiber microelectrodes, has superior spatial resolution relative to metal electrodes. Carbon fiber microelectrodes are frequently used with FSCV to quantitate catecholamines such as DA.[173,205–207,210] Because DA adsorbs well to the surface of carbon fiber microelectrodes, faster scan rates are used to maximize signal. Traditionally, this is accomplished by using a triangular waveform, but novel waveforms such as the "sawhorse" scan which briefly holds the potential above +1.0 V further improve sensitivity by opening up sites on the electrode for DA to bind.[207] This can be used to deconvolute signals arising from mixtures of redox active molecules such as adenosine, ATP, and H_2O_2.[212]

Long-term studies with implantable electrodes are limited by their decreased sensitivity over time. Loss of sensitivity is primarily due to biofouling and is compounded by the inability to recalibrate electrodes once implanted.[170] Biofouling of GOx, LOx, and pyruvate oxidase

(POx) coated electrodes results in a diffusion barrier shown to decrease sensitivity *in vivo*.[170] However, the purposeful use of diffusion barriers, such as microdialysis membranes has been shown to extend the linear range of electrodes as well as reduce biofouling. For example, LOx films protected by a microdialysis membrane better retained sensitivity compared to GOx and POx films without the protective membrane.[170] Alternatively, FSCV can be used to extend the lifetime of implanted electrodes by eliminating the assumption that the electrode sensitivity is constant during the course of an experiment. It does so by fitting the total background current and switching potential to a model with four regression coefficients.[209] This method has accurately predicted the sensitivity of a carbon fiber microelectrode for a variety of analytes *in vivo*, including DA, AA, H_2O_2, and H^+.[209]

Spatial mapping can be accomplished by electrochemically evaluating how cells respond to different stimuli. By determining how cells respond to DA, medium spiny neurons can be subtyped, mapping the nucleus accumbens in behavioral studies.[205] When iontophoresed stimulants are not redox active in the potential range being swept with FSCV, redox active compounds such as DOPAC[208] and acetaminophen[205] can be added to the iontophoresed solution to act as internal standards. Glutamate, an iontophoresed stimulant that is not redox active, can be accurately quantified by such internal standards.[208]

By simultaneously using electrodes at different locations, responses in different regions of the brain may be seen as a result of a single stimulus.[206] For example, DA can be tracked in the nucleus accumbens while 5-HT is tracked in the substantia nigra pars reticulata to investigate the mechanisms governing their release. Upon stimulation, DA release in the nucleus accumbens is 300 times greater than 5-HT release in the substantia nigra pars reticulata despite them being similar in overall concentration within their respective tissue.[206] By selectively inhibiting

enzymes responsible for the synthesis, packaging, release, uptake, and metabolism of these two neurotransmitters, the dependence of DA transmission on synthesis and repackaging and the tight regulation of 5-HT transmission by reuptake and degradation pathways were revealed. Additionally, the severe neurological consequences resulting from the co-administration of 5-HT transporter and monoamine oxidase inhibitors were observed.[206]

Wearable Devices

As manageable chronic conditions such as diabetes mellitus, hypertension, and hyperlipidemia become more prevalent, the demand for minimally invasive continuous monitoring devices increases. Wearable devices are now capable of monitoring many different analytes simultaneously, have readouts that interface with mobile phones, and can deliver a therapeutic agent.[180] Devices that utilize bodily fluids other than serum and cerebral spinal fluid such as sweat and urine are becoming increasingly common in part due to the ease by which samples can be obtained.[171,180,183,211] The 'diabetes patch' sits on the surface of the skin, monitors temperature, humidity, pH, and glucose levels, and delivers Metformin as needed. In the device, glucose is measured by the amperometric detection of peroxide on gold-doped graphene modified with PB and GOx at -0.05 V. By using additional sensors to assess pH and temperature, corrections can be made for the activity of GOx, yielding more accurate glucose readings. When hyperglycemic conditions are detected, a thermal actuator will melt polymeric microneedles incorporating Metformin, releasing it into the bloodstream. This patch is capable of continuously monitoring glucose levels over an entire day, and such non-invasive platforms may someday replace current methods of monitoring and managing blood glucose levels.

Wearable MAP microanalytical devices have also been utilized in exercise training

regimens to gain insights into individual performance. Two of the most promising are a 3D-printed microfluidic device and ‘smart bands.’ The 3D-printed microfluidic devices have a subcutaneous microdialysis probe that allows external needle-based electrodes to continuously monitor glucose and lactate levels.[213] The needle electrodes are removable from the device housing and can be easily modified to measure different analytes as desired. Although technically wearable, this device is still reliant upon an external potentiostat and requires a clinician to subcutaneously insert the microdialysis probe.[213] On the other hand, a recently developed 'smart headband/smart wristband' can simultaneously and non-invasively measure glucose, lactate, Na^+, and K^+ levels in sweat.[183] In these smart bands, GOx- and LOx-chitosan-SWCNT films on PB are used for chronoamperometric detection of glucose and lactate, respectively, whereas Na^+ and K^+ levels are determined *via* open circuit potential using ionophores (Na ionophore X and valinomycin) in ion-selective membranes atop PEDOT:PSS. When access to water is restricted during exercise while wearing the flexible integrated sensor array (FISA), dehydration can be clearly seen when concentrations of sodium and potassium begin to significantly increase. In combination with the real-time profiles of glucose and lactate, athletes undergoing intense training can avoid over-exertion and gain physiological insights into individual performance.

Wearable FISAs have also incorporated ion-selective membranes to continuously measure Ca^{2+} and pH levels to determine hydration and electrolyte levels. Ca^{2+} concentration and pH are measured through films incorporating calcium ionophore II on PEDOT:PSS and electropolymerized polyaniline.[211] As with sodium and potassium, calcium ion concentration can be monitored with open circuit potential measurements in sweat during the course of a workout, and the *in vivo* stability of the reference electrode can be enhanced by the incorporation of a

poly-vinyl butyral layer to maintain chloride ion saturation at the Ag/AgCl film with little interference from other common cations, including NH_4^+, Mg^{2+}, K^+, and Na^+. The results obtained with the FISA for both pH and Ca^{2+} aligned well with the results from commercial pH meters and ICP-MS, the gold-standard for Ca^{2+} measurement, indicating that these wearable platforms can be used in clinically relevant conditions such as hyperparathyroidism and kidney stones.

The quantitation of other metal species bears clinical relevance due conditions such as Wilson's disease and acute heavy metal poisoning. Heavy metals can be detected by square wave anodic stripping voltammetry relying on the inherent redox potentials of the metal species being evaluated. The redox potentials of zinc, copper, cadmium, lead, and mercury are sufficiently separated to allow their quantitation in a complex mixture.[171] The strong correlation between values obtained from a sweat sample using ICP-MS and the wearable sensor indicates that these wearable sensors can also be used reliably for heavy metal detection in addition to the analytes previously discussed.[171,183,211] These advances significantly expand the number of cationic species that can be continuously evaluated in biofluids such as sweat and urine with wearable sensors, thus enlarging the diagnostic toolbox in the field.

Conclusions

The in-house modification of commercially available instruments to convert single analyte detection systems into those capable of measuring multiple analytes has largely become obsolete in part due to the advent of screen printed electrodes and 3-D fabrication techniques. The inclusion of customizable sensors into microfluidic devices has enabled multianalyte detection under physiological conditions, allowing researchers to make advances in the fields of

bioenergetics, toxicology, and neurology. These devices also show great promise in clinical settings due to their capabilities of continuously monitoring vitals and predicting patient outcome. As the medical field shifts toward more personalized approaches, the widespread adoption of devices that can perform multianalyte detection is inevitable as evidenced by the continued success of the i-STAT. Outside of research and clinical settings, non-invasive smart bands are beginning to allow athletes to optimize training regimens, and the self-contained nature of these robust fully integrated sensor arrays in combination with their low power usage makes them ideal for use in low resource monitoring settings as well. Overall, multianalyte investigations will continue to grow in number as the monitoring of a panel of analytes is more broadly recognized for its utility in gaining a better understanding of fundamental cellular processes and disease states.

REFERENCES

(1) Freestone, I.; Meeks, N.; Sax, M.; Higgitt, C. *Gold Bull.* **2007**, *40*, 270–277.

(2) Heiligtag, F. J.; Niederberger, M. *Mater. Today* **2013**, *16*, 262–271.

(3) Reibold, M.; Paufler, P.; Levin, A. A.; Kockmann, W.; Pätzke, N.; Meyer, D. C. *Nature* **2006**, *444*, 286–286.

(4) Hulla, J.; Sahu, S.; Hayes, A. *Hum. Exp. Toxicol.* **2015**, *34*, 1318–1321.

(5) Binnig, G.; Rohrer, H. *IBM J. Res. Dev.* **1986**, *30*, 355–369.

(6) Binnig, G.; Quate, C. F.; Gerber, C. *Phys. Rev. Lett.* **1986**, *56*, 931–933.

(7) Vance, M. E.; Kuiken, T.; Vejerano, E. P.; McGinnis, S. P.; Hochella, M. F.; Hull, D. R. *Beilstein J. Nanotechnol.* **2015**, *6*, 1769–1780.

(8) World Health Organization. Life expectancy - Data by WHO region http://apps.who.int/gho/data/view.main.SDG2016LEXREGv?lang=en (accessed Jun 27, 2017).

(9) World Health Organization. Diarrhoeal disease http://www.who.int/mediacentre/factsheets/fs330/en/ (accessed Jun 27, 2017).

(10) Savage, N.; Diallo, M. S. *J. Nanoparticle Res.* **2005**, *7*, 331–342.

(11) Smijs, T. G.; Pavel, S. *Nanotechnol. Sci. Appl.* **2011**, *4*, 95–112.

(12) American Cancer Society. Key Statistics for Melanoma Skin Cancer https://www.cancer.org/cancer/melanoma-skin-cancer/about/key-statistics.html (accessed Jun 27, 2017).

(13) American Cancer Society. Breast Cancer Survival Rates https://www.cancer.org/cancer/breast-cancer/understanding-a-breast-cancer-diagnosis/breast-cancer-survival-rates.html (accessed Jun 27, 2017).

(14) Harry, S. R.; Hicks, D. J.; Amiri, K. I.; Wright, D. W. *Chem. Commun. (Camb).* **2010**, *46*, 5557–5559.

(15) Jackson, S. R.; Wong, A. C.; Travis, A. R.; Catrina, I. E.; Bratu, D. P.; Wright, D. W.; Jayagopal, A. *Applications of Hairpin DNA-Functionalized Gold Nanoparticles for Imaging mRNA in Living Cells*; 1st ed.; Elsevier Inc., 2016; Vol. 572.

(16) Lucky, S. S.; Soo, K. C.; Zhang, Y. *Chem. Rev.* **2015**, *115*, 1990–2042.

(17) Huang, X.; El-Sayed, M. A. *J. Adv. Res.* **2010**, *1*, 13–28.

(18) van der Merwe, D.; Pickrell, J. A. *Vet. Toxicol.* **2012**, 383–390.

(19) Simpson, C. A.; Huffman, B. J.; Gerdon, A. E.; Cliffel, D. E. *Chem. Res. Toxicol.* **2010**, *23*, 1608–1616.

(20) Falagan-Lotsch, P.; Grzincic, E. M.; Murphy, C. J. *Proc. Natl. Acad. Sci.* **2016**, *113*, 13318–13323.

(21) Maurer-Jones, M. A.; Gunsolus, I. L.; Murphy, C. J.; Haynes, C. L. *Anal. Chem.* **2014**, *85*, 3036–3049.

(22) Hwang, J.; Jeong, Y.; Park, J. M.; Lee, K. H.; Hong, J. W.; Choi, J. *Int. J. Nanomedicine* **2015**, *10*, 5701–5713.

(23) Mas-Moruno, C.; Rechenmacher, F.; Kessler, H. *Anticancer. Agents Med. Chem.* **2010**, 753–768.

(24) Nguyen, L. A.; He, H.; Pham-Huy, C. *Int. J. Biomed. Sci.* **2006**, *2*, 85–100.

(25) Govindarajan, S.; Goldstein, R. A. *Proc. Natl. Acad. Sci. U. S. A.* **1998**, *95*, 5545–5549.

(26) Peterson, M. E.; Daniel, R. M.; Danson, M. J.; Eisenthal, R. *Biochem. J.* **2007**, *402*, 331–337.

(27) Zaks, A.; Klibanov, A. M. *Proc. Natl. Acad. Sci.* **1985**, *82*, 3192–3196.

(28) White, F. H. *J. Biol. Chem.* **1961**, *236*, 1353–1360.

(29) Houck, S. A.; Singh, S.; Cyr, D. M. *Methods Mol Biol.* **2012**, *832*, 455–461.

(30) Brundin, P.; Melki, R.; Kopito, R. *Nat Rev Mol Cell Biol.* **2010**, *11*, 301–307.

(31) American Cancer Society. Lung Cancer (Non-Small Cell) http://www.cancer.org/acs/groups/cid/documents/webcontent/003115-pdf.pdf (accessed Jun 30, 2016).

(32) National Cancer Institute. SEER Stat Fact Sheets: Lung and Bronchus Cancer http://seer.cancer.gov/statfacts/html/lungb.html (accessed Feb 24, 2016).

(33) Ellis, L. M. *Horizons Cancer Ther. From Bench to Bedside* **2002**, *3*, 4–22.

(34) Liu, Z.; Wang, F.; Chen, X. *Drug Dev Res* **2008**, *69*, 329–339.

(35) Liao, D.; Johnson, R. S. *Cancer Metastasis Rev.* **2007**, *26*, 281–290.

(36) Campbell, I. D.; Humphries, M. J. *Cold Spring Harb. Perspect. Biol.* **2011**, *3*, 1–14.

(37) Harburger, D. S.; Calderwood, D. A. *J. Cell Sci.* **2009**, *122*, 1472–1472.

(38) Ruoslahti, E. *Annu. Rev. Cell Dev. Biol.* **1996**, *12*, 697–715.

(39) Healy, J. M.; Murayama, O.; Maeda, T.; Yoshino, K.; Sekiguchi, K.; Kikuchi, M. *Biochemistry* **1995**, *34*, 3948–3955.

(40) Chen, K.; Chen, X. *Theranostics* **2011**, *1*, 189–200.

(41) Dal Pozzo, A.; Ni, M.-H.; Esposito, E.; Dallavalle, S.; Musso, L.; Bargiotti, A.; Pisano, C.; Vesci, L.; Bucci, F.; Castorina, M.; Foderà, R.; Giannini, G.; Aulicino, C.; Penco, S. *Bioorg. Med. Chem.* **2010**, *18*, 64–72.

(42) Xiong, X.-B.; Ma, Z.; Lai, R.; Lavasanifar, A. *Biomaterials* **2010**, *31*, 757–768.

(43) Liu, S. *Bioconjug. Chem.* **2009**, *20*, 2199–2213.

(44) Zhang, Z.; Lai, Y.; Yu, L.; Ding, J. *Biomaterials* **2010**, *31*, 7873–7882.

(45) Wängler, C.; Maschauer, S.; Prante, O.; Schäfer, M.; Schirrmacher, R.; Bartenstein, P.; Eisenhut, M.; Wängler, B. *Chembiochem* **2010**, *11*, 2168–2181.

(46) Xiong, J. P.; Stehle, T.; Diefenbach, B.; Zhang, R.; Dunker, R.; Scott, D. L.; Joachimiak, A.; Goodman, S. L.; Arnaout, M. A.. *Science* **2001**, *294*, 339–345.

(47) Xiong, J.-P.; Stehle, T.; Zhang, R.; Joachimiak, A.; Frech, M.; Goodman, S. L.; Arnaout, M. A. *Science* **2002**, *296*, 151–155.

(48) Stupp, R.; Hegi, M. E.; Gorlia, T.; Erridge, S. C.; Perry, J.; Hong, Y. K.; Aldape, K. D.; Lhermitte, B.; Pietsch, T.; Grujicic, D.; Steinbach, J. P.; Wick, W.; Tarnawski, R.; Nam, D. H.; Hau, P.; Weyerbrock, A.; Taphoorn, M. J. B.; Shen, C. C.; Rao, N.; Thurzo, L.; Herrlinger, U.; Gupta, T.; Kortmann, R. D.; Adamska, K.; McBain, C.; Brandes, A. A.; Tonn, J. C.; Schnell, O.; Wiegel, T.; Kim, C. Y.; Nabors, L. B.; Reardon, D. A.; van den Bent, M. J.; Hicking, C.; Markivskyy, A.; Picard, M.; Weller, M. *Lancet Oncol.* **2014**, *15*.

(49) Stupp, R.; Hegi, M. E.; Neyns, B.; Goldbrunner, R.; Schlegel, U.; Clement, P. M. J.; Grabenbauer, G. G.; Ochsenbein, A. F.; Simon, M.; Dietrich, P. Y.; Pietsch, T.; Hicking, C.; Tonn, J. C.; Diserens, A. C.; Pica, A.; Hermisson, M.; Krueger, S.; Picard, M.; Weller, M. *J. Clin. Oncol.* **2010**, *28*, 2712–2718.

(50) Vansteenkiste, J.; Barlesi, F.; Waller, C. F.; Bennouna, J.; Gridelli, C.; Goekkurt, E.; Verhoeven, D.; Szczesna, A..; Feurer, M.; Milanowski, J.; Germonpre, P.; Lena, H.; Atanackovic, D.; Krzakowski, M.; Hicking, C.; Straub, J.; Picard, M.; Schuette, W.; O'Byrne, K. *Ann. Oncol.* **2015**, 1734–1740.

(51) Manegold, C.; Vansteenkiste, J.; Cardenal, F.; Schuette, W.; Woll, P. J.; Ulsperger, E.; Kerber, A.; Eckmayr, J.; von Pawel, J. *Invest. New Drugs* **2013**, *31*, 175–182.

(52) Samant, R. S.; Shevde, L. A. *Oncotarget* **2011**, *2*, 122–134.

(53) Aggarwal, C.; Somaiah, N.; Simon, G. *Cancer Biol. Ther.* **2012**, *13*, 247–263.

(54) Kerbel, R. *N Engl J Med* **2008**, *358*, 2039–2049.

(55) Sandler, A.; Gray, R.; Perry, M. C.; Brahmer, J.; Schiller, J. H.; Dowlati, A.; Lilenbaum, R.; Johnson, D. H. *N Engl J Med* **2006**, *24*, 2542–50.

(56) Vokes, E.; Salgia, R.; Karrison, T. *Ann. Oncol.* **2013**, *24*, 6–9.

(57) Candelaria, M.; Garcia-Arias, A.; Cetina, L.; Dueñas-, A.; Dueñas-Gonzalez, A.; Dueñas-, A. *Radiat. Oncol.* **2006**, *1*, 1–17.

(58) Fowler, J.; Adams, G.; Denekamp, J. *Cancer Treat. Rev.* **1976**, *3*, 227–256.

(59) Wardman, P. *Clin. Oncol.* **2007**, *19*, 397–417.

(60) Mesbahi, A. *Reports Pract. Oncol. Radiother.* **2010**, *15*, 176–180.

(61) Tsai, M. F.; Chang, S. H. G.; Cheng, F. Y.; Shanmugam, V.; Cheng, Y. S.; Su, C. H.; Yeh, C. S. *ACS Nano* **2013**, *7*, 5330–5342.

(62) Misawa, M.; Takahashi, J. *Nanomedicine Nanotechnology, Biol. Med.* **2011**, *7*, 604–614.

(63) Maeda, H. *Adv. Enzyme Regul.* **2001**, *41*, 189–207.

(64) Shen, J.; Meng, Q.; Sui, H.; Yin, Q.; Zhang, Z.; Yu, H.; Li, Y. *Mol. Pharm.* **2014**, *11*, 2579–2591.

(65) Cun, X.; Chen, J.; Ruan, S.; Zhang, L.; Wan, J.; He, Q.; Gao, H. *ACS Appl. Mater. Interfaces* **2015**, *7*, 27458–27466.

(66) Huang, K.; Ma, H.; Liu, J.; Huo, S.; Kumar, A.; Wei, T.; Zhang, X.; Jin, S.; Gan, Y.; Wang, P. C.; He, S.; Zhang, X.; Liang, X. J. *ACS Nano* **2012**, *6*, 4483–4493.

(67) Wong, C.; Stylianopoulos, T.; Cui, J.; Martin, J.; Chauhan, V. P.; Jiang, W.; Popovic, Z.; Jain, R. K.; Bawendi, M. G.; Fukumura, D. *Proc. Natl. Acad. Sci. U. S. A.* **2011**, *108*, 2426–2431.

(68) Lee, H.; Fonge, H.; Hoang, B.; Reilly, R. M.; Allen, C. *Mol. Pharm.* **2010**, *7*, 1195–1208.

(69) Arvizo, R.; Bhattacharya, R.; Mukherjee, P. *Expert Opin Drug Deliv.* **2010**, *7*, 753–763.

(70) Hainfeld, J. F.; Slatkin, D. N.; Smilowitz, H. M. *Phys. Med. Biol.* **2004**, *49*, N309–N315.

(71) Su, N.; Dang, Y.; Liang, G.; Liu, G. *Nanoscale Res. Lett.* **2015**, *10*, 160.

(72) Hainfeld, J. F.; Dilmanian, F. A.; Zhong, Z.; Slatkin, D. N.; Kalef-Ezra, J. A.; Smilowitz, H. M. *Phys. Med. Biol.* **2010**, *55*, 3045–3059.

(73) Hainfeld, J. F.; Smilowitz, H. M.; O'Connor, M. J.; Dilmanian, F. A.; Slatkin, D. N. *Nanomedicine (Lond).* **2013**, *8*, 1601–1609.

(74) Zhang, X.-D.; Wu, D.; Shen, X.; Chen, J.; Sun, Y.-M.; Liu, P.-X.; Liang, X.-J. *Biomaterials* **2012**, *33*, 6408–6419.

(75) Miladi, I.; Alric, C.; Dufort, S.; Mowat, P.; Dutour, A.; Mandon, C.; Laurent, G.; Bräuer-Krisch, E.; Herath, N.; Coll, J. L.; Dutreix, M.; Lux, F.; Bazzi, R.; Billotey, C.; Janier, M.; Perriat, P.; Le Duc, G.; Roux, S.; Tillement, O. *Small* **2014**, *10*, 1116–1124.

(76) Khoshgard, K.; Hashemi, B.; Arbabi, A.; Rasaee, M. J.; Soleimani, M. *Phys. Med. Biol.* **2014**, *59*, 2249–2263.

(77) Wang, C.; Li, X.; Wang, Y.; Liu, Z.; Fu, L.; Hu, L. *J. Nanoparticle Res.* **2013**, *15*, 1–12.

(78) Gerdon, A. E.; Wright, D. W.; Cliffel, D. E. *Angew. Chem. Int. Ed. Engl.* **2006**, *45*, 594–598.

(79) Brauer, G. *HANDBOOK OF PREPARATIVE INORGANIC CHEMISTRY*; CURRENT SCIENCE ASSN: C V RAMAN AVENUE, PO BOX 8005, BANGALORE 560 080, INDIA, 1965; Vol. 1.

(80) *Med. Lett.* **1989**, *31*, 7–8.

(81) Templeton, A. C.; Chen, S.; Gross, S. M.; Murray, R. W.; Hill, C.; Carolina, N. **1999**, 66–76.

(82) Taherian, A.; Li, X.; Liu, Y.; Haas, T. A. *BMC Cancer* **2011**, *11*, 293.

(83) Franken, N. A. P.; Rodermond, H. M.; Stap, J.; Haveman, J.; van Bree, C. *Nat. Protoc.* **2006**, *1*, 2315–2319.

(84) Meier, J.; Kassler, K.; Sticht, H.; Eichler, J. *Beilstein J. Org. Chem.* **2012**, *8*, 1858–1866.

(85) Simpson, C. A.; Salleng, K. J.; Cliffel, D. E.; Feldheim, D. L. *Nanomedicine* **2013**, *9*, 257–263.

(86) Zhang, H.; Forman, H. J.; Choi, J. *Methods Enzymol.* **2005**, *401*, 468–483.

(87) Albert, J. M.; Cao, C.; Geng, L.; Leavitt, L.; Hallahan, D. E.; Lu, B. *Int. J. Radiat. Oncol. Biol. Phys.* **2006**, *65*, 1536–1543.

(88) Alkilany, A. M.; Nagaria, P. K.; Hexel, C. R.; Shaw, T. J.; Murphy, C. J.; Wyatt, M. D. *Small* **2009**, *5*, 701–708.

(89) Goel, A. K. *World J. Clin. cases* **2015**, *3*, 20–33.

(90) Spencer, R. C. *J. Clin. Pathol.* **2003**, *56*, 182–187.

(91) Centers for Disease Control and Prevention. Anthrax https://www.cdc.gov/nczved/divisions/dfbmd/diseases/anthrax/technical.html (accessed Jan 24, 2017).

(92) Centers for Disease Control and Prevention. Inhalation Anthrax https://www.cdc.gov/anthrax/basics/types/inhalation.html (accessed Jan 24, 2017).

(93) Fan, Y.; Moon, J. J. *Wiley Interdiscip. Rev. Nanomedicine Nanobiotechnology* **2016**.

(94) Riedel, S. *Proc. (Bayl. Univ. Med. Cent).* **2005**, *18*, 234–243.

(95) Nass, M. *Infect. Dis. Clin. North Am.* **1999**, *13*, 187–208.

(96) Beierlein, J. M.; Anderson, A. C. *Curr. Med. Chem.* **2011**, *18*, 5083–5094.

(97) Brossier, F.; Mock, M. *Toxicon* **2001**, *39*, 1747–1755.

(98) Bann, J. G. *Protein Sci.* **2012**, *21*, 1–12.

(99) Trescos, Y.; Tournier, J. N. *Toxins (Basel).* **2012**, *4*, 83–97.

(100) Collier, R. J.; Young, J. A. *Annu Rev Cell Dev Biol* **2003**, *19*, 45–70.

(101) Abrami, L.; Reig, N.; Van Der Goot, F. G. *Trends Microbiol.* **2005**, *13*, 72–78.

(102) Friedlander, A. M.; Little, S. F. *Vaccine* **2009**, *27*, 28–32.

(103) Brey, R. N. *Adv. Drug Deliv. Rev.* **2005**, *57*, 1266–1292.

(104) Fox, C. B.; Kramer, R. M.; Barnes V, L.; Dowling, Q. M.; Vedvick, T. S. *Ther. Adv. vaccines* **2013**, *1*, 7–20.

(105) Dykman, L. A.; Staroverov, S. A.; Bogatyrev, V. A.; Shchyogolev, S. Y. *Nanotechnologies Russ.* **2010**, *5*, 748–761.

(106) Dykman, L. A.; Khlebtsov, N. G. *Chem. Sci.* **2017**, *0*, 1–17.

(107) Cao-Milán, R.; Liz-Marzán, L. M. *Expert Opin. Drug Deliv.* **2014**, *11*, 741–752.

(108) Nambara, K.; Niikura, K.; Mitomo, H.; Ninomiya, T.; Takeuchi, C.; Wei, J.; Matsuo, Y.; Ijiro, K. *Langmuir* **2016**, *32*, 12559–12567.

(109) Niikura, K.; Matsunaga, T.; Suzuki, T.; Kobayashi, S.; Yamaguchi, H.; Orba, Y.; Kawaguchi, A.; Hasegawa, H.; Kajino, K.; Ninomiya, T.; Ijiro, K.; Sawa, H. *ACS Nano*

2013, *7*, 3926–3938.

(110) Chen, Y.-S.; Hung, Y.-C.; Lin, W.-H.; Huang, G. S. *Nanotechnology* **2010**, *21*, 195101.

(111) Gerdon, A. E.; Wright, D. W.; Cliffel, D. E. *Angew. Chem. Int. Ed. Engl.* **2006**, *45*, 594–598.

(112) Harkness, K. M.; Hixson, B. C.; Fenn, L. S.; Turner, B. N.; Rape, A. C.; Simpson, C. A.; Huffman, B. J.; Okoli, T. C.; McLean, J. A.; Cliffel, D. E. *Anal. Chem.* **2010**, *82*, 9268–9274.

(113) Golde, W. T.; Gollobin, P.; Rodriguez, L. L. *Lab Anim. (NY).* **2005**, *34*, 39–43.

(114) NIH Office of Animal Care and Use Animal Research Advisory Committee. Guidelines for Survival Bleeding of Mice and Rats. *Blood*, 2005, 1–5.

(115) Kurien, B. T.; Scofield, R. H. *Lab. Anim.* **1999**, *33*, 83–86.

(116) Liu, F.; Cui, Y.; Wang, L.; Wang, H.; Yuan, Y.; Pan, J.; Chen, H.; Yuan, L. *ACS Appl. Mater. Interfaces* **2015**, *7*, 11547–11554.

(117) Casciaro, B.; Moros, M.; Rivera-Fernández, S.; Bellelli, A.; de la Fuente, J. M.; Mangoni, M. L. *Acta Biomater.* **2017**, *47*, 170–181.

(118) Gianvincenzo, P. Di; Calvo, J.; Perez, S.; Álvarez, A.; Bedoya, L. M.; Alcamí, J.; Penadés, S. *Bioconjug. Chem.* **2015**, *26*, 755–765.

(119) Chen, Y.-S.; Hung, Y.-C.; Lin, W.-H.; Huang, G. S. *Nanotechnology* **2010**, *21*, 195101.

(120) Mahalakshmi, R.; Balaram, P. *D-Amino Acids A New Front. Amin. Acid Protein Res.* **2007**, 415–430.

(121) Jones, L. S.; Peek, L. J.; Power, J.; Markham, A.; Yazzie, B.; Middaugh, C. R. *J. Biol. Chem.* **2005**, *280*, 13406–13414.

(122) Peek, L. J.; Martin, T. T.; Nation, C. E.; Pegram, S. A.; Middaugh, C. R. *J. Pharm. Sci.* **2007**, *96*, 547–557.

(123) Paul, E.; Whitesides, G. M. *J. Phys. Chem.* **1994**, *98*, 563–571.

(124) Stranick, S. J.; Parikh, A. N.; Tao, Y.-T.; Allara, D. L.; Weiss, P. S. *J. Phys. Chem.* **1994**, *98*, 7636–7646.

(125) Kim, H.; Carney, R. P.; Reguera, J.; Ong, Q. K.; Liu, X.; Stellacci, F. *Adv. Mater.* **2012**, *24*, 3857–3863.

(126) Harkness, K. M.; Balinski, A.; McLean, J. A.; Cliffel, D. E. *Angew. Chem. Int. Ed. Engl.* **2011**, *50*, 10554–10559.

(127) Singh, C.; Ghorai, P.; Horsch, M.; Jackson, A.; Larson, R.; Stellacci, F.; Glotzer, S. *Phys. Rev. Lett.* **2007**, *99*, 226106.

(128) Sologan, M.; Marson, D.; Polizzi, S.; Pengo, P.; Boccardo, S.; Pricl, S.; Posocco, P.; Pasquato, L. *ACS Nano* **2016**, *10*, 9316–9325.

(129) Liu, X.; Yu, M.; Kim, H.; Mameli, M.; Stellacci, F. *Nat. Commun.* **2012**, *3*, 1182.

(130) Centrone, A.; Hu, Y.; Jackson, A. M.; Zerbi, G.; Stellacci, F. *Small* **2007**, *3*, 814–817.

(131) Pradhan, S.; Brown, L. E.; Konopelski, J. P.; Chen, S. *J. Nanoparticle Res.* **2008**, *11*, 1895–1903.

(132) Pradhan, S.; Xu, L. P.; Chen, S. *Adv. Funct. Mater.* **2007**, *17*, 2385–2392.

(133) Jackson, A. M.; Myerson, J. W.; Stellacci, F. *Nat. Mater.* **2004**, *3*, 330–336.

(134) Häkkinen, H. *Nat. Chem.* **2012**, *4*, 443–455.

(135) Jadzinsky, P. D.; Calero, G.; Ackerson, C. J.; Bushnell, D. A.; Kornberg, R. D. *Science* **2007**, *318*, 430–433.

(136) Walter, M.; Akola, J.; Lopez-Acevedo, O.; Jadzinsky, P. D.; Calero, G.; Ackerson, C. J.; Whetten, R. L.; Gronbeck, H.; Hakkinen, H. *Proc. Natl. Acad. Sci.* **2008**, *105*, 9157–9162.

(137) Li, R.; Bowerman, B. *Cold Spring Harb. Perspect. Biol.* **2010**, *2*, 1–5.

(138) Schroeder, H. W. J.; Cavacini, L. *J. Allergy Clin. Immunol.* **2010**, *125*, S41–S52.

(139) Li, N.; Zhao, P.; Astruc, D. *Angew. Chem. Int. Ed. Engl.* **2014**, *53*, 1756–1789.

(140) Murthy, S. K. *Int. J. Nanomedicine* **2007**, *2*, 129–141.

(141) Verma, A.; Stellacci, F. *Small* **2010**, *6*, 12–21.

(142) Gao, Y.; Yu, Y. *J. Am. Chem. Soc.* **2013**, *135*, 19091–19094.

(143) Walther, A.; Müller, A. H. E. *Chem. Rev.* **2013**, *113*, 5194–5261.

(144) Wong, O. A.; Heinecke, C. L.; Simone, A. R.; Whetten, L.; Ackerson, C. J. *Nanoscale* **2012**, *102*, 4099–4102.

(145) Centers for Disease Control and Prevention. *Updated Guidelines for Antiretroviral Postexposure Prophylaxis After Sexual , Injection Drug Use , or Other Nonoccupational Exposure to HIV — United States , 2016*; 2016.

(146) HIV drug classes http://aids.gov/hiv-aids-basics/just-diagnosed-with-hiv-aids/treatment-options/overview-of-hiv-treatments/.

(147) Kwong, P. D.; Wyatt, R.; Robinson, J.; Sweet, R. W.; Sodroski, J.; Hendrickson, W. a. *Nature* **1998**, *393*, 648–659.

(148) Li, Y.; O'Dell, S.; Walker, L. M.; Wu, X.; Guenaga, J.; Feng, Y.; Schmidt, S. D.; McKee, K.; Louder, M. K.; Ledgerwood, J. E.; Graham, B. S.; Haynes, B. F.; Burton, D. R.; Wyatt, R. T.; Mascola, J. R. *J. Virol.* **2011**, *85*, 8954–8967.

(149) Herzyk, D. J.; Gore, E. R.; Polsky, R.; Nadwodny, K. L.; Maier, C. C.; Liu, S.; Hart, T. K.; Harmsen, A. G.; Bugelski, P. J. *Infect. Immun.* **2001**, *69*, 1032–1043.

(150) Bruno, C. J.; Jacobson, J. M. *J. Antimicrob. Chemother.* **2010**, *65*, 1839–1841.

(151) Bowman, M.-C.; Ballard, T. E.; Ackerson, C. J.; Feldheim, D. L.; Margolis, D. M.; Melander, C. *J. Am. Chem. Soc.* **2008**, *130*, 6896–6897.

(152) Miller, S. A.; Hiatt, L. A.; Keil, R. G.; Wright, D. W.; Cliffel, D. E. *Anal. Bioanal. Chem.* **2011**, *399*, 1021–1029.

(153) Simpson, C. A.; Huffman, B. J.; Gerdon, A. E.; Cliffel, D. E. *Chem. Res. Toxicol.* **2010**, *23*, 1608–1616.

(154) Gerdon, A. E.; Wright, D. W.; Cliffel, D. E. *Anal. Chem.* **2005**, *77*, 304–310.

(155) Frey, G.; Peng, H.; Rits-Volloch, S.; Morelli, M.; Cheng, Y.; Chen, B. *Proc. Natl. Acad. Sci. U. S. A.* **2008**, *105*, 3739–3744.

(156) Hart, M. L.; Saifuddin, M.; Spear, G. T. *J. Gen. Virol.* **2003**, *84*, 353–360.

(157) Lusic, H.; Grinstaff, M. W. *Chem Rev* **2013**, *113*, 1641–1666.

(158) El-Sayed, M. A.; Shabaka, A. A.; El-Shabrawy, O. A.; Yassin, N. A.; Mahmoud, S. S.; El-Shenawy, S. M.; Al-Ashqar, E.; Eisa, W. H.; Farag, N. M.; El-Shaer, M. A.; Salah, N.; Al-Abd, A. M. *PLoS One* **2013**, *8*, e76207.

(159) Lassiter, J. B.; Aizpurua, J.; Hernandez, L. I.; Brandl, D. W.; Romero, I.; Lal, S.; Hafner, J. H.; Nordlander, P.; Halas, N. J. *Nano Lett.* **2008**, *8*, 1212–1218.

(160) Bhatia, S. N.; Ingber, D. E. *Nat Biotech* **2014**, *32*, 760–772.

(161) Esch, E. W.; Bahinski, A.; Huh, D. *Nat. Rev. Drug Discov.* **2015**, *14*, 248–260.

(162) Shanks, N.; Greek, R.; Greek, J. *Philos. Ethics, Humanit. Med.* **2009**, *4*, 2.

(163) Wikswo, J. P.; Block, F. E.; Cliffel, D. E.; Goodwin, C. R.; Marasco, C. C.; Markov, D. A.; McLean, D. L.; McLean, J. A.; McKenzie, J. R.; Reiserer, R. S.; Samson, P. C.; Schaffer, D. K.; Seale, K. T.; Sherrod, S. D. *IEEE Trans. Biomed. Eng.* **2013**, *60*, 682–690.

(164) Hastings, M.; O'Neill, J. S.; Maywood, E. S. *J. Endocrinol.* **2007**, *195*, 187–198.

(165) Chung, B. G.; Lin, F.; Li Jeon, N. *Lab Chip* **2006**, *6*, 764–768.

(166) Jang, Y.-H.; Hancock, M. J.; Kim, S. B.; Selimović, S.; Sim, W. Y.; Bae, H.; Khademhosseini, A. *Lab Chip* **2011**, *11*, 3277–3286.

(167) Lin, F.; Saadi, W.; Rhee, S. W.; Wang, S.-J.; Mittal, S.; Jeon, N. L. *Lab Chip* **2004**, *4*, 164–167.

(168) He, L.; Kniss, A.; San-Miguel, A.; Rouse, T.; Kemp, M. L.; Lu, H. *Lab Chip* **2015**, *15*, 1497–1507.

(169) Block, F. E. I.; Samson, P. C.; Wikswo, J. P. Normally closed microvalve and applications of the same. US9618129 B2, 2017.

(170) Cordeiro, C. A.; de Vries, M. G.; Ngabi, W.; Oomen, P. E.; Cremers, T. I.; Westerink, B. H. *Biosens Bioelectron* **2015**, *67*, 677–686.

(171) Gao, W.; Nyein, H. Y. Y.; Shahpar, Z.; Fahad, H. M.; Chen, K.; Emaminejad, S.; Gao, Y.; Tai, L.-C.; Ota, H.; Wu, E.; Bullock, J.; Zeng, Y.; Lien, D.-H.; Javey, A. *ACS Sensors* **2016**, *1*, 866–874.

(172) Patel, B. A.; Rogers, M.; Wieder, T.; O'Hare, D.; Boutelle, M. G. *Biosens Bioelectron* **2011**, *26*, 2890–2896.

(173) Qi, L.; Thomas, E.; White, S. H.; Smith, S. K.; Lee, C. A.; Wilson, L. R.; Sombers, L. A. *Anal Chem* **2016**, *88*, 8129–8136.

(174) Rogers, M. L.; Feuerstein, D.; Leong, C. L.; Takagaki, M.; Niu, X.; Graf, R.; Boutelle, M. G. *ACS Chem Neurosci* **2013**, *4*, 799–807.

(175) Tolosa, V. M.; Wassum, K. M.; Maidment, N. T.; Monbouquette, H. G. *Biosens Bioelectron* **2013**, *42*, 256–260.

(176) Wassum, K. M.; Tolosa, V. M.; Wang, J.; Walker, E.; Monbouquette, H. G.; Maidment, N. T. *Sensors (Basel)* **2008**, *8*, 5023–5036.

(177) Córcoles, E. P.; Deeba, S.; Hanna, G. B.; Paraskeva, P.; Boutelle, M. G.; Darzi, A. *Anal. Methods* **2011**, *3*, 2010.

(178) Feuerstein, D.; Manning, A.; Hashemi, P.; Bhatia, R.; Fabricius, M.; Tolias, C.; Pahl, C.; Ervine, M.; Strong, A. J.; Boutelle, M. G. *J Cereb Blood Flow Metab* **2010**, *30*, 1343–1355.

(179) Lawrance, D.; Williamson, C.; Boutelle, M. G.; Cass, A. E. G. *Anal. Methods* **2015**, *7*, 3714–3719.

(180) Lee, H.; Choi, T. K.; Lee, Y. B.; Cho, H. R.; Ghaffari, R.; Wang, L.; Choi, H. J.; Chung, T. D.; Lu, N.; Hyeon, T.; Choi, S. H.; Kim, D. H. *Nat Nanotechnol* **2016**, *11*, 566–572.

(181) Lin, Y.; Liu, K.; Yu, P.; Xiang, L.; Li, X.; Mao, L. *Anal Chem* **2007**, *79*, 9577–9583.

(182) Rogers, M. L.; Brennan, P. A.; Leong, C. L.; Gowers, S. A.; Aldridge, T.; Mellor, T. K.; Boutelle, M. G. *Anal Bioanal Chem* **2013**, *405*, 3881–3888.

(183) Gao, W.; Emaminejad, S.; Nyein, H. Y.; Challa, S.; Chen, K.; Peck, A.; Fahad, H. M.; Ota, H.; Shiraki, H.; Kiriya, D.; Lien, D. H.; Brooks, G. A.; Davis, R. W.; Javey, A. *Nature* **2016**, *529*, 509–514.

(184) Sansuk, S.; Bitziou, E.; Joseph, M. B.; Covington, J. A.; Boutelle, M. G.; Unwin, P. R.; Macpherson, J. V. *Anal Chem* **2013**, *85*, 163–169.

(185) Eklund, S. E.; Cliffel, D. E.; Kozlov, E.; Prokop, A.; Wikswo, J.; Baudenbacher, F. *Anal. Chim. Acta* **2003**, *496*, 93–101.

(186) McConnell, H.; Owicki, J.; Parce, J.; Miller, D.; Baxter, G.; Wada, H.; Pitchford, S. *Science (80-.).* **1992**, *257*, 1906–1912.

(187) Eklund, S. E.; Taylor, D.; Kozlov, E.; Prokop, A.; Cliffel, D. E. *Anal Chem* **2004**, *76*, 519–527.

(188) Eklund, S. E.; Snider, R. M.; Wikswo, J.; Baudenbacher, F.; Prokop, A.; Cliffel, D. E. *J. Electroanal. Chem.* **2006**, *587*, 333–339.

(189) Eklund, S. E.; Thompson, R. G.; Snider, R. M.; Carney, C. K.; Wright, D. W.; Wikswo, J.; Cliffel, D. E. *Sensors* **2009**, *9*, 2117–2133.

(190) Snider, R. M.; McKenzie, J. R.; Kraft, L.; Kozlov, E.; Wikswo, J. P.; Cliffel, D. E. *Toxins (Basel)* **2010**, *2*, 632–648.

(191) McKenzie, J. R.; Palubinsky, A. M.; Brown, J. E.; McLaughlin, B.; Cliffel, D. E. *ACS Chem Neurosci* **2012**, *3*, 510–518.

(192) Shinawi, T. F.; Kimmel, D. W.; Cliffel, D. E. *Anal Chem* **2013**, *85*, 11677–11680.

(193) Kimmel, D. W.; Dole, W. P.; Cliffel, D. E. *Biochem Biophys Res Commun* **2013**, *431*, 181–185.

(194) Kimmel, D. W.; Meschievitz, M. E.; Hiatt, L. A.; Cliffel, D. E. *Electroanalysis* **2013**, *25*, 1706–1712.

(195) Hiatt, L. A.; McKenzie, J. R.; Deravi, L. F.; Harry, R. S.; Wright, D. W.; Cliffel, D. E. *Biosens Bioelectron* **2012**, *33*, 128–133.

(196) Snider, R. M.; Ciobanu, M.; Rue, A. E.; Cliffel, D. E. *Anal Chim Acta* **2008**, *609*, 44–52.

(197) Zeiger, S. L.; McKenzie, J. R.; Stankowski, J. N.; Martin, J. A.; Cliffel, D. E.; McLaughlin, B. *Biochim Biophys Acta* **2010**, *1802*, 1095–1104.

(198) Harry, R. S.; Hiatt, L. A.; Kimmel, D. W.; Carney, C. K.; Halfpenny, K. C.; Cliffel, D. E.; Wright, D. W. *Chem Res Toxicol* **2012**, *25*, 1643–1651.

(199) Kimmel, D. W.; Rogers, L. M.; Aronoff, D. M.; Cliffel, D. E. *Chem Res Toxicol* **2016**, *29*, 19–25.

(200) McKenzie, J. R.; Cognata, A. C.; Davis, A. N.; Wikswo, J. P.; Cliffel, D. E. *Anal Chem* **2015**, *87*, 7857–7864.

(201) Brown, J. A.; Pensabene, V.; Markov, D. A.; Allwardt, V.; Diana Neely, M.; Shi, M.; Britt, C. M.; Hoilett, O. S.; Yang, Q.; Brewer, B. M.; Samson, P. C.; McCawley, L. J.; May, J. M.; Webb, D. J.; Li, D.; Bowman, A. B.; Reiserer, R. S.; Wikswo, J. P. *Biomicrofluidics* **2015**, *9*, 1–15.

(202) Lima, E. A.; Snider, R. M.; Reiserer, R. S.; McKenzie, J. R.; Kimmel, D. W.; Eklund, S. E.; Wikswo, J. P.; Cliffel, D. E. *Sens Actuators B Chem* **2014**, *204*, 536–543.

(203) Jones, D. A.; Parkin, M. C.; Langemann, H.; Landolt, H.; Hopwood, S. E.; Strong, A. J.; Boutelle, M. G. *J. Electroanal. Chem.* **2002**, *538–539*, 243–252.

(204) Parkin, M.; Hopwood, S.; Jones, D. A.; Hashemi, P.; Landolt, H.; Fabricius, M.; Lauritzen, M.; Boutelle, M. G.; Strong, A. J. *J Cereb Blood Flow Metab* **2005**, *25*, 402–413.

(205) Belle, A. M.; Owesson-White, C.; Herr, N. R.; Carelli, R. M.; Wightman, R. M. *ACS Chem Neurosci* **2013**, *4*, 761–771.

(206) Hashemi, P.; Dankoski, E. C.; Lama, R.; Wood, K. M.; Takmakov, P.; Wightman, R. M. *PNAS* **2012**, *109*, 11510–11515.

(207) Keithley, R. B.; Takmakov, P.; Bucher, E. S.; Belle, A. M.; Owesson-White, C. A.; Park, J.; Wightman, R. M. *Anal Chem* **2011**, *83*, 3563–3571.

(208) Kirkpatrick, D. C.; McKinney, C. J.; Manis, P. B.; Wightman, R. M. *Analyst* **2016**, *141*, 4902–4911.

(209) Roberts, J. G.; Toups, J. V; Eyualem, E.; McCarty, G. S.; Sombers, L. A. *Anal Chem* **2013**, *85*, 11568–11575.

(210) Rodeberg, N. T.; Johnson, J. A.; Cameron, C. M.; Saddoris, M. P.; Carelli, R. M.; Wightman, R. M. *Anal Chem* **2015**, *87*, 11484–11491.

(211) Nyein, H. Y.; Gao, W.; Shahpar, Z.; Emaminejad, S.; Challa, S.; Chen, K.; Fahad, H. M.; Tai, L. C.; Ota, H.; Davis, R. W.; Javey, A. *ACS Nano* **2016**, *10*, 7216–7224.

(212) Ross, A. E.; Venton, B. J. *Anal Chem* **2014**, *86*, 7486–7493.

(213) Gowers, S. A.; Curto, V. F.; Seneci, C. A.; Wang, C.; Anastasova, S.; Vadgama, P.; Yang, G. Z.; Boutelle, M. G. *Anal Chem* **2015**, *87*, 7763–7770.

Curriculum Vitae

Vanderbilt University
Department of Chemistry
Station B 351822
Nashville, TN 37235

lab phone: (615) 322-5013
adam.travis@vanderbilt.edu

Education

Vanderbilt University Nashville, TN
Ph.D., Department of Chemistry, August 2017, GPA: 3.91, Dissertation: *Governing the Biological Interactions of Monolayer Protected Gold Nanoparticles by Controlling the Composition and Spatial Structure of the Thiolate Shell*

The University of Tennessee at Martin Martin, TN
B.S., Major: Chemistry, Minor: Biology, Summa Cum Laude, May 2011, GPA: 4.00, University Scholar Thesis: *The Chromatographic Isolation of Tadpole Erythrocyte Ferrireductase*

Research Experience

Vanderbilt University Nashville, TN
Advisors: Prof. David E. Cliffel and Prof. David W. Wright

- Synthesized small molecule thiols and peptides for place exchange onto gold nanoparticles to identify trends in self-assembling nanostructures and targeted radiosensitizers
- Purified materials through dialysis, flash chromatography, and HPLC
- Characterized materials using ^{1}H NMR, NOESY, TEM, TGA, UV/Vis, FT-IR, fluorimetry, GC-MS, and MALDI-MS
- Cultured primary and immortalized mammalian cells for flow cytometry, confocal microscopy, dark-field microscopy, and ^{137}Cs clonogenic assays
- Validated microformulator devices using electrochemistry and ICP-OES
- Collaborated with engineering team to develop multiplexed enzymatic biosensors for continuous amperometric monitoring of effluent from organs-on-chips

The University of Tennessee at Martin Martin, TN
Advisor: Prof. Charles R. Thomas

- Collected larval *Rana catesbeiana* field samples from local ponds
- Maintained, anaesthetized, and sacrificed *R. catesbeiana* for whole blood samples which were subsequently fractionated and lysed
- Separated erythrocytic components using gel permeation, ion exchange, and hydrophobic interaction chromatography
- Assessed activity of fractions with an air-sensitive optical assay employing density gradients

Teaching Experience

Vanderbilt University Nashville, TN

Advanced Integrated Laboratory

- Assisted senior undergraduates with experimental design to independently accomplish broad research goals
- Demonstrated advanced techniques including gel electrophoresis, protein digestion, MALDI-MS, ICP-OES, air-free synthesis, fluorimetry, TGA, and TEM

General Chemistry Laboratory

- Instructed multiple sections of 24 students in general chemistry practices and graded weekly reports

Graduate Student Mentor

- Mentored five summer research students in various programs including the Short-Term Training Program for Minority Students
- Mentored three Vanderbilt undergraduate Honors Thesis students
- Mentored six first-year Vanderbilt graduate students in rotations
- Assisted a Fisk graduate student in the trans-institutional Fisk-Vanderbilt Bridge Program with experimental design for her M.S. thesis

The University of Tennessee at Martin Martin, TN

General Chemistry

- Co-instructed multiple sections of 48 students in general chemistry practices and graded weekly reports and quizzes
- Prepared reagents and formulated unknowns for each lab section

Student Athletics Tutor

- Tutored student athletes in calculus and algebra-based physics

Math Lab Assistant

- Assisted students with remedial math, college algebra, statistics, calculus I/II, and math-based education courses

Publications

Travis, A. R.; Cliffel, D. E.; Wikswo, J. P. "Validation of a Rotary Planar Valve and Rotary Planar Peristaltic Micropump as a Microformulator." *Lab on a Chip* (In Preparation)

Travis, A. R.; McClain, E. S.; Melow, S. L.; Crisostomo, D. A.; Xu, K.; Cliffel, D. E. "On-Line Electrochemical Monitoring of a Model Blood Brain Barrier Using an Integrated Multianalyte Microclinical Analyzer and Neurovascular Unit-on-a-Chip." *Lab on a Chip* (In Preparation)

Travis, A. R.; Liau, V. A.; Agrawal, A. C.; Cliffel, D. E. "Small Gold Nanoparticles Presenting Linear and Looped Cilengitide Analogues as Radiosensitizers of Cells Expressing $\alpha_v\beta_3$ Integrin." *J. Nanopart. Res.* (Under Review)

Agrawal, A. C.; **Travis, A. R.**; Harkness, K. M.; Kimmel, D. W.; Cliffel, D. E. "Ultrasmall Gold Clusters Presenting Conformational Peptide Mimics of an Epitope from the Protective Antigen of Bacillus anthracis Stimulate Anti-PA Antibody Production in Mice." *Bioconj. Chem.* (Submitted)

Davis, A. N.; **Travis, A. R.**; Miller, D. R.; Cliffel, D. E. "Multianalyte Physiological Microanalytical Devices." *Annu. Rev. Anal. Chem.* **2017**, 10, 93-111.

Jackson, S. R.; Wong, A. C.; **Travis, A. R.**; Catrina, I. E.; Bratu, D. P.; Wright, D. W.; Jayagopal, A. "Applications of Hairpin DNA-Functionalized Gold Nanoparticles for Imaging mRNA in Living Cells." *Methods Enzymol.* **2016**, 572, 87-103.

Presentations

Travis, A. R. and Cliffel, D. E. "Targeted Radiosensitization with RGD-Containing Cilengitide Mimics on Small Gold Nanoparticles." 39th Area Collegiate Chemistry Meeting, Martin, TN. Oral Presentation.

Travis, A. R.; Liau, V. A.; Cliffel, D. E. "Evaluation of the Radiosensitizing Effects of Small Gold Nanoparticles Presenting Linear and Looped RGD-Containing Peptides." 2015 Pittsburgh Conference on Analytical Chemistry and Applied Spectroscopy, New Orleans, LA. Poster Presentation.

Travis, A. R. and Thomas, C. R. "Tadpole Erythrocyte Ferrireductase." 34th Area Collegiate Chemistry Meeting, Murray, KY. Oral Presentation.

Travis, A. R. and Thomas, C. R. "Purification of Tadpole Erythrocyte Ferrireductase." 33rd Area Collegiate Chemistry Meeting, Martin, TN. Oral Presentation.

Awards

University Graduate Fellowship, 2011-2016
Frederic LeRoy Conover Graduate Research Fellowship, 2015
Vanderbilt Institute of Chemical Biology Fellowship, 2011
University Scholar, 2007-2011
Outstanding Chemistry Major Award, 2011
Outstanding Physics and Astronomy Student, 2010
Lower Division Chemistry Award, 2009
Norman and Ruby Campbell Scholarship, 2008
Valedictorian Recognition Award, 2007

Professional Affiliations
American Chemical Society, Member
Material Research Society, Member
The Electrochemical Society, Member
Society for Applied Spectroscopy, Member

References

Prof. David E. Cliffel
Vanderbilt University, Department of Chemistry, Station B 351822, Nashville, TN 37235
Phone: (615) 343-3937 Fax: (615) 343-1234 Email: d.cliffel@vanderbilt.edu

Prof. David W. Wright
Vanderbilt University, Department of Chemistry, Station B 351822, Nashville, TN 37235
Phone: (615) 322-2636 Fax: (615) 343-1234 Email: david.wright@vanderbilt.edu

Prof. John P. Wikswo
Vanderbilt University, Vanderbilt Institute for Integrative Biosystems Research and Education, Station B 351807, Nashville, TN 37235
Phone: (615) 343-4124 Fax: (615) 322-4977 Email: john.wikswo@vanderbilt.edu